Université de Montréal

# Analysis of the human corneal shape with machine learning

par

Hala Bouazizi

Département d'informatique et de recherche opérationnelle

Faculté des arts et des sciences

Thèse présentée à la Faculté des études supérieures

en vue de l'obtention du grade de Philosophiæ Doctor (Ph.D.)

en informatique

Janvier 2023

# Résumé

Cette thèse cherche à examiner les conditions optimales dans lesquelles les surfaces cornéennes antérieures peuvent être efficacement pré-traitées, classifiées et prédites en utilisant des techniques de modélisation géométriques (MG) et d'apprentissage automatiques (AU).

La première étude (Chapitre 2) examine les conditions dans lesquelles la modélisation géométrique peut être utilisée pour réduire la dimensionnalité des données utilisées dans un projet d'apprentissage automatique. Quatre modèles géométriques ont été testés pour leur précision et leur rapidité de traitement : deux modèles polynomiaux (P) – polynômes de Zernike (PZ) et harmoniques sphériques (PHS) – et deux modèles de fonctions rationnelles (R) : fonctions rationnelles de Zernike (RZ) et fonctions rationnelles d'harmoniques sphériques (RSH). Il est connu que les modèles PHS et RZ sont plus précis que les modèles PZ pour un même nombre de coefficients (*J*), mais on ignore si les modèles PHS performent mieux que les modèles RZ, et si, de manière plus générale, les modèles SH sont plus précis que les modèles R, ou l'inverse. Et prenant en compte leur temps de traitement, est-ce que les modèles les plus précis demeurent les plus avantageux? Considérant des valeurs de *J* (nombre de coefficients du modèle) relativement basses pour respecter les contraintes de dimensionnalité propres aux taches d'apprentissage automatique, nous avons établi que les modèles HS (PHS et RHS) étaient tous deux plus précis que les modèles Z correspondants (PZ et RR), et que l'avantage de précision conféré par les modèles HS était plus important que celui octroyé par les modèles R. Par ailleurs, les courbes de temps de traitement en fonction de *J* démontrent qu'alors que les modèles P sont traités en temps quasi-linéaires, les modèles R le sont en temps polynomiaux. Ainsi, le modèle SHR est le plus précis, mais aussi le plus lent (un problème qui peut en partie être remédié en appliquant une procédure de pré-optimisation). Le modèle ZP était de loin le plus rapide, et il demeure une option intéressante pour le développement de projets. SHP constitue le meilleur compromis entre la précision et la rapidité.

La classification des cornées selon des paramètres cliniques a une longue tradition, mais la visualisation des effets moyens de ces paramètres sur la forme de la cornée par des cartes topographiques est plus récente. Dans la seconde étude (Chapitre 3), nous avons construit un atlas de cartes d'élévations moyennes pour différentes variables cliniques qui pourrait s'avérer utile pour l'évaluation et l'interprétation des données d'entrée (bases de données) et de sortie (prédictions, clusters, etc.) dans des tâches d'apprentissage automatique, entre autres. Une base de données constituée de plusieurs milliers de surfaces cornéennes antérieures normales enregistrées sous forme de matrices d'élévation de 101 by 101 points a d'abord été traitée par modélisation géométrique pour réduire sa dimensionnalité à un nombre de coefficients optimal dans une optique d'apprentissage automatique. Les surfaces ainsi modélisées ont été regroupées en fonction de variables cliniques de forme, de réfraction et de démographie. Puis, pour chaque groupe de chaque variable clinique, une surface moyenne a été calculée et représentée sous forme de carte d'élévations faisant référence à sa SMA (sphère la mieux ajustée). Après avoir validé la conformité de la base de donnée avec la littérature par des tests statistiques (ANOVA), l'atlas a été vérifié cliniquement en examinant si les transformations de formes cornéennes présentées dans les cartes pour chaque variable étaient conformes à la littérature. C'était le cas. Les applications possibles d'un tel atlas sont discutées.

La troisième étude (Chapitre 4) traite de la classification non-supervisée (clustering) de surfaces cornéennes antérieures normales. Le clustering cornéen un domaine récent en ophtalmologie. La plupart des études font appel aux techniques d'extraction des caractéristiques pour réduire la dimensionnalité de la base de données cornéennes. Le but est généralement d'automatiser le processus de diagnostique cornéen, en particulier en ce qui a trait à la distinction entre les cornées normales et les cornées irrégulières (kératocones, Fuch, etc.), et dans certains cas, de distinguer différentes sous-classes de cornées irrégulières. L'étude de clustering proposée ici se concentre plutôt sur les cornées normales afin de mettre en relief leurs regroupements naturels. Elle a recours

à la modélisation géométrique pour réduire la dimensionnalité de la base de données, utilisant des polynômes de Zernike, connus pour leur interprétativité transparente (chaque terme polynomial est associé à une caractéristique cornéenne particulière) et leur bonne précision pour les cornées normales. Des méthodes de différents types ont été testées lors de prétests (méthodes de clustering dur (hard) ou souple (soft), linéaires or non-linéaires. Ces méthodes ont été testées sur des surfaces modélisées naturelles (non-normalisées) ou normalisées avec ou sans traitement d'extraction de traits, à l'aide de différents outils d'évaluation (scores de séparabilité et d'homogénéité, représentations par cluster des coefficients de modélisation et des surfaces modélisées, comparaisons statistiques des clusters sur différents paramètres cliniques). Les résultats obtenus par la meilleure méthode identifiée, k-means sans extraction de traits, montrent que les clusters produits à partir de surfaces cornéennes naturelles se distinguent essentiellement en fonction de la courbure de la cornée, alors que ceux produits à partir de surfaces normalisées se distinguent en fonction de l'axe cornéen.

La dernière étude présentée dans cette thèse (Chapitre 5) explore différentes techniques d'apprentissage automatique pour prédire la forme de la cornée à partir de données cliniques. La base de données cornéennes a d'abord été traitée par modélisation géométrique (polynômes de Zernike) pour réduire sa dimensionnalité à de courts vecteurs de 12 à 20 coefficients, une fourchette de valeurs potentiellement optimales pour effectuer de bonnes prédictions selon des prétests. Différentes méthodes de régression non-linéaires, tirées de la bibliothèque scikit-learn, ont été testées, incluant gradient boosting, Gaussian process, kernel ridge, random forest, k-nearest neighbors, bagging, et multi-layer perceptron. Les prédicteurs proviennent des variables cliniques disponibles dans la base de données, incluant des variables géométriques (rayon de la sphere la mieux ajustée, diamètre horizontal de la cornée, profondeur de la chambre cornéenne, côté de l'œil), des variables de réfraction (cylindre, sphère et axe) et des variables démographiques (âge, genre). Un test de régression a été effectué pour chaque modèle de régression, défini comme la sélection d'une des 512 combinaisons possibles de variables cliniques (les prédicteurs), d'une méthode de régression, et d'un vecteur de coefficients de Zernike d'une certaine taille (entre 12 et 20 coefficients, les cibles). Tous les modèles de régression testés ont été évalués à l'aide de score de RMSE établissant la distance entre les surfaces cornéennes prédites (les prédictions) et vraies (les topographies cornéennes brutes). Les meilleurs d'entre eux ont été validés sur l'ensemble de données randomisé 20 fois pour déterminer avec plus de précision lequel d'entre eux est le plus performant. Il s'agit de gradient boosting utilisant toutes les variables cliniques comme prédicteurs et 16 coefficients de Zernike comme cibles. Le prédicteur le plus contributif était le rayon de la sphere la mieux ajustée, suivi du côté de l'œil et de paramètres de réfraction. Les prédictions de ce modèle ont été évaluées qualitativement à l'aide d'un atlas de cartes d'élévations moyennes élaborées à partir des variables cliniques ayant servi de prédicteurs, qui permet de visualiser les transformations moyennes d'en groupe à l'autre pour chaque variables. Cet atlas a permis d'établir que les cornées prédites moyennes sont remarquablement similaires aux vraies cornées moyennes pour toutes les variables cliniques à l'étude.

**Mots-clés :** cornée, polynômes de Zernike, harmoniques sphériques, fonctions rationnelles, topographie cornéenne, cartes d'élévations moyennes, clustering, clustering agglomératif, clustering en k-moyennes, clustering spectral, régression, gradient boosting, processus gaussien, kernel ridge, random forest, k-nearest neighbors, bagging.

# Abstract

This thesis aims to investigate the best conditions in which the anterior corneal surface of normal corneas can be preprocessed, classified and predicted using geometric modeling (GM) and machine learning (ML) techniques. The focus is on the anterior corneal surface, which is the main responsible of the refractive power of the cornea.

Dealing with preprocessing, the first study (Chapter 2) examines the conditions in which GM can best be applied to reduce the dimensionality of a dataset of corneal surfaces to be used in ML projects. Four types of geometric models of corneal shape were tested regarding their accuracy and processing time: two polynomial (P) models – Zernike polynomial (ZP) and spherical harmonic polynomial (SHP) models – and two corresponding rational function (R) models – Zernike rational function (ZR) and spherical harmonic rational function (SHR) models. SHP and ZR are both known to be more accurate than ZP as corneal shape models for the same number of coefficients, but which type of model is the most accurate between SHP and ZR? And is an SHR model, which is both an SH model and an R model, even more accurate? Also, does modeling accuracy comes at the cost of the processing time, an important issue for testing large datasets as required in ML projects? Focusing on low $J$ values (number of model coefficients) to address these issues in consideration of dimensionality constraints that apply in ML tasks, it was found, based on a number of evaluation tools, that SH models were both more accurate than their Z counterparts, that R models were both more accurate than their P counterparts and that the SH advantage was more important than the R advantage. Processing time curves as a function of $J$ showed that P models were processed in quasi-linear time, R models in polynomial time, and that Z models were fastest than SH models. Therefore, while SHR was the most accurate geometric model, it was the slowest (a problem that can partly be remedied by applying a preoptimization procedure). ZP was the fastest model, and with normal corneas, it remains an interesting option for testing and development, especially for clustering tasks due to its transparent interpretability. The best compromise between accuracy and speed for ML preprocessing is SHP.

The classification of corneal shapes with clinical parameters has a long tradition, but the visualization of their effects on the corneal shape with group maps (average elevation maps, standard deviation maps, average difference maps, etc.) is relatively recent. In the second study (Chapter 3), we constructed an atlas of average elevation maps for different clinical variables (including geometric, refraction and demographic variables) that can be instrumental in the evaluation of ML task inputs (datasets) and outputs (predictions, clusters, etc.). A large dataset of normal adult anterior corneal surface topographies recorded in the form of 101×101 elevation matrices was first preprocessed by geometric modeling to reduce the dimensionality of the dataset to a small number of Zernike coefficients found to be optimal for ML tasks. The modeled corneal surfaces of the dataset were then grouped in accordance with the clinical variables available in the dataset transformed into categorical variables. An average elevation map was constructed for each group of corneal surfaces of each clinical variable in their natural (non-normalized) state and in their normalized state by averaging their modeling coefficients to get an average surface and by representing this average surface in reference to the best-fit sphere in a topographic elevation map. To validate the atlas thus constructed in both its natural and normalized modalities, ANOVA tests were conducted for each clinical variable of the dataset to verify their statistical consistency with the literature before verifying whether the corneal shape transformations displayed in the maps were themselves visually consistent. This was the case. The possible uses of such an atlas are discussed.

The third study (Chapter 4) is concerned with the use of a dataset of geometrically modeled corneal surfaces in an ML task of clustering. The unsupervised classification of corneal surfaces is recent in ophthalmology. Most of the few existing studies on corneal clustering resort to feature extraction (as opposed to geometric modeling) to achieve the dimensionality reduction of the

dataset. The goal is usually to automate the process of corneal diagnosis, for instance by distinguishing irregular corneal surfaces (keratoconus, Fuch, etc.) from normal surfaces and, in some cases, by classifying irregular surfaces into subtypes. Complementary to these corneal clustering studies, the proposed study resorts mainly to geometric modeling to achieve dimensionality reduction and focuses on normal adult corneas in an attempt to identify their natural groupings, possibly in combination with feature extraction methods. Geometric modeling was based on Zernike polynomials, known for their interpretative transparency and sufficiently accurate for normal corneas. Different types of clustering methods were evaluated in pretests to identify the most effective at producing neatly delimitated clusters that are clearly interpretable. Their evaluation was based on clustering scores (to identify the best number of clusters), polar charts and scatter plots (to visualize the modeling coefficients involved in each cluster), average elevation maps and average profile cuts (to visualize the average corneal surface of each cluster), and statistical cluster comparisons on different clinical parameters (to validate the findings in reference to the clinical literature). K-means, applied to geometrically modeled surfaces without feature extraction, produced the best clusters, both for natural and normalized surfaces. While the clusters produced with natural corneal surfaces were based on the corneal curvature, those produced with normalized surfaces were based on the corneal axis. In each case, the best number of clusters was four. The importance of curvature and axis as grouping criteria in corneal data distribution is discussed.

The fourth study presented in this thesis (Chapter 5) explores the ML paradigm to verify whether accurate predictions of normal corneal shapes can be made from clinical data, and how. The database of normal adult corneal surfaces was first preprocessed by geometric modeling to reduce its dimensionality into short vectors of 12 to 20 Zernike coefficients, found to be in the range of appropriate numbers to achieve optimal predictions. The nonlinear regression methods examined from the scikit-learn library were gradient boosting, Gaussian process, kernel ridge, random forest, k-nearest neighbors, bagging, and multilayer perceptron. The predictors were based on the clinical variables available in the database, including geometric variables (best-fit sphere radius, white-to-white diameter, anterior chamber depth, corneal side), refraction variables (sphere, cylinder, axis) and demographic variables (age, gender). Each possible combination of regression method, set of clinical variables (used as predictors) and number of Zernike coefficients (used as targets) defined a regression model in a prediction test. All the regression models were evaluated based on their mean RMSE score (establishing the distance between the predicted corneal surfaces and the raw topographic true surfaces). The best model identified was further qualitatively assessed based on an atlas of predicted and true average elevation maps by which the predicted surfaces could be visually compared to the true surfaces on each of the clinical variables used as predictors. It was found that the best regression model was gradient boosting using all available clinical variables as predictors and 16 Zernike coefficients as targets. The most explicative predictor was the best-fit sphere radius, followed by the side and refractive variables. The average elevation maps of the true anterior corneal surfaces and the predicted surfaces based on this model were remarkably similar for each clinical variable.

**Keywords:** cornea, Zernike polynomials, spherical harmonics, rational functions, corneal topography, atlas, average elevation map, clustering, agglomerative clustering, k-means clustering, spectral clustering, regression, gradient boosting, Gaussian process, kernel ridge, random forest, k-nearest neighbors, bagging

# Acknowledgments

Words cannot express enough my gratitude to my supervisor Jean Meunier, who so generously supported me with his vast knowledge and expertise during my Ph.D. program. I could not finish this project effectively without benefiting from his numerous informed advice in the fields of geometric modeling, image processing, statistics and machine learning (among others) applied to ophthalmology. In addition, my publications would not have been possible without his generous support for journal's redaction, submission and revision.

I would also express my sincere thanks to Dr. Isabelle Brunette for providing me with the precious ready-to-use clinical database of corneal topographies on which this research project is based and for her useful help for the clinical interpretation of topographies.

I also express my sincere gratitude to the QVRN (Quebec Vision Research Network), the FRQNT (Fonds de recherche du Québec Nature et Technologie) and the MUTAN (University Mission of Tunisia in North America) for financing this project. I was pleased to learn of my selection for this honor and I am deeply appreciative of your support.

I would like to give special thanks to my colleague Claude Alie, Ph.D. in educational psychology from McGill University for our useful discussions regarding statistics, English writing and reasoning.

I am further grateful to Hayder Allkhenfr, physician student from the New York Institute of Technology, for his continuous support along my journey and for the precious discussions we had about my clinical research.

Many thanks should also go to the DESI (direction of education in computer services) of the University of Montreal for the experience I could acquire as an auxiliary teacher in numerous fields of computer sciences (databases, python, C++, web development, etc.).

Last, a special feeling of gratitude goes to my loving parents Ali Belhaouane Bouazizi and Zounaikha Raddadi, whose words of encouragements and push for tenacity ring in my ears. Both of you have been my best cheerleaders. My sister Nahed and my brothers Haykel and Karim have never left my side and are very special to me.

# Content

# LIST OF FIGURES

# List of Tables

# List of Abbreviations

| | |
|---|---|
| ACD | Anterior Chamber Depth |
| Ad | Anterior chamber depth (Chapter 5 only) |
| Ag | Age (Chapter 5 only) |
| Am | Ametropia |
| As | Astigmatism |
| ATR | Against-The-Rule astigmatism |
| BFS | Best-Fit Sphere |
| CHM | Curvature of the Horizontal Meridian |
| Co | Cosinus-axis(Chapter 5 only) |
| CVM | Curvature of the Vertical Meridian |
| Cy | Cy (Chapter 5 only) |
| F | Female |
| K | Keratometry |
| Ge | Gender (Chapter 5 only) |
| KNN | K-Nearest Neighbors |
| LM | Levenberg-Marquardt |
| M | Male |
| MFS α | Minimum Fully Successful α |
| ML | Machine Learning |
| OD | Oculus Dexter |
| OS | Oculus Sinister |
| P | Polynomial |
| R | Rational functions |
| RMSE | Root Mean Square Error |
| SE | Spherical Equivalence |
| SH | Spherical Harmonics |
| SHP | Spherical Harmonic Polynomials |
| SHR | Spherical Harmonics Rational functions |
| Si | Side (Chapter 5 only) |
| Sn | Sinus-axis (Chapter 5 only) |
| Sp | Sphere (Chapter 5 only) |
| VCD | Vertical Corneal Diameter |
| WCSS | Within-Cluster Sum of Squares |
| Wt | White-to-white (Chapter 5 only) |
| WTR | With-The-Rule astigmatism |
| WTW | White-To-White |
| Z | Zernike |
| ZP | Zernike Polynomials |
| ZR | Zernike Rational functions |

# INTRODUCTION

In ophthalmology, an accurate examination of the three-dimensional corneal shape is essential in the diagnosis of corneal diseases, in planning surgery or for patient follow-up after treatment or surgery. Designed as a diagnostic aid for ophthalmologists, corneal topographers have experienced great technological advances in recent years, which allow them to produce increasingly accurate 3D representations of the shape of the cornea. However, to assess the cornea of a patient, it is first necessary to know what the shape of a normal healthy corneal is.

One problem with the specification of the normal cornea is that a corneal topography consists of tens of thousands of data points from the corneal surface. This overabundance of data requires dimensionality reduction to enable various applications, such as cornea-based biometric recognition and computer-aided corneal diagnosis. Geometric modeling can be instrumental to this end. Another issue is the significant variability of the shape of the cornea within a normal population. This variability is better studied by classifying corneal surfaces into different categories. This classification can be conducted under supervision by applying (manually or automatically) a number of clinical parameters, or otherwise without supervision, by clustering. In either case, statistical techniques (mean comparisons) and visualization techniques (group maps) can be instrumental to highlight the central tendencies that emerge from the corneal surfaces of different categories and follow their transformations from one category to another.

Another problem with the specification of the normal cornea is to investigate the variability of the corneal shape to examine the complex relationship that holds between the corneal shape (conceived as a matrix of elevations) and the factors known to affect this shape, including geometric variables, refraction variables and demographic variables. In so doing, one should be able to predict the shape of the cornea based on such factors, and recent machine learning techniques of regression should be helpful in this regard. If the predictions are accurate, the central tendencies of corneal surfaces should be replicated in the predicted corneal surfaces, as visualized with the same visualization techniques.

This thesis is composed of a collection of four papers that address the above problems, preceded by some basic notions and a review of the literature, as follows.

Chapter 1 presents fundamental notions associated with this research and a brief review of the literature. Some basic concepts on the anatomy of the cornea, corneal topography, geometric models and machine learning methods are presented.

Chapter 2 presents a study that explores geometric modeling as a method of dimensionality reduction for machine learning tasks. Four geometric models are compared for their effectiveness at reducing the dimensionality of a dataset of corneal surfaces. These include two polynomial models (Zernike polynomials and spherical harmonics) and two rational function models based on the former (Zernike rational functions and Spherical Harmonic rational functions). This study focuses on small numbers of coefficients to minimize the dimensionality of the prepared datasets. The goal of this study is to assess how the polynomial and rational function models under study perform with a small number of coefficients, considering their accuracy and processing time. The issue is to specify the strengths and weaknesses of each of these models for dimensionality reduction.

Chapter 3 is concerned with the classification of corneal surfaces into a number of clinical categories (clinical classification) and with the visualization of the central tendencies of the surfaces in these categories using an atlas of average elevation maps. In the context of machine learning projects, the creation of such an atlas can be instrumental for validation purposes (ground truth), as concerns the inputs of machine learning (ML) tasks (to assess the conformity of the datasets after their preprocessing) or their outputs (to assess the clinical conformity of clusters, predictions, etc.), or else for interpretation purposes (to better understand the evolution, say, from one cluster to another). To construct such an atlas, we use a dataset of corneal surfaces previously preprocessed by geometric modeling to reduce their dimensionality to a small number of coefficients. The

modeled surfaces are then grouped in accordance with different clinical variables generated by the topographer. For each variable, the surfaces of each group are averaged (by obtaining the means of their modeling coefficients) and the average surface obtained is reconstructed based on these mean coefficients and represented in an elevation map. Using a gradient of colors, the average elevation map of each group of a clinical variable highlights the mean disparities of shape between a corneal surface and the sphere that fits it best and how these mean disparities evolve from one group to another. The atlas is then clinically verified both quantitatively, by assessing the conformity of the dataset of normal corneas with the clinical literature on the different clinical categories investigated, and qualitatively, by examining the corneal shape transformations displayed in the group average maps of each clinical variable.

The two first studies dealt with the dimensionality reduction of corneal data and with the visualization of the effects of their clinical parameters with an atlas of average elevation maps, as a preparation for machine learning applications. Chapter 4 is concerned with the unsupervised classification of normal anterior corneal surfaces (the focus is usually on irregular surfaces) to identify the clinical features that best explain their distribution. Different types of clustering methods are examined in pretests, including hard and soft linear and nonlinear methods, and the modeled surfaces may have their dimensionality further reduced by feature extraction. The evaluation of clusters is based on scores of cluster delimitation (compactness and separation) and on the visualization of the average corneal surfaces of each cluster (clustering atlas) and of their modeling coefficients (polar and scatter plots). Once the best method is identified based on the above evaluation tools, the issue is to identify the best clusters, and in so doing, specify their number ($k$) and the clinical criteria on which these clusters are based.

As a second machine learning application, Chapter 5 presents a regression study on whether corneal shapes can be predicted based on clinical information. Regression analyses are based on anterior corneal surfaces modeled with different numbers of Zernike coefficients (the targets) and on different combinations of geometric, refraction and demographic corneal variables (the predictors). The regression methods examined are nonparametric methods borrowed from the scikit-learn library (gradient boosting, Gaussian process, kernel ridge, random forest, k-nearest neighbors, bagging, and multilayer perceptron). The best model is identified based on RMSE scores that specify for each tested model (method + predictors + targets) the distance between the predicted and true surfaces. Once identified, the best model is qualitatively assessed based on an atlas of average elevation maps. The predictions are accurate to the extent that the RMSE scores are good and the average predicted surfaces of the atlas are visually similar to the true surfaces, to the extent that the shape transformations displayed in the atlas agree with the literature.

The general thesis conclusion follows that suggests possible applications and future research directions. Figure 0.1 summarizes the main articulations of the thesis. It starts with a step of data acquisition in which raw topographic true corneal surfaces are acquired and cleaned in the form of 91×91 matrices of elevations. The raw corneal surfaces are then preprocessed by geometric modeling to obtain a dataset of corneal surfaces modeled with $J$ Zernike coefficients for machine learning projects of clustering and predictions. Different geometric models are tested in Chapter 2 to assess their respective strengths and limitations. Although not the most accurate, Zernike modeling remains a good choice for exploratory studies of clustering and predictions involving normal corneas and will be selected for the following. As another preparatory step for machine learning applications, a task of (manual) supervised classification is accomplished to get an atlas of average elevation maps across a number of clinical categories for validation and interpretation purposes. Two machine learning projects are then conducted: an unsupervised classification project (clustering), to identify the natural groupings of normal corneal surfaces based on the distribution of data, and a regression project, to predict corneal surfaces based on clinical information. The inputs (datasets) and outputs (clusters and predictions) are validated based on a number of evaluation tools, including the atlas of corneal surfaces.

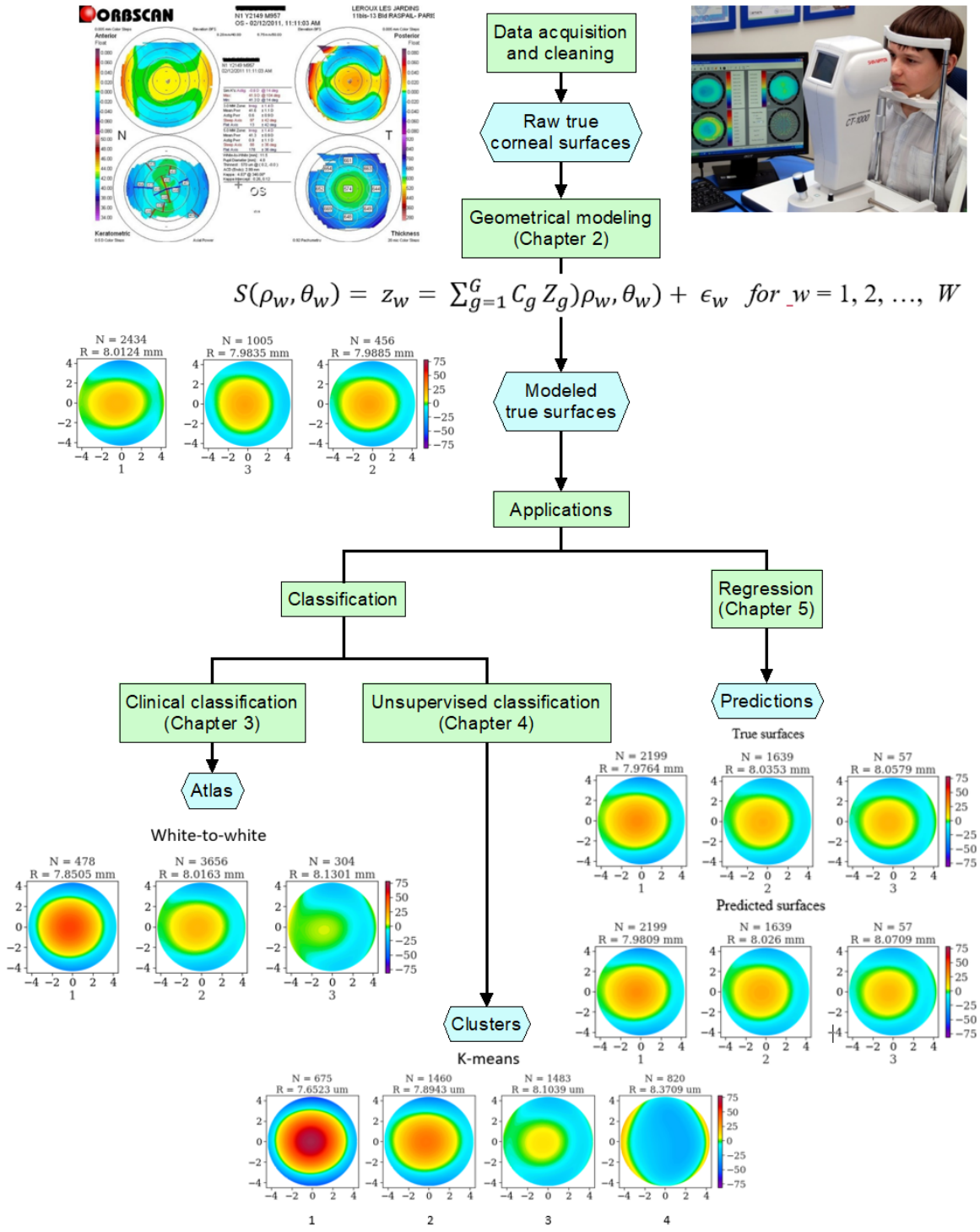


FIGURE 0.1: Flowchart of operations on corneal surfaces in the thesis.

# CHAPTER 1: BASIC CONCEPTS AND REVIEW OF LITERATURE

This chapter presents a number of fundamental notions associated with this research with a focus on the anterior surface of normal corneas. These include: the cornea and related notions, the geometric modeling of corneal surfaces, their clinical classification and visualization of their central tendencies, their clustering, and their prediction.

## 1.1. The cornea and related notions

### *1.1.1. The cornea*

The cornea is the external lens of the eye. It has a nearly spherical shape and covers approximately one-fifth of the eyeball surface, with an average diameter of 11 mm (Figure 1.1). Providing about 65 to 75 percent of the focusing power of the eye, it consists of a transparent tissue in front of the eye that refracts light and facilitates vision. This tissue involves five layers, namely, from front to back: the corneal epithelium, Bowman's layer, corneal stroma, Descemet's membrane, and corneal endothelium. Although nearly spherical, a healthy cornea can involve irregularities that lead to image distortion or aberration and thus to some visual defects, such as myopia or hyperopia. Irregularities cause light to spread out over a diffuse region of space instead of converging to a single point. Two categories of aberrations exist: lower-order and higher-order aberrations. Lower-order (or second order) aberrations make up approximately 85 percent of all aberrations in an eye. They consist primarily of defocus – nearsightedness (myopia) and farsightedness (hyperopia) – as well as astigmatism. Higher-order aberrations are more complex refractive errors and comprise many varieties of aberrations, such as coma, trefoil and spherical aberration.

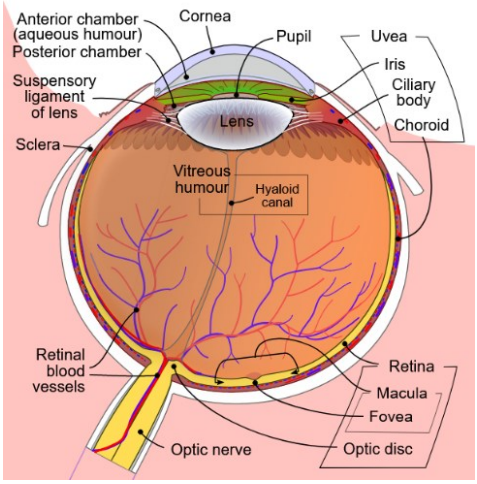


FIGURE 1.1: Cross-sectional view of the eyeball. Source [1].

### *1.1.2. The corneal topographer*

Recent progress in anterior segment imaging has improved the ability to accurately measure several corneal features. Corneal topography (Figure 1.2 and Figure 1.3) is a medical imaging technique used to obtain a precise 3D shape of a cornea as a set of 3D points of its anterior and posterior surfaces. From these data, topographic maps (Figure 1.2) can be derived to assist the ophthalmologist in the diagnosis of disorders.

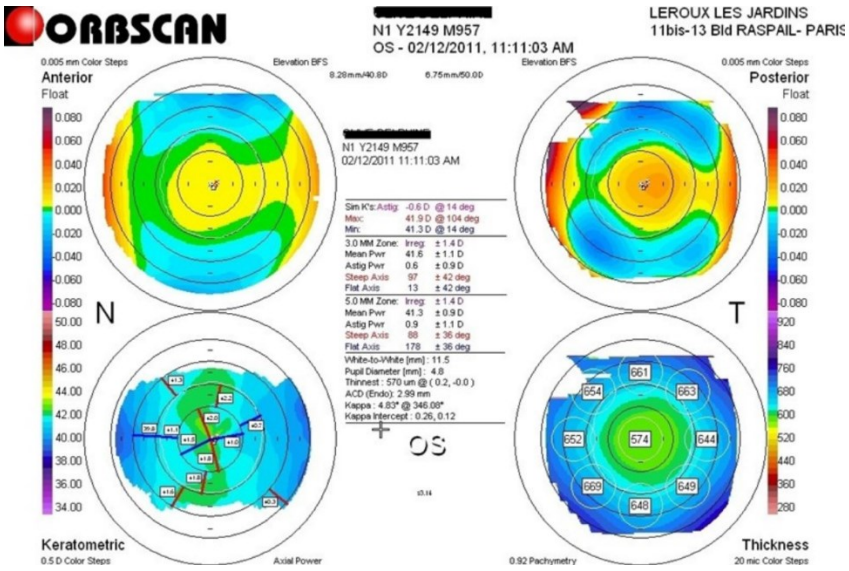


FIGURE 1.2: Typical display of a corneal topographer showing information about the corneal 3D shape. Source [2].

The anterior and posterior elevations with respect to the best-fit sphere (BFS) are shown in the top left and right images, while the curvature and pachymetry (thickness) are shown in the bottom left and right images. The BFS is the sphere that is best fitted to the corneal surface.

Because the shape of the cornea is close to a sphere, the difference between the least-square BFS is shown with a colormap where warm colors indicate positive differences (outside the BFS) and cold colors indicate negative differences (inside the BFS) [3].


FIGURE 1.3: The corneal topographer Orbscan II. Source [4].

The studies presented in this thesis are based on a database that was collected using the Orbscan II corneal topographer [5]. The Orbscan II topographer resorts to slit scanning in combination with

Placido disc technologies to collect information about the elevations of the anterior surface and about the thickness of the cornea, allowing it to reconstruct the posterior surface as well (Bausch and Lomb, Rochester, NY) [3]. This database was made available for both right (OD) and left (OS) eyes under the supervision of Dr. Isabelle Brunette in the Department of Ophthalmology, Maisonneuve-Rosemont Hospital, Montreal, Quebec, Canada.[1]

### *1.1.3. Clinical parameters – Basic definitions*

Each topography of the database of normal anterior corneal surfaces used in this study was associated with a number of clinical parameters, including *demographic parameters* (the age and gender of each subject for which a topographic acquisition was made) as well as *corneal shape* and *refraction parameters*.

*Geometric parameters.* The *best-fit sphere* (BFS) is the sphere that best fits the particular cornea under study. It is characterized by a radius (BFS R) and the coordinates of its *center*. The *white-to-white distance*, also known as the *white-to-white diameter*, is the limbus-to-limbus distance and corresponds to the white-to-white breadth of the cornea. The *anterior chamber depth* is the distance from the central anterior corneal epithelium to the anterior crystalline lens capsule.

*Refraction parameters. Refraction* is the process, achieved mainly by the cornea, by which the light is bent to produce a focused light beam on the retina. *Corneal refractive power* refers jointly to the degree of visual acuity and to the optical properties of visual mechanisms that support vision. An *optical aberration* is a lack of refractive power caused by a failure of light rays to converge on the retina and to set the point of focus on it, thus creating refractive errors that result in a distorted image. *Low-order aberrations* are the most common types of optical aberrations that people may experience to varying degrees (85 percent of all aberrations in an eye). They include *ametropia*, which arises when the vision is out of focus (too short or too long), and *astigmatism*, which occurs when the cornea is not spherical enough. *Ametropia* can take either the form of *myopia* (nearsightedness, when the light beam falls short from the retina) or *hyperopia* (farsightedness, when it falls beyond the retina). Ametropia is measured in diopters in terms of *spherical equivalent*, which is calculated by adding the sphere power with half of the cylinder power: it is negative for myopia and positive for hyperopia. *Astigmatism* is measured in terms of the cylinder and axis. The *cylinder* specifies the degree of astigmatism of the eye by stating how flat or spherical it is. The *axis*, measured in degrees from 0° to 180°, gives the orientation of the astigmatism by specifying the angle of the main axis of the corneal deformation (the degree of corneal rotation): approximately 0° or 180° (± 30°), the cornea is similar to a rugby ball on its side, and we have "with the rule" astigmatism; approximately 90° (± 30°), the cornea is similar to a rugby ball on its end, and we have "against the rule" astigmatism; between these values, we have oblique astigmatism.

Other clinical parameters of corneal shape were not directly provided by the database but could nevertheless be qualitatively observed in the elevation maps. The *corneal curvature* is the overall steepness of the curvature of the cornea [6]. It can be measured as the *radius of curvature* of the cornea. The BFS radius can give an approximation of it. Literally, the *asphericity* of the cornea is the difference with the perfect sphere that best fits it [6]. In a more specific sense, it refers to the rate of change of the corneal curvature from the center to the periphery and is designated as $Q$.

With an elevation map, the asphericity can be observed in relation to the BFS by a variation in color indicating a variation in distance [3].

[1] Given the focus of the present thesis on the anterior surface and the tasks at hand, the need for the more recent technology of the Pentacam was not as important as the need to have access to a sizable database of corneal surfaces, currently available only with the Obscan II.

### *1.1.4. Clinical parameters – Effects on the corneal shape*

The clinical parameters described above produce a number of effects on the corneal shape.

*Geometric parameters*

*BFS R.* The radius of the BFS of corneal surfaces is positively related to the degree of curvature of the horizontal and vertical at the apex (CHM and CVM) [3].

*WTW.* The white-to-white diameter (WTW), also known as horizontal corneal diameter (HCD) or horizontal visible iris diameter (HViD), strongly correlates with the radius of horizontal curvature (and thus negatively correlates with the curvature of the horizontal meridian [7]), which itself strongly correlates with the BFS R [3,7].

*ACD.* The anterior chamber depth (ACD) is negatively related to the keratometry (central corneal curvature, or *K*) [8], and to the spherical equivalent (SE) [9].

*Side.* Side as a predictor is associated with an interocular horizontal symmetry between OS and OD corneal shapes [10,11]. This property (enantiomorphism) is not affected by age, gender or spherical equivalent (SE). An intraocular corneal asymmetry of asphericity also arises for each eye, with more flattening occurring nasally than temporally [10].

*Refraction parameters*

*Ametropia.* An increase in spherical equivalent (SE) from myopia to hyperopia is associated with a flatter curvature of the horizontal meridian (CHM) [11,12], and a shallower anterior chamber depth (ACD) [9,13]. From high myopia to emmetropia, an increase in SE is also associated with larger corneal horizontal and vertical diameters [11], themselves related to a larger best-fit sphere radius (BFS R) [7,14].

*Astigmatism.* "With the rule" (WTR) astigmatism arises when the axis of the cornea is rather horizontal (the axis angle is between 0° and 30° or between 150° and 180°). This is the case when the curvature of the vertical meridian (CHM) is the steepest and the curvature of the horizontal meridian (CHM) is the flattest [15,16]. The cornea is then similar to a rugby ball on its side. "Against the rule" (ATR) astigmatism arises when the axis is rather vertical (the axis angle is 90° ± 30°). The CHM is then the steepest and the CVM the flattest. Finally, oblique astigmatism arises when the axis is neither roughly horizontal nor roughly vertical (the axis angle is between 30° and 60° or between 120° and 150°).

*Demographic variables*

*Age.* This factor has been related to a variety of changes relative to the shape of the anterior surface of the cornea, including a shift from a "with the rule" to "against the rule" astigmatism that translates into an increase in the curvature of the horizontal meridian (CHM) and a decrease in the curvature of the vertical meridian (CVM) and thus an increase in the axis angle [15,16,17,18]. A decrease in vertical corneal diameter and white-to-white distance (VCD and WTW) is also observed when different age groups are compared to elderly people from 70 to 79 yo [11]. Age is further related to a reduction in anterior chamber depth (ACD) [8,13,20,21]. Concerning refraction, the prevalence of myopia is generally lower in older adults than in young adults [22]. For hyperopia, its prevalence starts to increase at approximately 35-40 years old until 65 years old or so [23].

*Gender*. Males have generally a wider anterior white-to-white diameter (WTW) [7,11,19] and thus a flatter horizontal and vertical corneal curvature [11,14,19] and a larger BFS radius [3,14], as well as a deeper anterior chamber depth (ACD) [8,20,24]. Besides, adult females have a higher prevalence of myopia than adult males and a lower prevalence of hyperopia, and thus a lower SE [25].

## 1.2. Modeling the shape of the cornea

Models of the cornea have taken many forms, evolving from conceptual models to the schematic eye of the Gullstrand model and then to complex computational models that integrate structural, biomechanical and optical representations of the corneal response. Figure 1.4 presents a typology of the most important types of corneal models that have been developed.

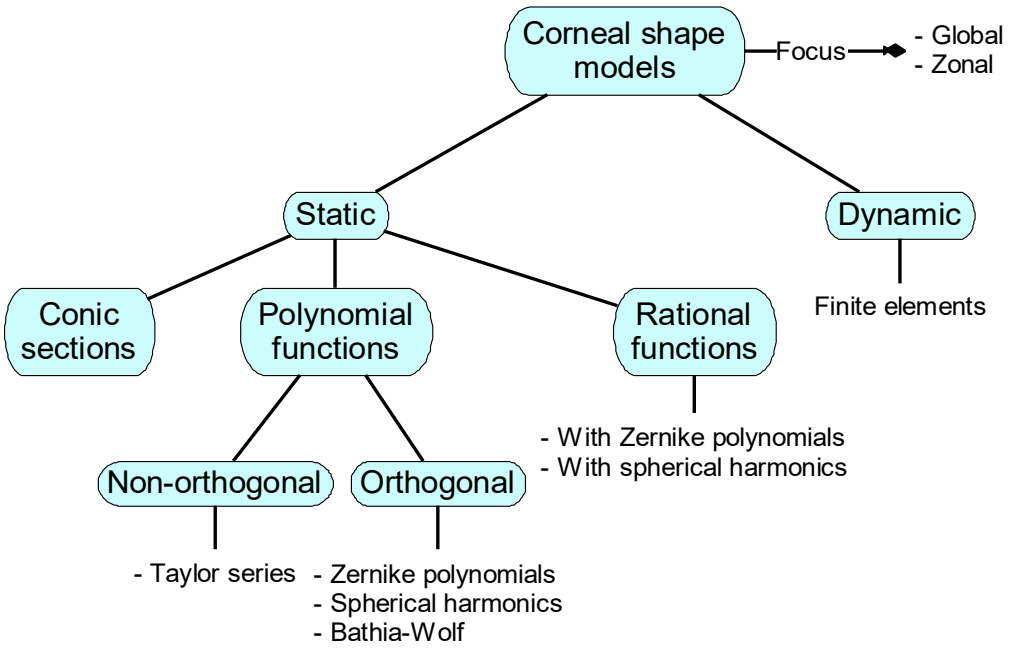


FIGURE 1.4: Typology of corneal shape models.

### *1.2.1. General distinctions*

*Static vs. dynamic models.* A first distinction is made between *static* and *dynamic* corneal shape models. Static models are geometric models that consider the cornea as a steady-state system in which stable input–output relationships are established. In contrast, dynamic models are aimed at describing successive time-related states of the system through differential equations or through successive state-change equations.

*Global vs. zonal static models.* In modeling the shape of the cornea, one may either consider it globally, producing a single model that represents the whole corneal surface, or locally, iteratively splitting the corneal surface into a number of modeling zones, or patches, and producing a number of models – one for each patch – that are integrated to represent the whole surface. The optimal number of patches is obtained by iteratively splitting the surface at specific control points until an accuracy or iteration criterion is satisfied.

The models of corneal shape used in the studies presented in Chapter 2 are both static and global. They are static since we are only interested in representing the shape of the cornea as opposed to its evolution. They are global given that we want simple models (used for data compression) in ML tasks, which must be as parsimonious as possible as the number of coefficients required to achieve a certain degree of accuracy. Different types of static global models have been developed, including conic section models, polynomial models, which are of particular interest here, and rational function models.

### *1.2.2. Conic section models*

A conic section is obtained by cutting a cone with a plane at different angles to get different geometric shapes, including spheres, ellipses, hyperbolas and parabolas [26]. A typical conic section model of the cornea defines the profile of the cornea as an ellipse using two parameters, namely the apical radius *R* and the eccentricity parameter *e*, as in Equation 1.1.

$$y = 2Rx - (1 - e^2)x^2 \tag{1.1}$$

A more intuitive way to formulate this expression is as follows:

$$y = 2Rx - px^2 \tag{1.2}$$

where

$$p = 1 - e^2 = \left(\frac{b}{a}\right)^2 \tag{1.3}$$

in which *a* and *b* are the horizontal and vertical semi-axes of the ellipse. With this information, one can establish whether the elliptical shape of the cornea is circular (like a standard ball), prolate (like a rugby ball) or oblate (like a round cushion) as follows. Assuming that $p > 0$ (we then have an ellipse): if $p < 1$ then $a > b$ and the ellipse is prolate; if $p > 1$ then $b < a$ and the ellipse is oblate; if $p = 1$ then $a = b$ and the ellipse is a circle. Related to these concepts are the notions of eccentricity *E* and asphericity *Q*, defined in Equations 1.4 and 1.5:

$$E = -Q = e^2 \tag{1.4}$$

This 2D modeling of the cornea can be extended to 3D modeling as in Equation 1.5, in which *z* is further accounted for (assuming the absence of toricity):

$$x^2 + y^2 + pz^2 - 2Rz = 0 \tag{1.5}$$

More complex conic section models involve accounting for the toricity of the ellipse using a biconic model [3]. While other models, such as polynomial expansions, can be even more precise than conic sections (see below), they are mathematically more complex. In most cases, conic and biconic section models remain sufficient for the functional study of the cornea.

### *1.2.3. Non-orthogonal polynomial models*

Taylor series are based on the decomposition of the corneal shape into simple radial polynomials [27]. However, Taylor series do not satisfy the condition of orthogonality allowing models to be easily expandable and interpretable, as required for ML applications based on corneal shape modeling.

### *1.2.4. Orthogonal polynomial models*

An orthogonal polynomial function is a linear combination of terms with an orthonormal radial basis, as specified in Equation 1.6:

$$S(u_w, v_w) = h_w = \sum_{g=1}^{G} C_g P_g(u_w, v_w) + \epsilon_w \quad \text{for } w = 1, 2, \ldots, W \tag{1.6}$$

where the corneal surface *S* consists of a set of *W* (polar or spherical) elevation $S(u_w, v_w)$ that are located at (polar or spherical) coordinates $u_w$ and $v_w$ for $w = 1$ to *W*. Each elevation $S(u_w, v_w)$ (equivalently $h_w$) is modeled as the sum of the product of the $g^{th}$ polynomial $P_j(u_w, v_w)$ and coefficient $C_g$ for $g = 1$ to *G*, assuming error $\epsilon_w$. The first coefficient ($C_1$) specifies the mean

elevation of the modeled surface while the subsequent coefficients ($C_1$ to $C_g$) define its shape [28,29].

The polynomial terms of an orthogonal polynomial function are not correlated (orthogonal) and have the same unit length (normalized). The modeling of spheroid objects then consists solely of specifying the desired number of terms of the equation to be optimized to obtain the vector of optimal coefficients associated with these terms. As the vector of coefficients are the only elements that need to be stored to reconstruct a modeled quasi-spheroid surface, the step of model fitting can be regarded as a compression procedure.

Three types of orthogonal polynomial functions have been extensively studied in corneal surface modeling, namely Zernike polynomials, spherical harmonics, and Bathia-Wolf polynomials. However, Bouazizi et al. (2017) have shown that while Bathia-Wolf polynomials are as effective as Zernike polynomials for a given radial order, they involve more coefficients for the same radial order and as such are less parsimonious [30]. Accordingly, this study focuses only on Zernike polynomials and spherical harmonics.

*Zernike polynomials*

In 1995, Schwiegerling made a clear demonstration of the interest of Zernike polynomials for the modeling of corneas [31], a finding replicated by Iskander et al. in 2001 when comparing this model to Bathia-Wolf [32]. In Zernike polynomials, the shape of the corneal surface is defined as a linear combination of simpler spheroid surfaces, or basis functions. This linear combination specifies Equation 1.6 as in Equation 1.7:

$$S(\rho_w, \theta_w) = z_w = \sum_{g=1}^{G} C_g \, Z_g(\rho_w, \theta_w) + \epsilon_w \quad \textit{for } w = 1, 2, \ldots, W \tag{1.7}$$

The corneal surface $S$ consists of $W$ polar elevations $S(\rho_w, \theta_w)$ (equivalently $z_w$) located at polar coordinates $\rho_w$ and $\theta_w$ for $w = 1$ to $W$. Each polar elevation $z_w$ is modeled by summing the product of the $g^{th}$ Zernike polynomial $Z_g(\rho_w, \theta_w)$ and the $g^{th}$ coefficient $C_g$ for $g = 1$ to $G$, assuming error $\epsilon_w$. Each Zernike basis function $Z_g(\rho_w, \theta_w)$ represents a particular type of optical aberration. With Zernike polynomials, each polynomial term is associated with a corneal feature. Using Noll sequential indices, we have for $g = 1$: piston, 2: horizontal tilt, 3: vertical tilt, 4: defocus, 5: oblique astigmatism, 6: vertical astigmatism, 7: vertical coma, 8: horizontal coma, etc. As radial series expansions, Zernike polynomial models display properties of completeness (being potentially capable of accounting fully for the true surface), orthonormality (being uncorrelated and normalized), radiality (representing spheroids), and linearity. These properties make them easily interpretable, flexible for deciding the optimal number of coefficients needed, and suitable for the use of fast exact methods of optimization, such as least squares. However, their use may be problematic for the modeling of corneal surfaces presenting high-level aberrations, as for post-surgery corneas [29,33,34].

*Spherical harmonics*

In 2009, Iskander et al. proposed using spherical harmonics to model the cornea [34]. Similar to Zernike polynomials, spherical harmonics consist of a complete set of orthonormal periodic functions defined on the surface of a unit sphere. These functions are expressed as a sum of circular functions (sines and cosines) in accordance with Equation 1.8, which specifies Equation 1.6 as follows:

$$S(\theta_w, \varphi_w) = \rho_w = \sum_{g=1}^{G} C_g \, SH_g(\theta_w, \varphi_w) + \epsilon_w \quad \textit{for } w = 1, 2, \ldots, W \tag{1.8}$$

The surface $S$ consists of $W$ spherical elevations $S(\theta_w, \varphi_w)$ positioned at spherical coordinates $\theta_w$ and $\varphi_w$ for $w = 1$ to $W$. Each spherical height $S(\theta_w, \varphi_w)$ (equivalently $\rho_w$) is a radius modeled as the sum of the product of the $g^{th}$ spherical harmonics $SH_g(\theta_w, \varphi_w)$ and coefficient $C_g$ for $g = 1$ to

*G*, assuming error $\epsilon_w$. For Equation 1.8 to apply properly, corneal surface data must first be centered in relation to a spherical reference, the best-fit sphere (BFS), which is located on the origin of the coordinate system and is normalized to a unit sphere. The spherical information of the modeled surface is contained in the first coefficient (mean radius coefficient), while the next coefficients represent the relative deformations with respect to this sphere.

In their study, Iskander et al. showed that spherical harmonics provide a better fit to true corneal surfaces than Zernike polynomials with the same radial order. In particular, Zernike polynomials were deemed to be insufficient for the modeling of complex corneal surfaces presenting higher-order aberrations, such as those encountered in postsurgical eyes. In [34], Iskander compared SH polynomials with 3D polynomial functions, such as hemispherical harmonics and 3D Zernike (3DZ) polynomials, and found that SH achieves better accuracy in modeling the shape of the cornea for the same radial order and a same number of coefficients.[2] However, these studies were limited to a relatively small number of corneas.

### *1.2.5. Rational function models*

A rational function is the ratio of two polynomial surfaces acting as the numerator and denominator, as shown in Equation 1.9:

$$S(u_w, v_w) = h_w = \frac{S^N(u_w, v_w)}{S^D(u_w, v_w)} + \epsilon_w \quad \textit{for } w = 1, 2, \ldots, W \tag{1.9}$$

where the surface *S* consists of *W* polar or spherical elevations $S(\theta_w, \varphi_w)$ (or equivalently $h_w$) positioned at spherical or polar coordinates $u_w$ and $v_w$ for $w$ = 1 to *W*. Each spherical height $h_w$ from 1 to *W* is modeled as the ratio of a modeled numerator polynomial surface $S^N(u_w, v_w)$ and a modeled denominator polynomial surface $S^D(u_w, v_w)$, assuming error $\epsilon_w$. In the present study, the numerator (*N*) and denominator (*D*) polynomial surfaces can be either Zernike polynomials (defined in Equation 1.7) or spherical harmonics (defined in Equation 1.8). The set of rational function coefficients $C^R$ is simply the union of the set of numerator coefficients and denominator coefficients.

Schneider et al. (2009) found that Zernike polynomial-based rational functions outperform traditional Zernike polynomials with the same number of coefficients after a minimum number of coefficients has been reached [35].

### *1.2.6. Optimization of corneal shape models*

The best set of coefficients of a geometric model of corneal shape must be identified by solving a cost function *F(ϵ)* of the form:

$$\hat{C} = F(\epsilon) = arg \min_{C \in \{C\}} \left( \sum_{w=1}^{W} \epsilon_w{}^2 \right) \tag{1.10}$$

where *C* is a set of coefficients among the superset of all those tested $\{C\}$, $\hat{C}$ is the set of coefficients among those tested that produces the lowest error when applying the cost function, *D* is the number of data (here, the number of elevation points of the modeled surface), and $\epsilon_w$ is the error of the $w^{th}$ modeled elevation. Each error $\epsilon_w$ is measured as the distance between the $w^{th}$ elevation of the modeled surface and that of the true surface:

[2] The matching between the radial orders and numbers of coefficients of ZP and SHP models was achieved by taking only the right side of the SH coefficient pyramid. However, the finding that SHP performed better than ZP for the same number of coefficients was confirmed by Bouazizi et al. (2017) with both the right and the left sides of the SH coefficient pyramid being considered.

$$\epsilon_w = S^M(u_w, v_w) - S^T(u_w, v_w) \quad for\ w = 1, 2, \ldots, W \tag{1.11}$$

where $S^T(u_w, v_w)$ is the $w^{th}$ elevation of the true surface $S^M(u_w, v_w)$ and the $w^{th}$ elevation of the modeled surface. Each modeled surface elevation is defined as in Equation 1.6 (without $\epsilon_w$), and thus as in Equation 1.7 for Zernike polynomials and as in Equation 1.8 for spherical harmonics.

Different types of optimization methods can be applied, as summarized in Figure 1.5 for those of the SciPy Optimize library [36].

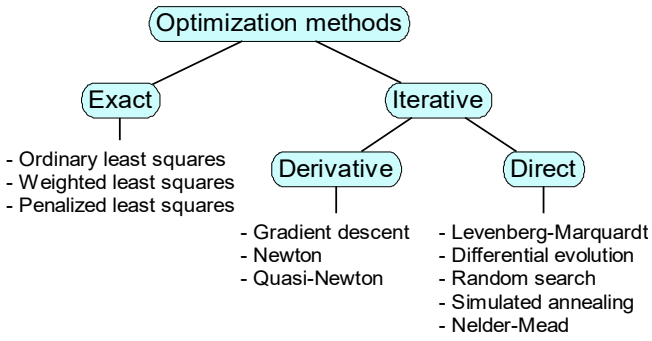


FIGURE 1.5: Typology of optimization methods.

An *exact optimization method* is one that can arrive directly and exactly, by simple calculus (usually least square calculus), to the best set of coefficients. In contrast, an *iterative optimization method* cannot do so and must instead proceed by successive approximations of the best set of coefficients, which are iterated until no significant progress toward this best set of coefficients can be made according to some stopping condition. When applicable, the use of an exact optimization method is always preferable, given its exactness and high speed, but this is not always the case: while polynomial models are suitable for this, rational function models must instead apply a much more demanding iterative method.

*Polynomial model optimization*

The best known exact optimization method for polynomial models is ordinary least squares, in which the best set of coefficients $\hat{C}$ is solved by calculating the Moore–Penrose pseudoinverse:

$$\hat{C} = (PM(u, v|C)^{\mathrm{T}}\ PM(u, v|C))^{-1}\ PM(u, v|C)^{\mathrm{T}}\ T(u, v) \tag{1.12}$$

Ordinary least squares can be amended by adding weights (weighted least squares) and/or a penalty (penalized least squares, such as Lasso or ridge regression). However, such amendments do not produce any change with corneal modeling (as verified in preliminary tests for the study on compression presented in Chapter 1), so ordinary least squares is suitable for the optimization of polynomial models of corneal surfaces.

*Rational function model optimization*

Being nonlinearizable, rational function models cannot provide a Moore–Penrose pseudoinverse and must accordingly be optimized with an iterative method. Among them, *derivative optimization methods* rest on the estimation of the curvature of the cost function, using a Jacobian matrix, as with gradient descent methods, or else a Hessian matrix, as with Newton methods. When the Hessian matrix cannot be computed, it can be approximated, as with quasi-Newton methods. Otherwise, *direct optimization methods* can also be used, which do not require any information about the gradient of the cost function but typically use a strategy that randomly generates variations of the design parameter vectors to directly estimate cost variations and get closer to the minimum. For the first article presented in this thesis in Chapter 2 about geometric models and compression, we examined in pretests all the applicable iterative methods available in

the SciPy Optimize library [36]. One of them stood out for its accuracy and speed in processing anterior corneal surfaces, namely Levenberg-Marquardt (LM), which is a derivative method, the same used and recommended by Schneider for the optimization of corneal models with rational function [35]. The LM algorithm is an upgraded version of the Gauss-Newton algorithm formulated as a trust-region algorithm that takes advantage of the gradient descent technique to solve unconstrained nonlinear problems [35,37]. Although it can only find a local minimum, it is more robust than other algorithms for small unconstrained problems if some initialization conditions provide a reasonable pre-estimation of the solution.

## 1.3. Visualization of the effects of clinical parameters on the corneal shape with an atlas of average elevation maps

A number of visualization tools have been developed over the last decades to capture and visualize some properties of groups of corneal surfaces (instead of focusing on a single one at a time). Currently, group maps include average maps, difference maps, count maps, standard deviation maps, t-test maps, pachymetry maps, and diagnosis maps, among others (see [38]). They have been used to visualize the effects produced by a few clinical parameters, including age [38], gender [29,30], spherical equivalent [30], and corneal diagnosis [38]. Once verified for its clinical conformity, an atlas can be used not only for clinical and instructional purposes but also to verify the conformity of datasets used or produced in ML tasks.

Pivotal among them is the average elevation map. In an *individual elevation map*, a single corneal surface is represented in reference to the sphere that fits it the best, the best-fit sphere (BFS). Figure 1.6 (a) shows a 3D representation of an individual anterior corneal surface (in blue) in reference to its BFS (spherical grid). Some areas of the cornea are above the BFS, and others are below it. This fact can be seen even more clearly in Figure 1.6 (c), where horizontal and vertical profile cuts of the same true corneal surface (the meridians) are presented. It is possible, using an elevation map, to represent all the elevations of the corneal surface on a 2D plane, as shown in Figure 1.6 (d) (the meridian elevations are represented by dotted lines). The surface points are located on the $X$ and $Y$ axes of the 91 × 91 grid, and the elevations on the $Z$ axis are represented as a colormap. Warm colors hold for the elevations above the BFS, and cold colors for those below the BFS. In Figure 1.6 (e), the same surface is represented in an elevation map modeled with 24 Zernike polynomials (ZP).

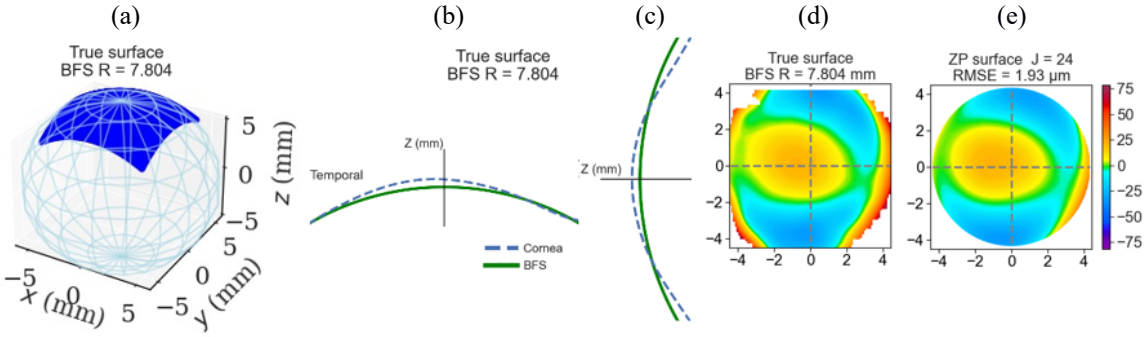


FIGURE 1.6: Representations of a true OD anterior corneal surface in reference to its BFS: (a) 3D map (the surface is in blue, the BFS is represented as a grid; (b) and (c) horizontal and vertical profile cuts (the surface is represented as a dashed curve, the BFS as a solid curve); (d) elevation map of the same true surface, (e) elevation map of the same surface modeled with 24 Zernike coefficients (a 5 mm fringe is radially removed to eliminate the most noisy part of the map).

WTW (group 1: from 10.40 to 11.36 mm, group 2: from 11.36 to 12.32 mm, group 3: from 12.32 to 14.10 mm)

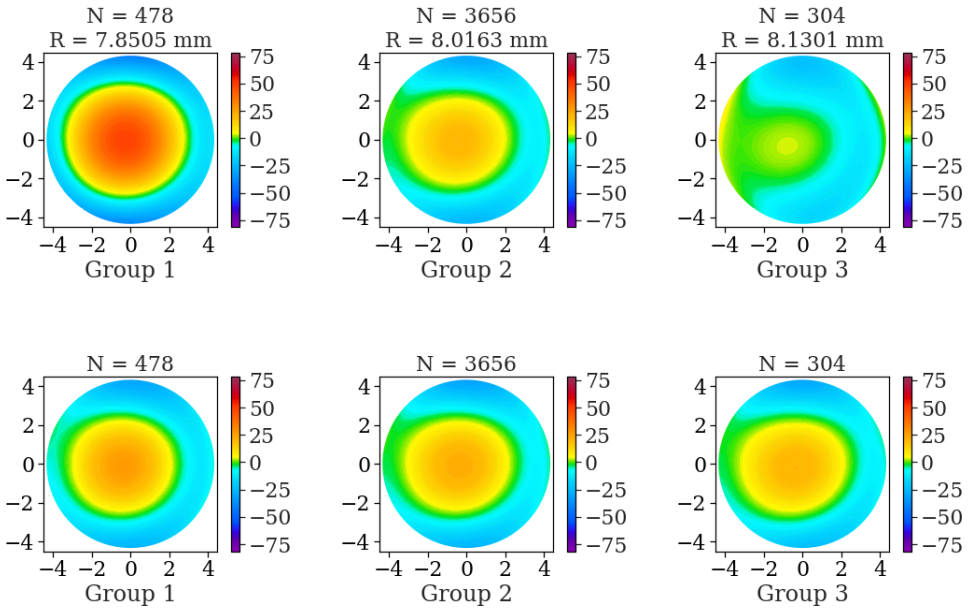


FIGURE 1.7: Average elevation maps for WTW segmented in three groups. In the first row, the maps are based on natural surfaces in reference to the common BFS, and in the second row on normalized surfaces in reference to the normalized BFS. For each WTW group, the average corneal surface is the mean of the corneal surfaces of the group modeled with 16 Zernike coefficients.

An *average elevation map* is a representation with an elevation map of the average surface of a group of surfaces. An *average surface* can be computed by averaging the elevations of the surfaces at each point of the grid, or equivalently, if the surface has been modeled, by averaging the modeling coefficients and constructing a surface based on the mean coefficients. The BFS of reference of an average elevation map is a *common BFS* with natural surfaces, computed as the mean of the group BFS, itself computed as the mean of the BFS of the individual surfaces of the group, or a normalized BFS with normalized surfaces, computed as the mean of the normalized BFSs.

In an *atlas of average elevation maps*, an average map is constructed for each group of different clinical variables (transformed beforehand into categorical variables, if needed). By examining the average elevation maps of a given variable, it is possible to visualize its effect on the corneal shape regardless of its particular manifestations in specific surfaces. For example, Figure 1.7 shows the average elevation maps of WTW with natural (first row) and normalized surfaces (second row). While the difference of curvature caused by the differences in size of the different WTW groups is emphasized with natural surfaces, this difference is neutralized with normalized surfaces to emphasize instead the relative shape of the cornea (which does not change much from one group to another).

## 1.4. Unsupervised classification of corneal surfaces

In unsupervised classification, or clustering, categories are "discovered" based on the distribution of data and the number of categories required ($k$). Once discovered, they form a set of $k$ categories, or clusters, in which the data that are close to each other tend to be grouped together in the same category, while those that are distant from each other tend to belong to different clusters. A number of clustering methods are available: one can distinguish between hard methods (in which one cluster only is assigned to each element of the dataset) and soft methods (in which more than one cluster can be assigned along with a likelihood index of belonging) and between linear methods (in which cluster delimitations are linear) and nonlinear methods. The evaluation of the clusters produced by these methods can be external or internal. In external clustering evaluation, the clusters are evaluated in reference to groups that are already known as to their number ($k$) and to their elements: the $k$ clusters produced are good to the extent that they are similar to the corresponding $k$ groups, which are posed as ground truth. In internal clustering evaluation (adopted in this thesis), there are no already known reference groups posed as ground truth, so the clusters must be evaluated in reference to each other in terms of their delimitation. The clusters are well delimited to the extent that they are compact (the data of a same cluster are close to one another) and separated (the data of different clusters are far from each other). In this case, the number of clusters $k$ and the criterion on which their grouping is based are not prespecified and must be discovered based on their delimitation. To evaluate the quality of this delimitation, a number of techniques are available. The best known, the elbow method, consists in estimating the WCSS score (within cluster sum of squares) for each possible number of clusters $k$ and in locating the elbow of the resulting WCSS curve, where the compactness-separation relationship is optimal. To amplify and clarify the location of the elbow, the $SPR^2$ (semi-partial $R^2$) score can be used instead, either alone or in combination with the $R^2$ score [39]. The $SPR^2$ score is a measure of cluster compactness that computes the differences of successive WCSS scores (the elbow is located where the curve gets quasi-flat). As for the $R^2$ score, it is a measure of cluster separation that computes the between cluster sum of squares in reference to the total sum of square (the optimal k is located at the "knee" of the curve).

Whatever the type of evaluation adopted, clustering methods are designed to optimize the compactness-separation relationship, and their difference lies in the strategy adopted to this end. For example, agglomerative clustering is a hard linear bottom-up method in which clusters are built by recursively grouping data into pairs of clusters until a reversed tree is formed from leaves to root (dendrogram). The grouping of data into clusters is based on a linkage criterion used to identify the grouping that produces the smallest Euclidian distance. The dendrogram is like a pyramid in which the higher is the row of clusters, the lower is the number of clusters $k$. Another hard linear method is k-means clustering, in which the clustering of data proceeds instead downward. The grouping procedure is based on a Voronoi space, which is a partition of a plane into $k$ regions based on a predefined set of points. The borders of these regions are linearly set to minimize the distance between the within-border members, as measured by the within-cluster sum of squares (WCSS). Distance minimization proceeds by assigning each datum to the nearest centroid of each of the $k$ regions, by computing again the location of the centroid of each region, and recursively until the WCSS passes below a quality criterion [40]. Spectral clustering is an example of hard nonlinear clustering method in which a step of feature engineering applies prior to the application of a standard clustering linear method such as k-means. In this step, an affinity matrix is created to provide a set of eigenvalues that inform about the similarity of each pair of data in the dataset. Clustering then proceeds by bipartioning the data in such a way as to maximize the affinity connections of the members of the same group and minimize those of different groups (in other words, by recursively cutting the weakest edges of the affinity matrix).

## 1.5. Prediction of corneal surfaces

The issue in corneal prediction is whether it is possible to predict the shape of the cornea based on clinical data. To this end, one must investigate the complex relationship that holds between corneal shape and clinical data, which is done through regression analysis. In its traditional statistical modality, regression analysis requires one to make an assumption about the shape of the relationship that holds between the predictors and the targets, if it exists (linear, logarithmic, etc.). However, such an assumption rests on knowledge that is not always available. In the paradigm of machine learning (ML), no such assumption needs to be made. The issue is no longer whether a relationship does exist but what is the strongest one to take advantage of it and make the best predictions as possible. Such an approach, though, requires a large amount of data, but fortunately, big databases become increasingly available. While ML studies dealing with corneal shape have been conducted in recent years, most of them are aimed at classification to provide support for clinical diagnosis rather than regression to make predictions about the shape of the cornea. A number of ML regression methods have been proposed. Deep learning algorithms are generally regarded as being particularly effective, but they are extremely resource consuming and not necessarily appropriate for a first approach aimed at exploring and narrowing down the optimization space of regression analysis in corneal shape prediction, especially if a large database is not available. Other effective methods that are more convenient for such initial exploration are available in recent ML libraries along with ready-to-use optimization tools. Figure 1.8 presents such regression methods borrowed from the scikit-learn library that were implemented in the present study [40].

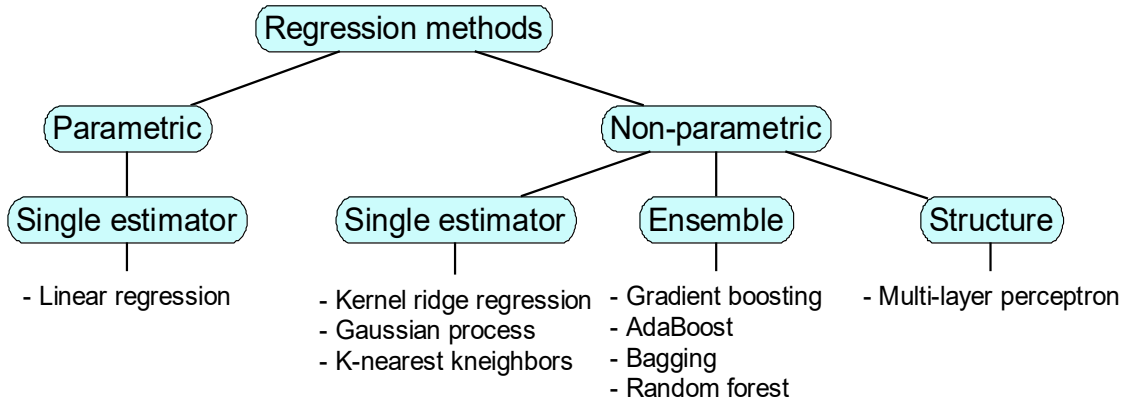


FIGURE 1.8: Regression methods for corneal surface predictions drawn from the scikit-learn library implemented in the present study.

Some of these methods are *parametric*, resting on a well-defined function that applies to data whose distribution is assumed to be known, as is the case of statistical methods. Such methods normally rely on a single estimator (linear regression, ridge regression). Other methods are *nonparametric* when data distribution must be discovered through some more elaborate training technique, as is the case of ML methods. The latter may rely on a *single estimator* (kernel ridge, Gaussian process, k-nearest neighbors), on an *ensemble* in which a collection of weak methods of the same type get their results combined by an integration function (gradient boosting, AdaBoost, bagging, random forest), or else on a *structure* in which the estimators form a complex structure (multi-layer perceptron). Among these regression algorithms, implemented in the scikit-learn library, those that proved to be applicable to the task at hand were linear regression (as a reference method), bagging, random forest, gradient boosting, k-nearest neighbors, kernel ridge, Gaussian process, and multilayer perceptron [40].

*Bagging* is designed as an ensemble of decision trees that rests on a bagging algorithm (a set of independent weak regression methods) to exploit all possible subsets of features. *Random forest* is a similar method that exploits only a selection of all possible subsets of features. Adaboost is also an ensemble of decision trees, but it rests on a boosting algorithm (a set of dependent weak regression methods) to sequentially exploit the feature subsets. *Gradient boosting* does the same as AdaBoost with a gradient descent loss function instead. *K-nearest neighbors*, designed as a single estimator, applies the nearest neighbor selection algorithm (in which the *k* closest neighbors from each example are selected as a basis for the prediction to make with the example). *Kernel ridge*, also designed as a single estimator, applies a ridge regression algorithm with the kernel trick (in which a kernel function is applied to transform a nonlinear space in a linear space of higher dimension to facilitate processing). Gaussian process is a single estimator method that exploits a probabilistic function algorithm based on Gaussian equations. Finally, multilayer perceptron is a structure that supports a process of multilayer propagation, in which the data flow forward from layer to layer and are nonlinearly modulated before the model is retroactively adjusted (backpropagation) through a gradient descent loss function.

These methods can be optimized with two cross-validated parameter search methods, namely RandomSearchCV and GridSearchCV. While the first proceeds by random search to narrow the optimization space, the second proceeds by grid search in the reduced space to get the best features (fine tuning).

# CHAPTER 2: COMPARISON OF POLYNOMIAL AND RATIONAL FUNCTION CORNEA MODELS FOR EFFECTIVE DIMENSIONALITY REDUCTION

Hala Bouazizi[1], Isabelle Brunette[2,3], Jean Meunier [1,2]

1 Department of Computer Science and Operations Research, University of Montreal, Montreal, Quebec, Canada
2 Department of Ophthalmology, University of Montreal, Montreal, Quebec, Canada
3 Maisonneuve-Rosemont Hospital Research Center, Montreal, Quebec, Canada

## Abstract

This study aims to examine some geometric models of the corneal surface that can be used to reduce the dimensionality of corneal surface datasets, with a focus on normal anterior corneal surfaces. To this end, we looked for models that support early convergence in a reasonable processing time. Polynomial models such as Zernike polynomials (ZP) and spherical harmonic polynomials (SHP) were obvious candidates to this end, as well as their rational function counterparts, Zernike rational functions (ZR) and spherical harmonic rational functions (SHR, a new model for the cornea), which were tested for a small number of model coefficients ($J$). Knowing that both SHP and ZR were more accurate than ZP for the modeling of normal and keratoconus corneas, it was expected more largely that both spherical harmonics models (SHP and SHR) would be more accurate than Zernike models (ZP and ZR) and that both rational models (SHR and ZR) would be more accurate than their polynomial model counterparts (SHP and ZP, respectively) for a low dimensional space ($J <$ 30). This was the case, and the SH factor was found to contribute more to accuracy than the R factor. Considering the processing time of corneal surfaces as a function of $J$, a different picture appeared. The increase in processing time was linear for the polynomial models (with a quasi-null slope) but polynomial for the rational models. Zernike models were faster than spherical harmonics models and increasingly so in their rational model version. In sum, for dimensionality reduction tasks involving small $J$ values, SHR is the most accurate model, but its processing time was increasingly prohibitive, indicating that the best combination must be identified before applying it to a large dataset. ZP is the fastest model and is reasonably accurate with normal anterior surface corneas, so it remains useful for exploratory studies and project development. SHP is the best compromise between accuracy and speed.

**Keywords:** cornea, Zernike polynomials, spherical harmonics, rational functions, corneal topography

## 2.1. Introduction[3]

In this study, an attempt is made to provide an accurate and parsimonious geometric model of the corneal surface for effective dimensionality reduction, often a requirement in machine learning or biometric projects in which dimensionality issues may arise. Current corneal shape models include conic section models, polynomial models, rational function models, and spline models, among others [26,31,41,42]. Conic section models are obtained by cutting a cone with a plane at different angles. In so doing, one may produce conic sections to 2D model different geometric shapes, including spheres, ellipses, hyperbolas, and parabolas, which may turn into 3D models by achieving a revolution about one axis. Such models are quite parsimonious, using only a few parameters to describe the global shape of the cornea [30]. However, Gatinel (2002) showed that this might be insufficient to describe the cornea at a local level, where surface irregularities leading to aberrations may lie [26]. There are no such limitations with polynomial models that rest on an orthogonal basis allowing the model to add or retrieve coefficients in accordance with modeling needs [31,34]. Rational function models can be even more accurate [35]. They are not themselves orthogonal, but they rest on orthogonal models whose coefficients may freely be added or retrieved. Finally, spline models can go even further in terms of accuracy by partitioning the corneal surface into patches to be fitted by so many polynomial models [31,34]. However, by multiplying the number of models across the surface, spline models are not parsimonious. Given the aforementioned drawbacks of conic and spline models, the present study focuses on polynomial and rational function models of the anterior corneal surface. In this work, the focus is on the anterior corneal surface, which is the main responsible for the refractive power of the cornea.

### *2.1.1. Geometric models of corneal shape*

#### *2.1.1.1. Polynomial models of corneal shape*

Several studies rest on the use of polynomials to model the cornea [26,30,32,34,41,43]. They generate corneal surface heights (aka elevations) (see Figure 2.2) that can be generally described as in Equation 2.1:

$$S(u_w, v_w) = h_w = \sum_{g=1}^{G} C_g P_g(u_w, v_w) + \epsilon_w \quad for\ w = 1, 2, \ldots, W \tag{2.1}$$

where the corneal surface $S$ consists of $W$ (polar or spherical) heights $S(u_w, v_w)$ located at (polar or spherical) coordinates $u_w$ and $v_w$ for $w = 1$ to $W$. Each height $S(u_w, v_w)$ (equivalently $h_w$) is modeled as the sum of the product of the $g^{th}$ polynomial $P_g(u_w, v_w)$ and the $g^{th}$ coefficient $C_g$ for $g = 1$ to $G$ to, assuming error $\epsilon_w$. The first coefficient ($C_1$) stands for the mean height of the modeled surface, while the subsequent coefficients ($C_2$ to $C_G$) define its shape [28,29]. The number of polynomial coefficients is given by $G$ in Equation 2.1. However, to facilitate comparisons between polynomial and rational function models, we will refer in the following to the number of shape coefficients $J$, given by $G - 1$.

Polynomial models of the cornea include models that have no orthogonal basis, such as Taylor series [27], and models that do, such as Zernike, Bathia-Wolf and spherical harmonic polynomials. Orthogonal polynomials are more precisely orthonormal, with terms that have the same normalized unit length [27,32,34]. Such models were found to be more effective for corneal shape modeling than nonorthogonal models [31]. Among them, Bathia-Wolf polynomials were as accurate as Zernike polynomials for the same order, but they require twice more coefficients and so are less

[3] Non-standard abbreviations: LM: Levenberg-Marquardt, MFS $\alpha$: Minimum Fully Successful α, P: Polynomial, R: Rational functions, SHP: Spherical Harmonic Polynomials, SHR: Spherical Harmonics Rational functions, Z: Zernike, ZP: Zernike Polynomials, ZR: Zernike Rational functions.

parsimonious [30]. The following will therefore focus on Zernike polynomials and spherical harmonics.

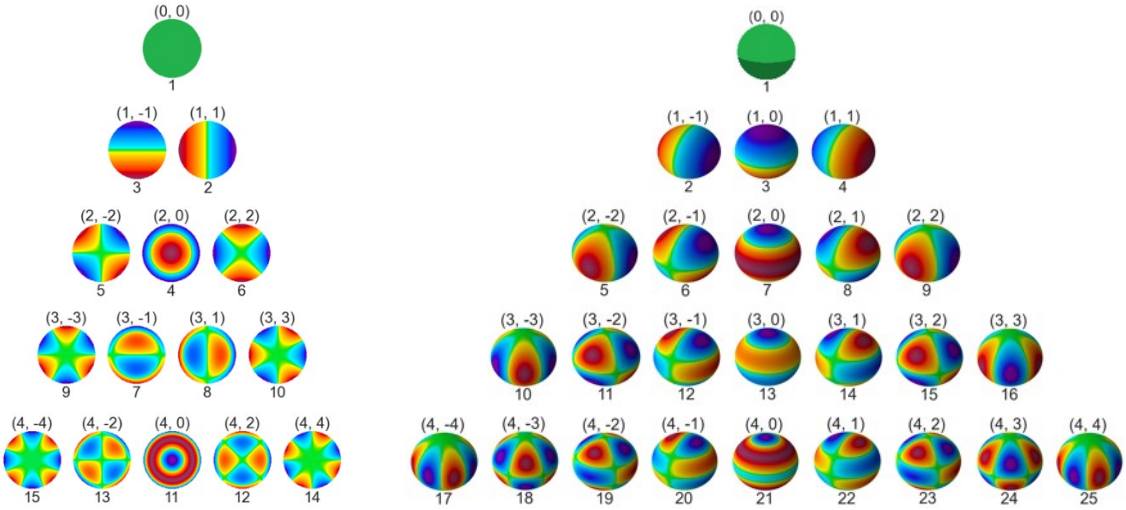


FIGURE 2.1: Pyramids of the Zernike (left) and spherical harmonic (right) basis functions up to order 4. For each Zernike function, *n* and *m* are above each elevation map. For each spherical harmonic function, *l* and *m* are above each elevation map. The sequential shape index of each basis function *j* (or *g* – 1) is given below the elevation map.

*Zernike polynomials.* Different studies have clearly demonstrated the effectiveness of the Zernike polynomial model (ZP) for the description of optical aberrations of the cornea [30,32,35,43]. In ZP modeling, Equation 2.1 becomes Equation 2.2:

$$S(\rho_w, \theta_w) = z_w = \sum_{g=1}^{G} C_g Z_g)\rho_w, \theta_w) + \epsilon_w \quad for \ w = 1, 2, \ldots, W \tag{2.2}$$

Modeled with Zernike polynomials, a corneal surface $S$ consists of a set of $W$ polar heights $S(\rho_w, \theta_w)$ that are located at polar coordinates $\rho_w$ and $\theta_w$ for $w$ = 1 to $W$. Each polar height $S(\rho_w, \theta_w)$ (or $z_w$) is modeled by summing the product of the $g^{th}$ Zernike polynomial $Z_g(\rho_w, \theta_w)$ and the $g^{th}$ coefficient $C_g$ for $g$ = *1* to $G$, assuming error $\epsilon_w$. Each Zernike polynomial $Z_g(\rho_w, \theta_w)$ is defined as in Equation 2.3:

$$Z_g(\rho_w, \theta_w) = \begin{pmatrix} \sqrt{2(n+1)}\, R_n^m(\rho_w)\, cos(m\theta_w)\,, g\ even, m \neq 0 \\ \sqrt{2(n+1)} R_n^m(\rho_w)\ sin(m\theta_w)\,, g\ odd, m \neq 0 \\ \sqrt{n+1}\, R_n^0, m = 0 \end{pmatrix} \tag{2.3}$$

where $n$ is the radial degree (corresponding to a row in Figure 2.1 (left), $m$ is the azimuthal frequency (corresponding to a position in a row), and $g$ is the coefficient index. The radial polynomial $R_n^m(\rho_w)$ is defined as in Equation 2.4:

$$R_n^m(\rho_w) = \sum_{s=0}^{\frac{n-m}{2}} \frac{(-1)^s (n-s)!}{s!\left(\frac{n+m}{2} - s\right)!\left(\frac{n-m}{2} - s\right)!} \rho_w{}^{n-2s} \tag{2.4}$$

In this study, the Noll convention of sequential indices is adopted, in which index $g$ relates to the radial degree $n$ and to the azimuthal frequency $m$ as follows:

$$g = \frac{n(n+1)}{2} + |m| + \begin{Bmatrix} 0, & m > 0 \wedge n \equiv \{0,1\} \, (mod\ 4) \\ 0, & m < 0 \wedge n \equiv \{2,3\} \, (mod\ 4) \\ 1, & m \geq 0 \wedge n \equiv \{2,3\} \, (mod\ 4) \\ 1, & m \leq 0 \wedge n \equiv \{0,1\} \, (mod\ 4) \end{Bmatrix} \tag{2.5}$$

Zernike basis functions display properties of linearity, completeness (fully accounting for any surface over the unit circle domain), orthonormality, and radiality (representing spheroids). As such, they are easily interpretable, are flexible for deciding the optimal number of coefficients needed as a trade-off between parsimony and accuracy, and support the use of exact linear optimization methods.

*Spherical harmonics.* First proposed in 2009 by Iskander et al. to model the cornea spherical harmonic polynomial (SHP) models consist of a complete set of orthonormal periodic functions defined on the surface of a unit sphere [34,44]. Like the Zernike and Bathia-Wolf polynomials, they can be expressed as a sum of circular functions (sines and cosines) as follows:

$$S(\theta_w, \varphi_w) = \rho_w = \sum_{g=1}^{G} C_g \, SH_g(\theta_w, \varphi_w) + \epsilon_w \quad for\ w = 1, 2, \ldots, W \tag{2.6}$$

Modeled with spherical harmonics, the corneal surface $S$ consists of a set of $W$ spherical heights $S(\theta_{fw}, \varphi_w)$ (equivalently $\rho_w$) positioned at spherical coordinates $\theta_w$ and $\varphi_w$. Each spherical height $\rho_w$ is a radius modeled by summing the product of the $g^{th}$ spherical harmonics $SH_g(\theta_w, \varphi_w)$ and coefficient $C_g$ for $g = 1$ to $G$, assuming error $\epsilon_w$. Each spherical harmonics $SH_g(\theta_w, \varphi_w)$ is defined as in Equation 2.7:[4]

$$S^{SH}(\theta_w, \varphi_w) = \begin{pmatrix} \sqrt{2} N_\ell^m \, P_\ell^m(cos\,\theta_w) \, cos(m\varphi_w), & m > 0 \\ \sqrt{2} N_\ell^m \, P_\ell^m(\theta_w) \, sin(m\varphi_w), & m < 0 \\ N_\ell^0 \, P_\ell^0(cos\,\theta_w), & m = 0 \end{pmatrix} \tag{2.7}$$

$N_\ell^m$ is the normalization factor:

$$N_l^m = \sqrt{\frac{(2l+1)}{4\pi} \, \frac{(\ell\text{-m})!}{(l+m)!}} \tag{2.8}$$

and $P_\ell^m$ is the Legendre polynomial:

$$P_\ell^m(x) = \frac{(-1)^m}{2^l \, \ell!} (1 - x^2)^{m/2} \, \frac{d^{\ell+m}}{dx^{\ell+m}} (x^2 - 1)^\ell \tag{2.9}$$

Here, ℓ is the degree (corresponding to a row in Figure 2.1, right), and m is the order (corresponding to a position in a row). The coefficient index g in Equation 2.6 relates to the degree ℓ and the order m as in Equation 2.10, assuming that |m| <= ℓ:

$$g = \ell(\ell + 1) + m \tag{2.10}$$

The corneal surface data must first be centered in relation to a spherical reference called the best-fit sphere (BFS), which is located on the origin of the spherical coordinate system and is normalized to the unit sphere [29]. The spherical information of the modeled surface (center and radius) is contained in the first coefficient ($g$ = 1), while the next coefficients ($g$ = 2 to $G$, or equivalently $j$ = 1 to $J$) represent the relative deformations with respect to this sphere, thus specifying the details of its shape.

Like Zernike polynomials, spherical harmonics display properties of linearity, completeness, and radiality, but they are not as transparently interpretable in terms of optical aberrations. Yet,

[4] The opposite convention where $\theta$ and $\varphi$ are reversed is also possible.

they may provide a better fit to true corneal surfaces than Zernike polynomials for the same radial order and for the same number of coefficients, including surfaces presenting higher-order aberrations [30,34].

#### *2.1.1.2. Rational function models of corneal shape*

A rational function is the ratio of two surfaces produced by polynomial models, as shown in Equation 2.11:

$$S(u_w, v_w) = h_w = \frac{S^N(u_w, v_w)}{S^D(u_w, v_w)} + \epsilon_w \quad for\ w = 1, 2, \ldots, W \tag{2.11}$$

In rational function modeling, the corneal surface $S$ consists of a set of $W$ (polar or spherical) heights $S(u_w, v_w)$ positioned at (polar or spherical) coordinates $u_w$ and $v_w$ for $w$ = 1 to $W$. Each height $S(u_w, v_w)$ (equivalently $h_w$) is modeled as the ratio of a numerator polynomial modeled surface $S^N(u_w, v_w)$ and a denominator polynomial modeled surface $S^D(u_w, v_w)$, assuming error $\epsilon_w$. In the present study, the numerator ($N$) and denominator ($D$) polynomial surfaces can be either Zernike polynomials, in which case they are defined as in Equations 2.2 to 2.5, or spherical harmonics, in which case they are defined as in Equations 2.6 to 2.10. The set of rational ($R$) coefficients $C^R$ is simply the union of the set of numerator coefficients and denominator coefficients:

$$C^R = (\mathrm{C}^{\mathrm{N}}, C^D) = (C_1^N, C_2^N \ldots, C_{G^N}^N, C_1^D, C_2^N \ldots, C_{G^D}^D) \tag{2.12}$$

The number of rational function coefficients $G^R$ is given by:

$$G^R = G^N + G^D \tag{2.13}$$

The number of rational function shape coefficients $J^R$ is accordingly $G^R - 2$.

### *2.1.2. Goal and hypotheses*

Iskander (2009) showed that spherical harmonic polynomial (SHP) models perform better than Zernike polynomial (ZP) models for the same number of coefficients. He observed that SHP models outperformed ZP models on models of orders 4, 8, and 10 and for the same number of coefficients by an average of 22% (Iskander, 2009). This finding, based on nonnegative $m$ spherical harmonic values to insure that the SHP and ZP orders match, was confirmed by Bouazizi et al. (2017) for both negative and nonnegative values [30]. On the other hand, Schneider et al. (2009) showed that the performance of Zernike polynomials can be improved when Zernike coefficients are rearranged to form Zernike rational function models (ZR), in which coefficients are split into numerator and denominator coefficients to be used in rational functions, that is, as the ratio of two Zernike polynomial models [35]. There is no a priori reason why SHP models cannot likewise be integrated into rational function models to form SHR models, thus benefiting from being both a spherical harmonic (SH) model and a rational function (R) model. If so, the SH model advantage should extend to other models than SHP, and the R model advantage to other models than ZR.

While ZP and SHP have been directly compared in the same study design (Iskander, 2009) and likewise for ZP and ZR [35], Zernike (Z) models (ZP and ZR) have never been compared directly to spherical harmonic (SH) models (SHP and SHR). This study aims to simultaneously compare these four models to assess the effectiveness of P versus R models and SH versus Z models both in terms of early accuracy and processing time in a (relatively) low-dimensional space ($J$ < 30).

## 2.2. Method

### *2.2.1. Data collection and conditioning*

This study is based on a dataset of 40 normal anterior corneal topographies selected randomly from a dataset of 8728 topographies acquired from 5060 consenting subjects (4427 female corneas, 4301 male corneas, 4510 OD corneas, 4218 OS corneas). A smaller dataset of 8 keratoconus corneal topographies was also used to test the models on irregular surfaces. The relatively small number of topographies of the dataset was necessary to test rational function models, whose processing time increases rapidly with the number of coefficients. These datasets are drawn from the Database for the anatomopathological, functional and surgical characterization of the cornea (Montreal, QC, Canada) and produced by the Orbscan II corneal topographer (Bausch and Lomb, Rochester, NY).

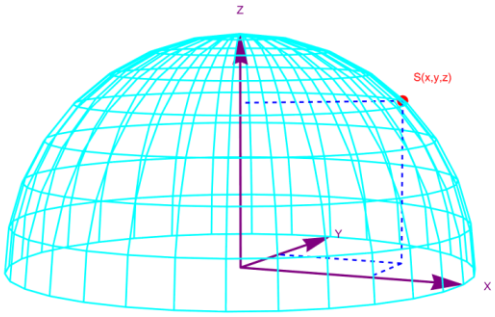


FIGURE 2.2: Schematic representation of the anterior corneal surface *S* in a 101×101 matrix of nasal to temporal elevations *z* at Cartesian positions *x* and *y*. One of these points *S(x,y,z)* is shown with dashed lines.

Each topography came in the form of a 101×101 matrix of elevations (or heights) evenly spaced every 0.1 µm along the horizontal (nasal-temporal) and vertical (superior-inferior) axes (see Figure 2.2). The matrix was first cropped into a 91×91 matrix to eliminate 0.5 mm of radius to clean up the noisiest part of the image fringe due to the lids, lashes, nose, etc. The remaining elevations were linearized into a *Z* vector of 8281 elevations, which was assigned *X* and *Y* vectors of the same length to form a three-column matrix of Cartesian coordinates *x, y* and *z* representing the dots *S(x,y,z)* of the corneal surface *S*.

In preparation for model optimization, each set of Cartesian coordinates was generated by uniform scaling steps insuring normalization and converted into polar coordinates for Zernike polynomials:

$$(x_w, y_w, z_w) \rightarrow (\rho_w, \theta_w, z_w) \tag{2.14}$$

and into spherical coordinates for spherical harmonics:

$$(x_w, y_w, z_w) \rightarrow (\rho_w, \theta_w, \varphi_w) \tag{2.15}$$

To estimate the repeatability error of the topographer, we collected another dataset from the same database for which double acquisitions of corneal measures were made. This measure was estimated to set an accuracy threshold when estimating the minimum best numbers of coefficients. This dataset contained two different acquisitions for 257 corneas, including 120 of them from right eyes and 137 from left eyes, and the RMSE repeatability score was computed for each of them and estimated as 6.18 µm for a 91×91 matrix of elevations.

### *2.2.2. Model optimization*

*Polynomial models.* These models were fitted with least squares, a method that offers an exact solution quasi-instantly provided that the pseudo-inverse of the surface matrix exists, as is the case here.

*Rational function models.* The optimization of rational functions was based on Levenberg-Marquardt (LM), an iterative method recommended by [35] and found here to be the most effective among those available in the SciPy library [36] for the task at hand. LM is a derivative method that takes advantage of the gradient descent technique to solve non-linear least-squares problems and that relies on the MINPACK library to implement gradient descent [37]. It is more robust than other algorithms such as Gauss-Newton and applies to unconstrained problems. The LM algorithm rests on the following approximation:

$$\mathrm{H}(\mathrm{C} + \Delta_{\mathrm{C}}) \approx \mathrm{H}(\mathrm{C}) + \mathfrak{J}(\mathrm{C})\Delta_{\mathrm{C}} \tag{2.16}$$

$C$ is a tested set of coefficients and $H(C)$ is given by

$$h_w = S(u_w, v_w) \quad \textit{for } w = 1, 2, \ldots, W, \textit{ given } C \tag{2.17}$$

$S(u_w, v_w)$ was defined in Equation 2.11. The Jacobian matrix $\mathfrak{J}(\mathrm{C})$ is given by:

$$\mathfrak{J}(C) = \frac{\partial H(C)}{\partial C}\begin{pmatrix} \frac{\partial}{\partial c_1}h_1(C) & \frac{\partial}{\partial c_2}h_1(C) & \cdots & \frac{\partial}{\partial c_{(N+D)}}h_1(C) \\ \frac{\partial}{\partial c_2}h_2(C) & \frac{\partial}{\partial c_2}h_2(C) & \cdots & \frac{\partial}{\partial c_{(N+D)}}h_2(C) \\ \vdots & & \ddots & \vdots \\ \frac{\partial}{\partial c_1}h_W(C) & \frac{\partial}{\partial c_2}h_W(C) & \cdots & \frac{\partial}{\partial c_{(N+D)}}h_W(C) \end{pmatrix} \tag{2.18}$$

Finally, $\Delta_C$ is defined as:

$$\Delta_C = (\mathfrak{J}(C)^T\, \mathfrak{J}(C) + \lambda I)^{-1}\; \mathfrak{J}(C)^T\, (T - H(C)) \tag{2.19}$$

The optimal set of coefficients $\hat{C}$ is estimated in accordance with the following algorithm (in which Equation 2.19 is applied recursively):

*1:* $\hat{C} \leftarrow C^{(0)}$ (2.20)
*2:* $\Delta_C \leftarrow x$ *with* $x > \Delta_{min}$
*3:* ***while*** $|\hat{C} - T| > \epsilon_{tol}$ ***and*** $\Delta_C > \Delta_{min}$ ***do***
*4:* $\Delta_C \leftarrow (\mathfrak{J}(C)^T\, \mathfrak{J}(C) + \lambda I)^{-1}\; \mathfrak{J}(C)^T\, (T - H(C))$
*5:* $\hat{C} \leftarrow C + \Delta_C$
*6:* ***end while***

To ensure that the LM algorithm finds the global minimum, Schneider et al. (2009) recommends that the initial set of denominator coefficients $C^{D(0)}$ be set to $(1, 0, 0, \ldots, 0)^{\mathrm{T}}$ to allow the least-square estimator (Moore-Penrose) pseudoinverse to apply properly. We tested that LM is even more robust if the initial set of numerator coefficients $C^{N(0)}$is itself preoptimized with ordinary least squares to make it closer to the final solution.

### *2.2.3. Model evaluation*

The effectiveness for dimensionality reduction of the four geometric models under study was evaluated as to their accuracy and processing time on relatively small numbers of shape coefficients (*J* values) that were deemed to be potentially optimal for machine learning (ML) tasks. Only sets

of shape coefficients are considered in the subsequent analyses. At least one numerator coefficient and one denominator shape coefficient must be present in each set of rational coefficients.

Concerning the evaluation of modeling accuracy, the range of potentially best *J* values, or best *J* range, was specified by applying the elbow method (frequently used in cluster analysis) to the RMSE by the *J* curve of each model (see Figure 2.3). Each score of an RMSE curve measured the distance (root mean square error) between the modeled surfaces produced by a geometric model for a given *J* value and the corresponding raw topographic true surfaces (the missing dots resulting from the topographic acquisition flaws were excluded from the computation). For the RMSE curve of each model, the best *J* range was delimited by the minimum and maximum values of its elbow. The elbow of an RMSE curve starts where the bulk of the curve convergence toward the minimum error is achieved, and it ends where the curve starts to flatten (so that only little gain of accuracy can be made by further increasing the *J* value). Once the best *J* range has thus been delimited for each model, a common best *J* range was established as their best overlap to allow the models to be compared on their accuracy in a common low-dimensional space of optimization for ML tasks. Complementary to RMSE scores, performance profiles were further made to evaluate the proportion of corneal surfaces whose RMSE scores were better than a given value α [14] (see Figure 2.4).

In addition to this quantitative evaluation, a visual assessment of the models' accuracy was made by comparing a series of elevation maps of the same corneal surface as reconstructed by the four geometric models on different *J* values (see Figure 2.5). Assuming that a corneal surface is approximately spherical,an elevation map shows the differences in height between a corneal surface and the sphere that fits it the best (the best-fit sphere, or BFS) at every position of the surface based on a gradient of colors (colormap). The BFS is computed by least square fitting to the corneal surface. Warm colors represent positive differences (surface regions outside the BFS), and cold colors represent negative differences (surface regions inside the BFS) [3,15,38].

The processing speed of the geometric models was estimated by measuring the average time they took to process a cornea (the time needed to process the whole dataset divided by its size) with the same predefined computer configuration for different *J* values (2, 5, 8, 11, 14, 17, 20, 23, 26 and 29). The computer cluster used for this test was Narval [45], managed by Digital Research Alliance of Canada, and configured with 32 CPUs per task and 10 G of memory per CPU.

## 2.3. Results

### *2.3.1. Normal corneas*

*RMSE curves.* An RMSE curve larger than the best *J* range for normal corneas is presented (from $J = 4$ to 26) in Figure 2.3 (left) to locate its minimum and maximum *J* values. As can be seen, the bulk of the convergence is achieved somewhere between $J = 6$ and 12, depending on the model. Additionally, all the curves start to flatten around $J = 24$. Therefore, the (common) best *J* range of RMSE curves was set from $J = 12$ to 24, as shown in Figure 2.3 (right). As can be seen, for $J \geq 12$, all curves have RMSE scores lower than the mean repeatability error of the topographer (6.2 µm). On average, the spherical harmonic (SH) models (SHP and SHR) are more accurate than the Zernike (Z) models (ZP and ZR), while the rational function (R) models (SHR and ZR) are somewhat more accurate than the corresponding polynomial (P) models (SHP and ZP, respectively). Therefore, being both an SH model and an R model is favorable for early convergence. However, the most effective factor between SH and R is SH, as revealed by the gaps between the SH and Z curves, which are more than three times larger than those between the P and R curves (27.8% improvement with SH vs. 8.1% with R).

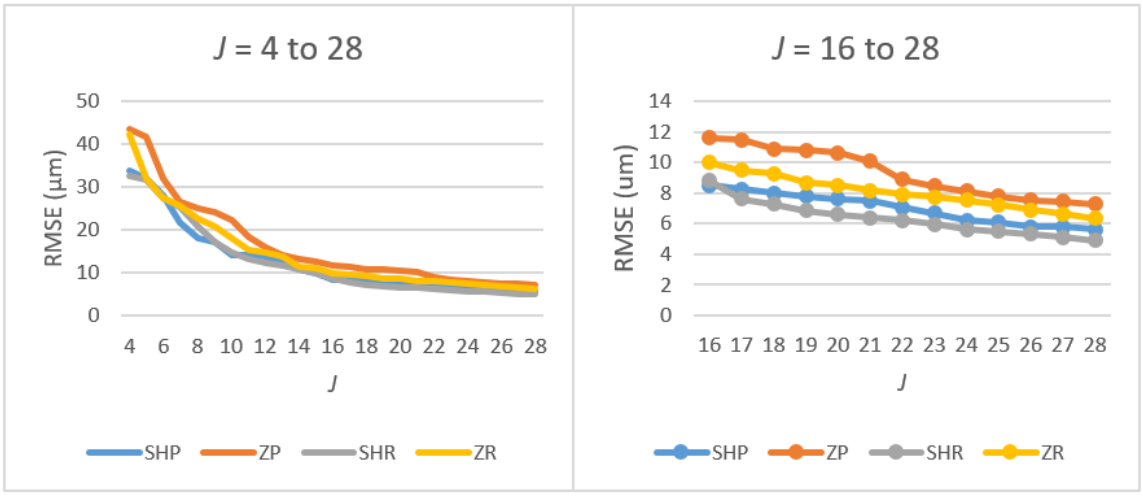


FIGURE 2.3: Accuracy of polynomial and rational function models (SHP, ZP, SHR, ZR) from $J = 4$ to 26 with normal corneas (left). Zoomed-in view of the best $J$ range ($J$ = 12 to 24) (right).

*Performance profiles.* Figure 2.4 presents the performance profiles of the examined models for normal corneas with $J = 16$. Except for ZP with $J = 12$, all models achieve full success (100% of the data are below the success standard $\alpha$) when $\alpha$ is below the topographer repeatability error of 6.2 µm. Their full success arises roughly in the same order as with RMSE curves: SHP and SHR followed by ZR and ZP.

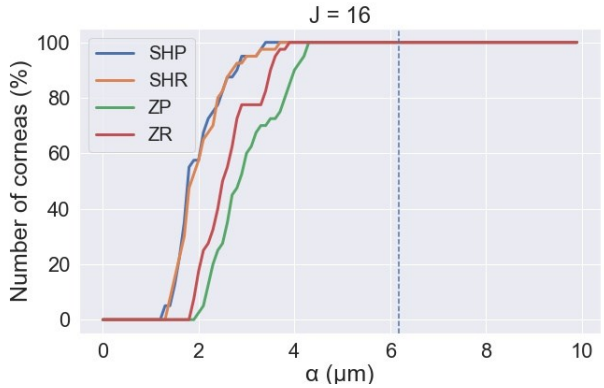


FIGURE 2.4: Typical performance profile of SHP, ZP, SHR and ZR for $J = 16$ with normal corneas. The dashed blue vertical line represents the topographer repeatability error.

TABLE 2.1: MFS $\alpha$ with normal corneas in the best $J$ range for $J$ = 12, 14, 16, 18, 20, 22 and 24 (in µm). All MFS $\alpha$ values are below the repeatability error of 6.2 µm.

| $J$ | SHP | SHR | ZP | ZR |
|---|---|---|---|---|
| 12 | 4.9 | 4.8 | 6.5 | 5.6 |
| 14 | 4.4 | 4.3 | 6.0 | 5.0 |
| 16 | 3.4 | 3.7 | 4.3 | 3.9 |
| 18 | 3.3 | 2.9 | 4.1 | 3.5 |
| 20 | 3.2 | 2.8 | 4.0 | 3.4 |
| 22 | 2.8 | 2.4 | 3.5 | 3.3 |
| 24 | 2.6 | 2.3 | 3.5 | 3.2 |
| Mean MFS $\alpha$ | 3.5 | 3.3 | 4.6 | 4.0 |

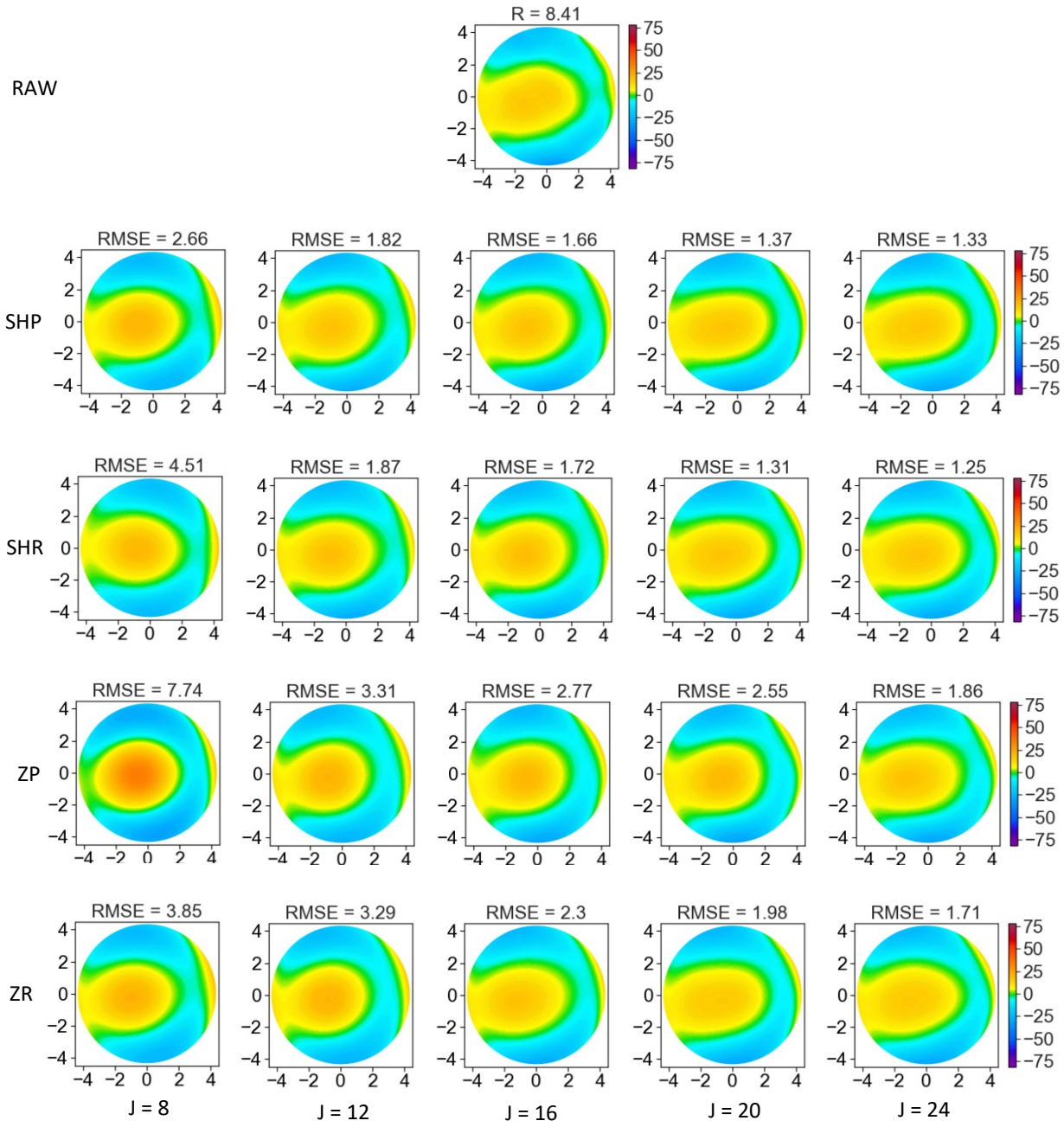


FIGURE 2.5: Elevation maps of the same OD normal corneal surface presented in raw version (first row) or modeled with ZP (second row), ZR (third row), SHP (fourth row) and SHR (fifth row) for $J$ = 8, 16, 20 and 24. The last three $J$ values are in the best $J$ range.

Table 2.1 presents the minimum fully successful (MFS) $\alpha$ value across the best $J$ range, that is, the minimum value of $\alpha$ at which a model achieves full success for a given $J$. These performance profiles are consistent with the RMSE curves of Figure 2.3. On average, SH models have a lower MFS $\alpha$ than Z models (3.4 vs. 4.3 µm), and R models have a lower MFS $\alpha$ than P models (3.7 vs. 4.0 µm). The SH advantage (20.1% improvement) is more important than the R advantage (9.6%). The best model for early convergence is SHR.

*Elevation maps*. Figure 2.5 presents the elevation map of a true normal cornea and those of the same surface modeled by SHP, SHR, ZP and ZR with $J$ = 8, 16, 20 and 24 (the last three $J$ values

are in the best $J$ range). As expected, for each of these models, the shape of the modeled surface becomes progressively closer to that of the true surface as $J$ increases, especially when they $J$ gets into the best $J$ range, as revealed by RMSE scores and by the patterns of colors displayed by the elevation maps.

### *2.3.2. Keratoconus corneas*

Figure 2.6 presents the curves of the four models from $J = 4$ to 28 for keratoconus corneas. It can be seen that the best $J$ range lies somewhere between $J = 14$ and 26 (a shift toward larger $J$ values compared to normal corneas). Within that range, the RMSE scores of all models reach the topographer repeatability error of 6.2 µm at around $J = 24$.

SHR is the most accurate model for keratoconus corneas, followed by SHP, ZR and ZP. On average, SH models are more accurate than Z models, and R models more than P models. Again, the fact of being both an SH model and an R model favors the aptitude of a model for early convergence. The most important factor of accuracy between SH and R in modeling keratoconus corneas is again SH (21.6% from SH to Z models vs. 10.9% from R to P models).

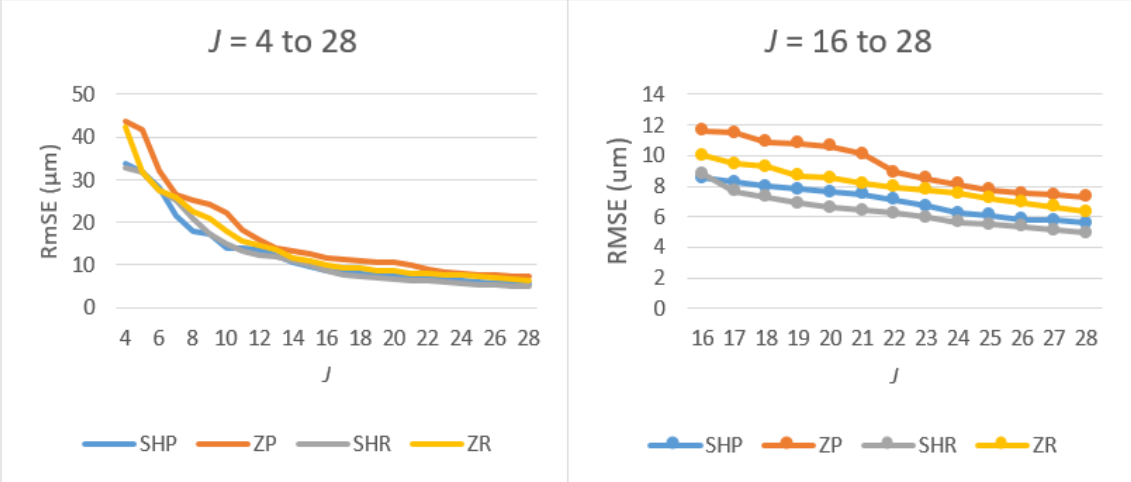


FIGURE 2.6: Accuracy of polynomial and rational function models (SHP, ZP, SHR, ZR) from $J = 4$ to 28 with keratoconus corneas (left). Zoomed-in view of the best $J$ range ($J = 14$ to 26) (right).

*Performance profiles.* As shown in Table 2.1, all models reach the topographer repeatability error of 6.2 µm around $J \geq 24$, reaching it in the following order: 1st SHR, 2nd SHP and ZR, and 3rd ZP (when reached, the RMSE is boldfaced). Again, on average, SH models outperform Z models (MFS $\alpha$ of 7.15 vs. 9.15 µm), and R models outperform P models (7.3 vs. 8.95 µm). And again, the SH advantage (21.9%) is greater than the R advantage (17.9%).

Table 2.2: MFS $\alpha$ with keratoconus corneas in the best $J$ range ($J = 14$, 16, 18, 20, 22, 24 and 26, in µm; the MFS $\alpha$ is boldfaced when the repeatability error of 6.2 µm is reached).

| $J$ | SHP | SHR | ZP | ZR |
|---|---|---|---|---|
| 16 | 7.6 | 13.2 | 13.2 | 9.4 |
| 18 | 7.5 | **6.2** | 12.9 | 8.4 |
| 20 | 7.0 | 5.6 | 12.8 | 7.0 |
| 22 | **5.8** | 4.6 | 7.2 | **5.9** |
| 24 | 4.4 | 2.8 | **6.2** | 5.5 |
| 26 | 4.2 | 2.4 | 5.2 | 4.5 |
| 28 | 4.1 | 2.1 | 5.1 | 4.1 |
| Mean MFS $\alpha$ | 5.8 | 5.3 | 8.9 | 6.4 |

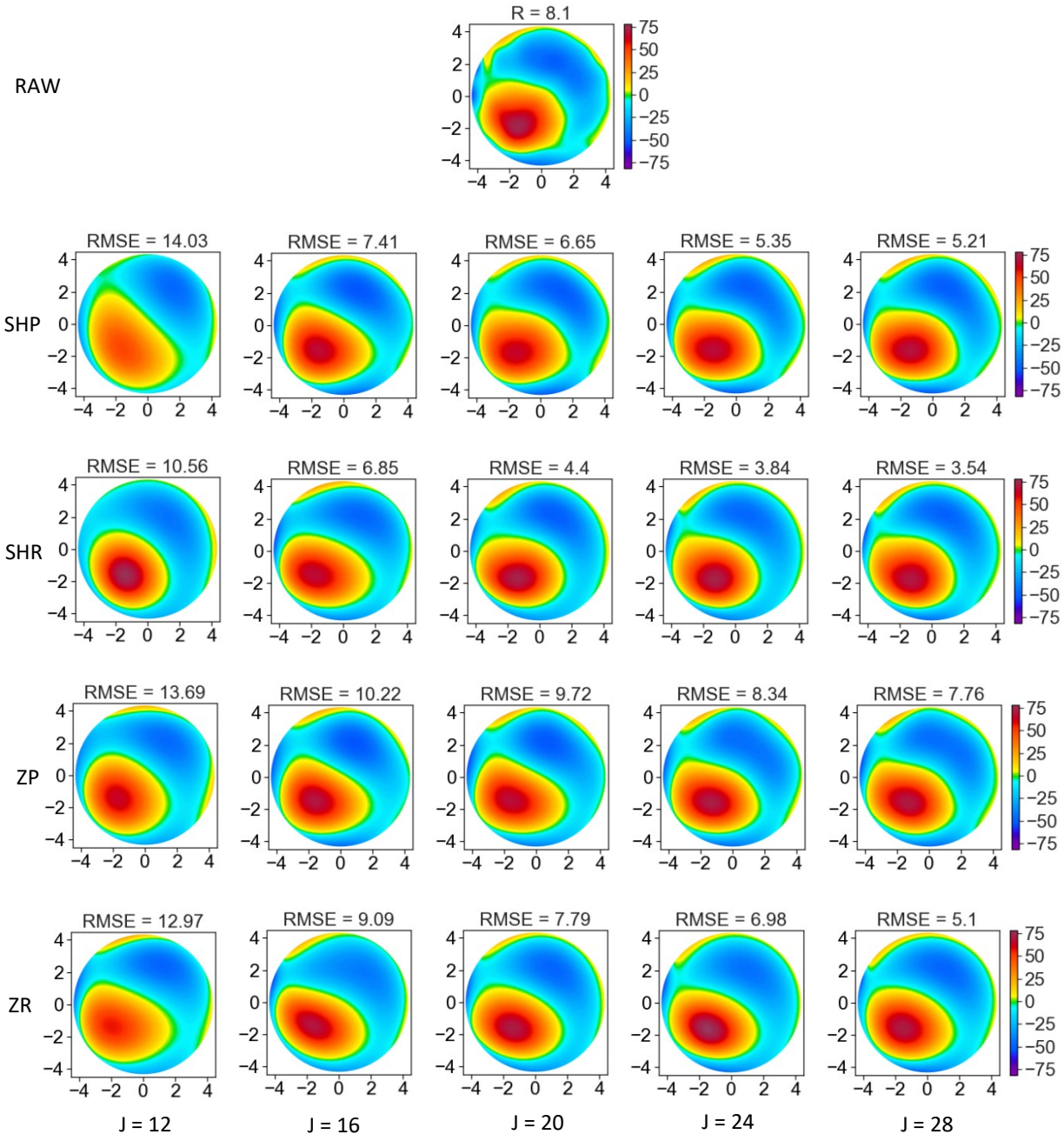


FIGURE 2.7: Elevation maps of the same keratoconus corneal surface presented in raw version (first row) or modeled with SHP (second row), SHR (third row), ZP (fourth row) and ZR (fifth row) for $J$ = 8, 16, 20 and 24. The last three $J$ values are in the best $J$ range.

### *2.3.3. Processing times*

As shown in Figure 2.8 (left), R models take increasingly more time to process the anterior surface of a cornea than P models as *J* gets larger, especially for SHR. P models have a processing time that remains within the order of a half second even at $J = 29$. Meanwhile, ZR takes 550 s. to process a cornea at $J = 17$ and 3642 s. at $J = 29$. As for SHR, the increase is even more dramatic: it takes 4677 s. and 37220 s., respectively. Inverse transformations show that while P models are processed in quasi-linear time, R models are processed in $O(x^4)$.

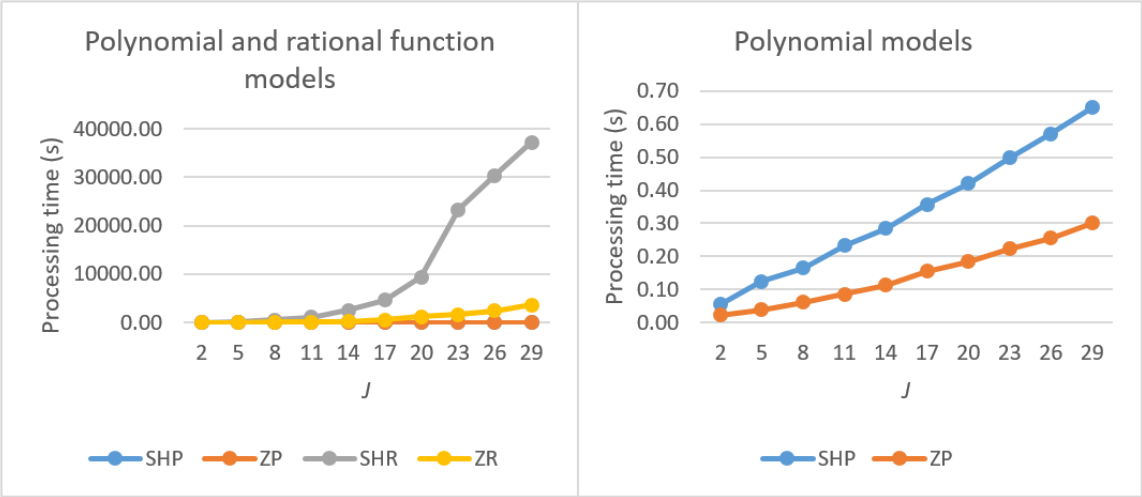


FIGURE 2.8: Curve of the processing time needed for SHP, ZP, SHR and ZR to process the anterior surface of a cornea according to *J*.

## 2.4. Discussion

In this study, we examined the effectiveness of a few geometric models at reducing the dimensionality of a dataset of corneal surfaces from about 10000 dimensions to a few only, and in so doing their aptitude to process large datasets of corneal surfaces. To this end, the models had to be parsimonious, being capable of achieving early convergence, and fast enough to process large datasets in a reasonable time. Eliminating from the start different types of geometric models deemed to be unsuitable for this task (conic section models, spline models, non-orthogonal polynomials, etc.), two polynomial models (SHP and ZP) and two corresponding rational function models (SHR and ZR) were examined. To insure low dimensionality, their performance at modeling normal and keratoconus corneas was assessed for relatively small numbers of coefficients. It was first determined, based on the elbow method, that the most promising *J* numbers ranged somewhere between $J = 12$ and $J = 24$ for normal corneas, and between $J = 14$ and $J = 26$ for keratoconus corneas (an increase due the additional difficulty of fitting their more irregular shape).

We already knew that both SHP and ZR were more accurate than ZP, especially for irregular surfaces [34,35]. But we did not know whether SHP was superior to ZR, and whether their superiority over ZP models could extend to other types of SH model (such as SHR) and R models (again, such as SHR). Within the best *J* range, for both normal and keratoconus anterior corneal surfaces, this was indeed the case. SH models were more accurate than Z models, and R models more than P models. Finally, the SH advantage was more important than the R advantage. When considering processing times, though, the situation was reversed: P models performed much better than R models (in very flat quasi-linear time vs. polynomial time), and Z models performed slightly

better than SH models (increasingly so in their R versions). This made the processing of R models for large databases increasingly impracticable as $J$ grew larger, especially for SHR.

Given this state of affairs, when one wants to achieve dimensionality reduction by geometric modeling, if speed is the main consideration and only normal corneas need to be processed (as can be the case in exploratory studies or in early development phases of ML projects), then ZP is the best choice. Given its transparent interpretability (each Zernike coefficient is assigned a corneal parameter correlate), it remains an excellent choice for clustering tasks where the clear interpretation of clusters might be an issue, especially for tasks involving normal corneas.

If instead accuracy is the main consideration, then SHR is the best choice, especially for irregular corneas, provided that powerful processing resources are available and that the optimization procedure is alleviated to reduce the processing time. This can be done by reducing the optimization space of SHR before applying it to a large dataset. To this end, one can narrow down the best $J$ range (in pretests) for the type of task to be conducted (for example, one may process SHR for only $J = 16$ to 18 instead of $J = 12$ to 24). One can also considerably simplify and speed up the optimization process by imposing the same set of rational coefficients to all surfaces (the one found to be on average the best for all surfaces in pretests). For keratoconus corneas at least, the results remain better in the best $J$ range using SHR with the same set of coefficients for each surface (for $J = 24$, RMSE = 5.82 μm) than for SHP (RMSE = 6.46 μm), though indeed not as good as for SHR with the best coefficient set for each surface (RMSE = 5.64 μm).[5]

On the other hand, if one looks for the best compromise between accuracy and speed, then SHP is clearly the best choice of geometric model for dimensionality reduction of corneal datasets, being both nearly as accurate as SHR and almost as fast as ZR.

## 2.5. Conclusion

This study has investigated how geometric modeling can be used for dimensionality reduction in different applications. SHP is the best compromise between accuracy and speed, but ZP remains an interesting option for testing and project development, and SHR is also interesting if accuracy is the priority, especially for irregular surfaces. However, in the case of SHR, the corneal processing time must be substantially reduced. A major processing cost of SHR in the present study was the need to determine the best combinations of numerator and denominator coefficients (the grid search procedure used involved running the model for each of the $J - 1$ possible combinations). The issue to be investigated in a next study with regard to SHR, then, is to what extent the best combinations identified with a small dataset can apply to a large dataset with a minimum of accuracy loss (generalizability issue). Another issue is to what extent the best combinations can be learned effectively in applications involving training. Besides, geometric modeling (GM) is not the only way to reduce the dimensionality of a dataset. Feature extraction (FE) methods (PCA, LDA, t-SNE, etc.) can also be used to this end. It remains to see whether linear or nonlinear FE methods should be used alone or in combination with GM methods for a given task, and how.

## Acknowledgements

This work was supported by the QVRN (Quebec Vision Research Network), the FRQNT (Fonds de recherche du Québec Nature et Technologie) and the MUTAN (University Mission of Tunisia in North America).

[5] Using the same set of coefficients would simplify considerably the learning process in applications involving training. Otherwise, the trained model would need to learn the best proportion of numerator and denominator coefficients for a given $J$ in addition to the coefficients.

# CHAPTER 3: THE EFFECTS OF CLINICAL VARIABLES ON THE NORMAL CORNEAL SHAPE VISUALIZED WITH AVERAGE ELEVATION MAPS

Hala Bouazizi[1], Isabelle Brunette[2,3], Jean Meunier [1,2]

1 Department of Computer Science and Operations Research, University of Montreal, Montreal, Quebec, Canada
2 Department of Ophthalmology, University of Montreal, Montreal, Quebec, Canada
3 Maisonneuve-Rosemont Hospital Research Center, Montreal, Quebec, Canada

## Abstract

The cornea is prone to significant changes in its 3D shape in the normal population. Factors of variability include geometric parameters (white-to-white distance, anterior chamber depth), refraction parameters (sphere, cylinder, axis), and demographic parameters (age, gender), among others. While the statistical foundations of this research are increasing, there is a need to visualize the effects of these factors on the corneal shape. Corneal shape analysis took a step forward when corneal topographic maps were developed to visualize the typical characteristics of groups of corneal surfaces instead of focusing on the idiosyncrasies of one single surface at a time. Thanks to these group maps, it is now possible to visualize globally how corneal shape is affected by clinical factors, regardless of individual variability. This has already been done for a few factors, but only as a proof of concept. The present study presents a systematic atlas of group maps (average elevation maps) of normal adult anterior corneal surfaces that covers the shape transformations produced by different clinical variables (mentioned above). Its construction involved a preprocessing step in which the dimensionality of the dataset is reduced by geometric modeling with Zernike polynomials. The corneal shape data were then grouped in accordance with the clinical variables. A centroid surface was constructed for each group of surfaces by averaging their modeling coefficients, which was represented in the form of an elevation map. The clinical effects made visible in the atlas of average elevation maps thus constructed were consistent with the literature on the corneal shape. The possible uses of such an atlas are discussed.

**Keywords:** cornea, Zernike polynomials, atlas, corneal topography, elevation maps

## 3.1. Introduction[6]

Shape characterization of the normal cornea is of paramount importance to better understand visual acuity and improve diagnostic and therapeutic assessments. Several factors influence corneal shape, including geometric parameters (axial length, anterior chamber depth, white-to-white distance, etc.), refraction parameters (axis, cylinder, spherical equivalence, etc.) and demographic parameters (age, sex, race, ethnicity, etc.) [11]. In this work, the focus is on the anterior corneal surface, which is the main responsible for the refractive power of the cornea.

Corneal shape analysis took a step forward when group topographic maps were developed to visually capture the typical characteristics of groups of corneal surfaces in single maps instead of focusing on the idiosyncrasies of one single surface at a time. In 1994, Hayashi et al. were the first to develop such maps, including average maps, standard deviation maps, count maps, and average difference maps [46]. This toolkit of group maps was further improved over time by providing t-test maps [47], average and standard deviation maps applied to pachymetry (instead of elevations) [48], diagnosis maps (involving an individual map in reference to a corresponding group map) [38], and by improving the accuracy of group maps through different topography alignment algorithms [38,43]. Such group maps have been used to visualize and compare the characteristics of different clinical groups of corneal shapes, including age [38], gender [29,30], spherical equivalent [30], and diagnosis (e.g., keratoconus vs. normal corneas) [38], but not to assess the validity of the dataset of corneas itself, as required in machine learning (ML) tasks.

The goal of this study is to develop and validate an atlas of average elevation maps to visualize the transformations produced by varying clinical variables known to have an effect on the shape of the anterior surface of normal corneas. Such a visualization tool of corneal shape transformations can be instrumental not only for clinical and pedagogic purposes but also as a validation and interpretation tool to assess the datasets used and produced in machine learning research.

The atlas average elevation maps is based on a dataset of normal adult anterior corneal surfaces modeled with a moderate number of Zernike polynomials to obtain a low-dimensional dataset that is good enough to model normal corneas in many applications. The modeled surfaces of the dataset are grouped in accordance with different clinical parameters known to have a determining effect on the anterior surface of the normal cornea, including geometric parameters, refraction variables and demographic variables. The atlas of average elevation maps thus formed is then assessed in light of the clinical literature.

### *3.1.1. Geometric parameters*

The BFS R, WTW, ACD and Side are direct measures of different aspects of the corneal shape.

*BFS R.* The *best-fit sphere* (BFS) is the sphere that best fits the shape of the cornea under examination. It is specified as a radius (in mm) and a center (Cartesian coordinates). The radius of the BFS (BFS R) is positively related to the degree of corneal curvature of the horizontal meridian (CHM) and to the vertical meridian (CVM) at the apex [3,14].

*WTW.* The white-to-white distance (WTW), also known as horizontal corneal diameter (HCD) or visible iris diameter (HViD), measures the limbus-to-limbus distance of the cornea. It is known to correlate positively with the radius of curvature, the axial length and the spherical equivalent and negatively with the degree of corneal curvature [7].

*ACD.* The *anterior chamber depth* (ACD) is the distance from the central anterior corneal epithelium to the anterior crystalline lens capsule. It is negatively related to K, the degree of central curvature (keratometry) [8] and to the spherical equivalent (SE) (by which myopia is distinguished from hyperopia) [9,13].

[6] Non-standard abbreviations: CHM (Curvature of the Horizontal Meridian) and CVM (Curvature of the Vertical Meridian).

*Side.* The *side* of the cornea differentiates between right eye (OD) and left eye (OS) corneas. Side is associated with an interocular horizontal symmetry between OD and OS corneas (enantiomorphism) [10,11]. This symmetry is not affected by the age, gender or spherical equivalent when the dataset is balanced (involving an acquisition for the two eyes of each participant). Within each eye, an intraocular corneal asymmetry of asphericity is also observed between the temporal side and the nasal side of the corneas, with more flattening nasally than temporally [10].

### *3.1.2. Refraction parameters*

*Refraction* is the process, achieved mainly by the cornea, by which the light is bent to produce a focused light beam on the retina. An *optical aberration* is a lack of refractive power caused by a failure of light rays to converge on the retina and to set the point of focus on it (defocus). *Low-order aberrations* are the most common types of optical aberrations, and people with normal corneas may experience them to varying degrees (85 percent of all aberrations in an eye). They include *ametropia*, which arises when the vision is out of focus (too short or too long), and *astigmatism*, which occurs when the cornea is not spherical enough. Contrasted with emmetropia (the eye is in focus), *ametropia* can take the form of myopia (the focus is too short) or hyperopia (the focus is too long). The degree of ametropia is measured in diopters in terms of *spherical equivalent* (SE), calculated by adding the sphere power with half of the cylinder. The SE is negative for myopia and positive for hyperopia. *Astigmatism* is measured in terms of the cylinder and the axis. The *cylinder* specifies the degree of astigmatism of the eye by stating how flat or spherical it is. The *axis*, measured in degrees from 0° to 180°, gives the orientation of the astigmatism by specifying the angle of the main axis of the corneal deformation (the degree of corneal rotation). The following relationships have been established between refraction parameters and corneal shape.

*Ametropia.* An increase in spherical equivalent (SE) from myopia to hyperopia is associated with a flatter curvature of the central area of the cornea [12,49], a reduction in eccentricity [50], and a shallower anterior chamber depth (ACD) [9,13], and with a larger WTW (as mentioned earlier).

*Astigmatism.* "With the rule" (WTR) astigmatism occurs when the axis of the cornea is roughly horizontal (the axis angle between 0° and 30° or between 150° and 180°). This is the case when the curvature of the vertical meridian is the steepest and the curvature of the horizontal meridian (CHM) is the flattest [15,17]. "Against the rule" (ATR) astigmatism arises when the axis is roughly vertical (the axis angle is between 60° and 120°). The CHM is then the steepest and the CVM the flattest. Otherwise, astigmatism is oblique (the axis angle is between 30° and 60° or between 120° and 150°).

### *3.1.3. Demographic parameters*

*Age.* This demographic factor has been related to a variety of changes in the shape of the anterior corneal surface. The most often quoted one is a shift from a "with the rule" to "against the rule" astigmatism, which involves an increase in the curvature of the horizontal meridian (CHM) and a decrease in the curvature of the vertical meridian (CVM) [16]. A decrease in white-to-white distance (WTW) was also observed for elderly people [11]. Age is further associated with a reduction in the anterior chamber depth (ACD) [8,13,20,21]. Concerning refraction, the prevalence of myopia is generally lower in older adults than in young adults [22]. For hyperopia, its prevalence starts to increase at approximately 35-40 years old until 65 years old [23]. Together, these two refraction effects produce an overall increase in SE (with a possible slight reduction at approximately 70 yo) [23].

*Gender*. Males have generally a wider white-to-white distance (WTW) than females [7,11,19], known to correlate with the BFS R [3,14]. On the other hand, females have a steeper curvature of

horizontal and vertical meridian (CHM) [11,14,19] and a shallower anterior chamber depth (ACD) [8,20,24]. Also, in adulthood, females have a higher prevalence of myopia than males and a lower prevalence of hyperopia, and thus a lower SE [25].

## 3.2. Method

### *3.2.1. Clinical database and topographies*

The database used in this study comprises a total of 8609 topographies of normal adult anterior corneal surfaces (4245 female corneas and 4364 male corneas, 4438 OD corneas and 4171 OS corneas) acquired from 4941 consenting subjects. These topographies, collected with the Orbscan II topographer (Bausch & Lomb, Rochester, NY), are part of the Database for the anatomopathological, functional and surgical characterization of the cornea [5], which compiles more than 36,000 corneal topographies. This database was screened to ensure that subjects had no history of ocular disease, ocular surgery, or recent contact lens wear. No topographies were recorded more than once for the same eye. Each topography is accompanied by information on geometric parameters on the cornea (white-to-white diameter, anterior chamber depth, eye side), refraction parameters (sphere, cylinder, axis), and demographic information (gender, age). This clinical information is followed by topographic information describing each corneal surface in the form of a string of 10201 points representing the 101×101 elevations of the corneal surface topography evenly spaced (every 0.1 mm) along the *X* (left-right) and *Y* (up-down) axes. The grid of elevation points was reduced into 91×91 matrices to eliminate 0.5 mm of radius and clean up the noisiest part of the image fringe (periphery) due to the lids, lashes, nose, etc. Involving human subjects, the experimental procedures described in this paper were approved by the Institutional Review Board.

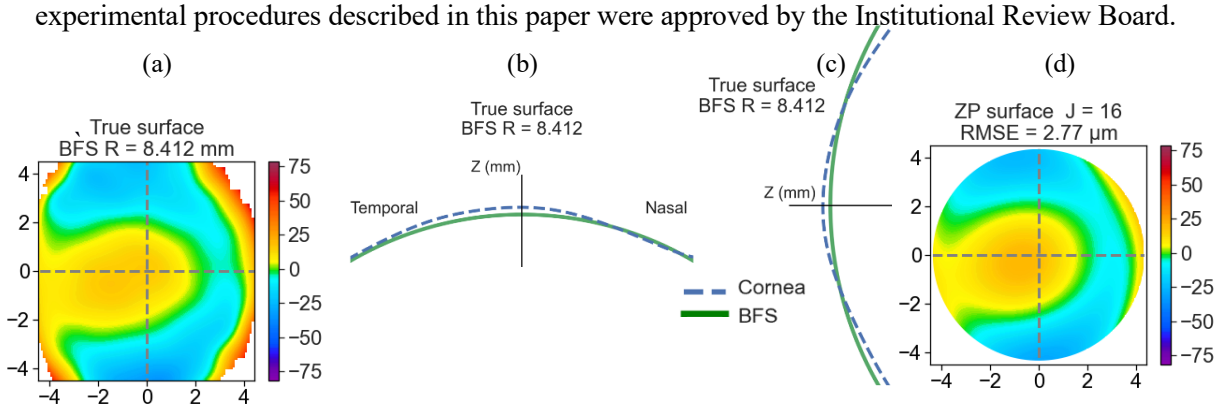


FIGURE 3.1: (a) Elevation map of a true OD anterior corneal surface, (b) Horizontal and (c) vertical profile cuts of the same true surface in relation to the BFS (in green) (d) Elevation map of the same surface modeled with 16 Zernike coefficients (a fringe is radially removed to eliminate the most noisy part of the map). Elevation maps and profile cuts are all in reference to the BFS of the surface. The location of the horizontal and vertical profile cuts on elevation maps is indicated by dotted lines. The differences of elevation with the BFS in the profile cuts are amplified 10 times for better visualization.

In an elevation map, the elevations of the corneal surfaces are presented in reference to a best-fit sphere (BFS): their differences at each point of the grid are visualized with a gradient of colors in which warm colors are for positive differences (outside the BFS), cold colors for negative differences (inside the BFS), and green colors for no significant differences. Figure 3.1 (a) presents an elevation map of a true OD anterior corneal surface along with the radius of the best-fit sphere (BFS R). Horizontal and vertical profile cuts of the true surface are presented in Figure 3.1 (b) and (c). These profile cuts correspond to the dotted lines in Figure 3.1 (a). A map of the same surface modeled with $J = 24$ Zernike terms is finally presented in Figure 3.1 (d), in which the most noisy fringe is radially removed (error score (RMSE) of 1.86 µm).

### *3.2.2. Dimensionality reduction*

In the reference dataset, dimensionality reduction was achieved by geometric modeling using $J$ = 16 shape Zernike polynomials, where 16 was found in pretests to be in the range of optimal values for a variety of applications (predictions, clustering, etc.). In Zernike modeling, the corneal surface is modeled as a sum of least-squared fitted Zernike polynomials over the unit disk, as described in Equation 3.1:

$$S(\rho_w, \theta_w) = z_w = \sum_{g=1}^{G} C_g P_g(\rho_w, \theta_w) + \epsilon_w \quad \text{for w = 1, 2, …, W} \qquad (3.1)$$

The corneal surface $S$ consists of a set of $W$ elevations $S(\rho_w, \theta_w)$ located at polar coordinates $\rho_w$ and $\theta_w$ for $w$ = 1 to $W$. Each elevation $S(\rho_w, \theta_w)$ (equivalently $z_w$) is modeled by summing the product of the $g^{th}$ Zernike polynomial $P_w(\rho_w, \theta_w)$ and the $g^{th}$ coefficient $C_g$ for $g = 1$ to $G$, assuming error $\epsilon_w$. In this study, the Gaussian polynomials were ordered in accordance with the Noll sequential indices. The first polynomial term (the piston), representing the mean height of the surface (as opposed to its shape), was not counted. Therefore, a model will be said to have $J$ (or $G$ – 1) coefficients. For more details on Zernike polynomials.

### *3.2.3. Clinical variables*

The anterior corneal surfaces of the dataset were grouped in accordance with the following clinical parameters (described earlier): (1) geometric variables: BFS R (best-fit sphere radius), WTW (white-to-white diameter), ACD (anterior chamber depth), (2) refraction variables: Ametropia, Astigmatism, (3) demographic variables: Age, Gender. These parameters were first transformed into categorical variables by segmenting them into groups (when needed), as described in Figure 3.2.

### *3.2.4. Analyses*

To evaluate the validity of the clinical classification and of the atlas based on the dataset, the groups of each clinical variable were compared both quantitatively and qualitatively.

*Quantitative comparison.* For each clinical variable, the groups were compared using analyses of variance (ANOVA). The units of clinical variables are in millimeters (mm) for BFS R, WTW and ACD, in degrees for Axis (from 0° to 90°; the Axis values that were above 90° were horizontally flipped to be in the first quarter by doing Axis = 180° – Axis), in diopters (D) for SE, and years old (yo) for Age. The limits of the groups of each clinical variable are the same as for the qualitative evaluation and are described in Figure 3.2. For example, Age has 6 groups (1: 20-30, 2: 30-40, 3: 40-50, 4: 50-60, 5: 60-70, 6: 70-), and so many means (M1 to M6) are presented in Table 3.1 and Table 3.2. For each effect presented, $p < 0.01$.

*Qualitative evaluation.* An average elevation map was constructed for each group of each clinical variable. An *average elevation map* is an elevation map of the average surface of a group of corneal surfaces. The *average surface* was computed by averaging the Zernike coefficients of each surface of the group and by reconstructing a new surface based on the mean coefficients thus obtained. For each group of each clinical variable, the average surface was constructed both in reference to the *common BFS* (the BFS that applies to all groups of the variable, computed as the mean of the BFS of each group). The surfaces represented could be either natural (non-normalized) or normalized (in this case, the distinction between common and group BFS is irrelevant).

## 3.3. Results and interpretation

### *3.3.1. Quantitative evaluation*

The significant results of interest are presented in Table 3.1 (size of each group of each clinical variable for all corneas, for OD corneas only and for OS corneas only) and in Table 3.2 (effects for all corneas; effects for OD and OS corneas only are not presented since no significant Side by Clinical variable interactions were observed).

TABLE 3.1: Sizes of each group of each clinical variable for all corneas, OD corneas and OS corneas

| Variable/N | All surfaces | | | | | | OD surfaces | | | | | | OS surfaces | | | | | |
|---|---|---|---|---|---|---|---|---|---|---|---|---|---|---|---|---|---|---|
| | N1 | N2 | N3 | N4 | N5 | N6 | N1 | N2 | N3 | N4 | N5 | N6 | N1 | N2 | N3 | N4 | N5 | N6 |
| WTW | 861 | 6929 | 819 | --- | --- | --- | 478 | 3656 | 304 | --- | --- | --- | 384 | 3313 | 521 | --- | --- | --- |
| ACD | 601 | 7600 | 408 | --- | --- | --- | 349 | 3894 | 195 | --- | --- | --- | 252 | 3749 | 217 | --- | --- | --- |
| Side | 4438 | 4171 | --- | --- | --- | --- | 4438 | --- | --- | --- | --- | --- | 4171 | --- | --- | --- | --- | --- |
| Ametropia | 4974 | 3509 | 126 | --- | --- | --- | 2518 | 1855 | 65 | --- | --- | --- | 2473 | 1684 | 61 | --- | --- | --- |
| Age | 1641 | 2961 | 2423 | 1187 | 222 | 175 | 836 | 1496 | 1234 | 611 | 131 | 130 | 805 | 1465 | 1189 | 576 | 91 | 45 |
| Gender | 4364 | 4245 | --- | --- | --- | --- | 2241 | 2197 | --- | --- | --- | --- | 2149 | 2069 | --- | --- | --- | --- |

TABLE 3.2: Mean values of the significant main ANOVA effects with OD+OS corneal surfaces.

| CLINICAL VARIABLE | | MEAN PER GROUP | | | | | |
|---|---|---|---|---|---|---|---|
| IV | DV | M1 | M2 | M3 | M4 | M5 | M6 |
| WTW | BFS R | 7.78 ± 0.23 | 7.92 ± 0.22 | 8.03 ± 0.24 | -- -- | -- -- | -- -- |
| | SE | -3.60 ± 2.65 | -3.40 ± 2.42 | -3.32 ± 2.18 | | | |
| Side | BFS R | 7.90 ± 0.25 | 7.92 ± 0.25 | -- -- | -- -- | -- -- | -- -- |
| | WTW | 11.89 ± 0.40 | 11.80 ± 0.37 | -- -- | -- -- | -- -- | -- -- |
| | ACD | 3.70 ± 0.37 | 3.67 ± 0.38 | -- -- | -- -- | -- -- | -- -- |
| | Axis | 27.19 ± 30.67 | 28.13 ± 31.68 | -- -- | -- -- | -- -- | -- -- |
| | SE | -3.51 ± 2.38 | -3.37 ± 2.48 | -- -- | -- -- | -- -- | -- -- |
| | Age | 39.74 ± 10.75 | 40.74 ± 12.05 | -- -- | -- -- | -- -- | -- -- |
| Ametr. | ACD | 3.76 ± 0.32 | 3.61 ± 0.40 | 3.06 ± 0.42 | -- -- | -- -- | -- -- |
| Age | WTW | 11.88 ± 0.41 | 11.86 ± 0.38 | 11.84 ± 0.37 | 11.80 ± 0.37 | 11.74 ± 0.46 | 11.72 ± 0.47 |
| | ACD | 3.90 ± 0.28 | 3.79 ± 0.31 | 3.63 ± 0.33 | 3.45 ± 0.35 | 3.19 ± 0.36 | 3.02 ± 0.42 |
| | Axis | 23.40 ± 29.71 | 25.20 ± 29.97 | 29.97 ± 31.54 | 34.93 ± 33.08 | 34.86 ± 33.78 | 34.99 ± 31.08 |
| | SE | -4.06 ± 2.09 | -3.74 ± 1.99 | -3.57 ± 2.29 | -2.64 ± 2.83 | -0.39 ± 3.04 | 0.12 ± 3.09 |
| Gender | BFS R | 7.97 ± 0.24 | 7.85 ± 0.24 | -- -- | -- -- | -- -- | -- -- |
| | WTW | 11.92 ± 0.39 | 11.76 ± 0.38 | -- -- | -- -- | -- -- | -- -- |
| | ACD | 3.75 ± 0.37 | 3.62 ± 0.37 | -- -- | -- -- | -- -- | -- -- |
| | SE | -3.29 ± 2.32 | -3.58 ± 2.53 | -- -- | -- -- | -- -- | -- -- |

*Geometric parameters*

*WTW:* The WTW is positively associated with the BFS R, as observed in [3,14] and with SE [7].

*ACD:* The ACD is negatively related to SE, as found in [9].

*Side:* OD and OS eye corneas present a rough interocular symmetry on the clinical variables at hand (BFS R, WTW, ACD, Axis). The small differences observed are comparable to those found in [51] and can be reduced by controlling for the significant effect of Side on Age.

*Refraction parameters*

*Ametropia:* From myopia to hyperopia, an increase in SE is associated with a lower ACD, as in [9,13].

*Demographic parameters*

*Age:* The WTW of older people (groups 5 and 6) is slightly lower than that of young adults (groups 1 and 2), as shown in [11]. The ACD decreases as adults aged, as shown in [8,20,21,52]. The Axis increases at approximately 50 yo (group 4), in accordance with the expected evolution in old age toward against-the rule astigmatism [16]. Finally, a progressive increase in the mean SE value with age in adulthood is observed, in accordance with [22] and [23].

*Gender:* Compared to men, women have a smaller BFS R [3,14] and WTW [7,11,19], a smaller ACD [8,20,24], and a lower SE [25].

Overall, these results describing statistically the clinical variables included in the dataset are consistent with the literature. Therefore, the atlas of average elevation maps presented next should also agree with the literature.

### *3.3.2. Qualitative evaluation*

Figure 3.2 presents the atlas of average elevation maps for each clinical variable in reference to the common BFS. Each average elevation map represents the average of the natural normal anterior OD surfaces of each group of each clinical variable. The size of each group (N) is presented along with the mean BFS radius (R) of the group. As a complement, Figure 3.3 presents elevation maps in which the surfaces represented are normalized to cancel out the effect of size. Only the normalized maps that differ visually from the corresponding natural maps are represented, namely BFS R, WTW, Ametropia and Gender.

*Geometric parameters*

(a) *Best-fit sphere radius (BFS R).* In their natural version (Figure 3.2 (a)), the BFS R maps show a coldening of central colors along with a warming of temporal and nasal colors, and thus an evolution toward a flatter cornea as the BFS R increases, in accordance with Gatinel et al. (2011) [3]. This effect disappears almost completely in the normalized version of the BFS R maps (Figure 3.3 (a)). This shows that the effect of flattening observed in the natural surface maps is mostly due to a difference in size of the corneas as the BFS R increases, as opposed to a significant difference in shape and asphericity that would be independent of the corneal size.

(b) *White-to-white diameter (WTW).* A transition toward colder central colors and (slightly) warmer temporal and nasal colors is also observed in the natural WTW maps (Figure 3.2 (b)) but not as marked as for the BFS R maps. This flattening effect is in agreement with the fact that the WTW correlates strongly with the radius of curvature [7], which is itself strongly related to the BFS R, and negatively to corneal curvature [7]. As for BFS maps, this flattening effect is reduced when the maps are constructed with normalized corneal surfaces (Figure 3.3 (b)). However, contrary to BFS maps, it does not disappear completely, leaving a slight flattening effect that cannot be due to the BFSR but should be due to the eccentricity of the corneal curvature. This is consistent with the finding of Hashemi et al. (2015) that the WTW is related to SE, a first-order aberration in which the cornea is out of focus due to some departure from the on-focus curvature.

(c) *Anterior chamber depth (ACD).* The natural ACD maps (Figure 3.2 (c)) show a progression toward less color change in the central corneal area, indicative of a flatter cornea for a similar corneal size (the BFS R is around 8.0 mm). This is in agreement with the fact that the ACD is negatively correlated with the corneal curvature [8].

(d) *Side.* The natural OD maps and OS maps (Figure 3.2 (d)) display a quasi-perfect corneal horizontal symmetry [10,51]. Also, in both eyes, the warm color pattern is more present on the temporal side. This reveals an intraocular asymmetry of asphericity in each eye, with more flattening nasally (where the colors remain blue) than temporally (where they evolve rapidly from warm to green), as shown in [10].

(a) BFS R (group 1: from 7.06 to 7.63 mm, group 2: from 7.63 to 8.19 mm, group 3: from 8.19 to 8.99 mm)

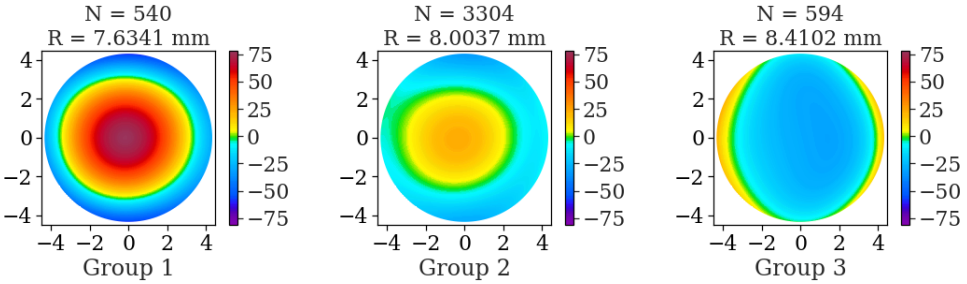


(b) WTW (group 1: from 10.40 to 11.36 mm, group 2: from 11.36 to 12.32 mm, group 3: from 12.32 to 14.10 mm)

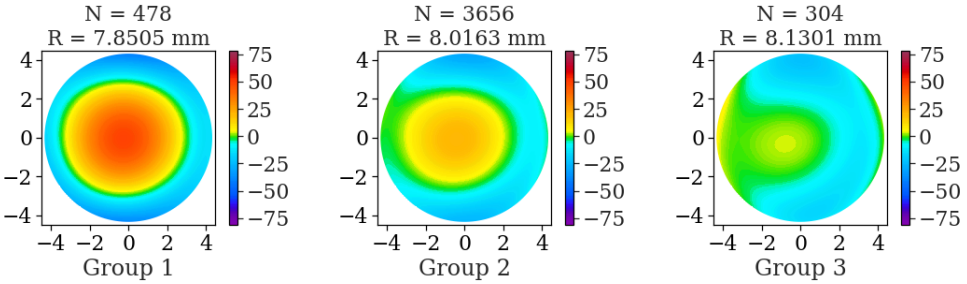


(c) ACD (group 1: from 1.96 to 3.11 mm, group 2: from 3.11 to 4.26 mm, group 3: from 4.26 to 6.92 mm)

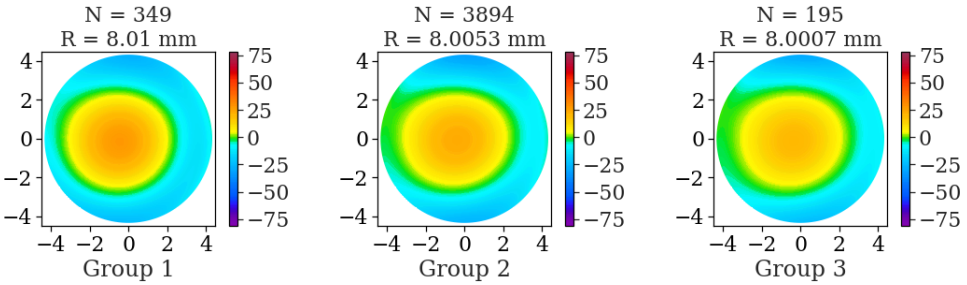


(d) Side (group 1: OD, group 2: OS)

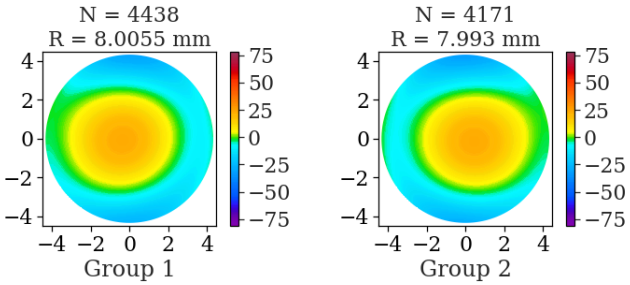

(e) Ametriopia (group 1: moderate or high myopia, SE < -3 D, group 2: emmetropia or low ametropia: -3 D ≥ SE ≤ 3 D, group 3: moderate or high hyperopia: SE > 3 D)

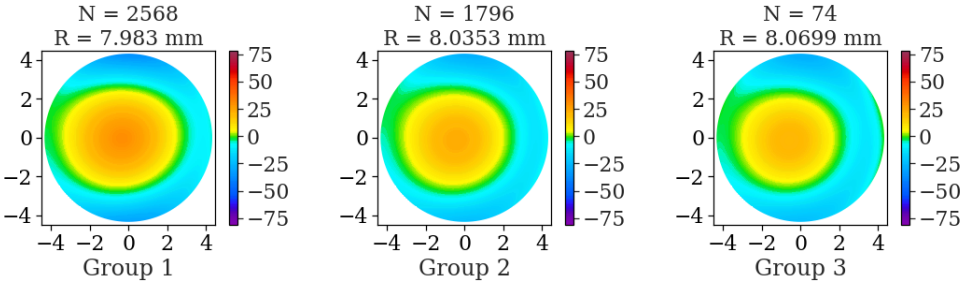


(f) Astigmatism (1: group 1: "with the rule": the axis is between 0° and 30° or between 150° and 180°, 2: group 2: oblique: the axis is between 30° and 60° or between 120° and 150°, group 3: "against the rule": the axis is between 60° and 90° or between 90° and 120°)

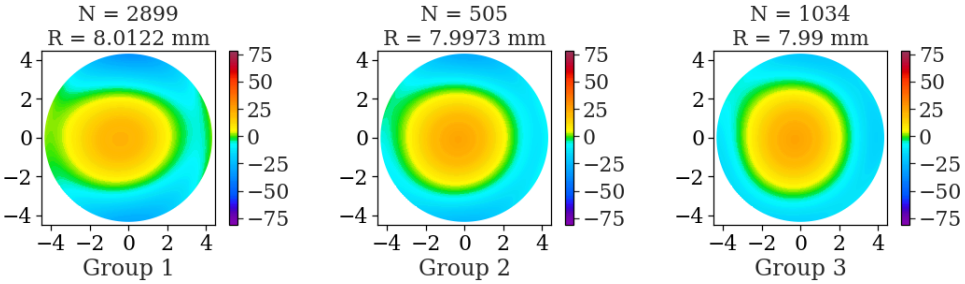


(g) Age (group 1: from 20 to 29 yo, group 2: from 30 to 39 yo, group 3: from 40 to 49 yo, group 4: from 50 to 59 yo, group 5: from 60 to 70 yo, group 6: 70 yo and more).

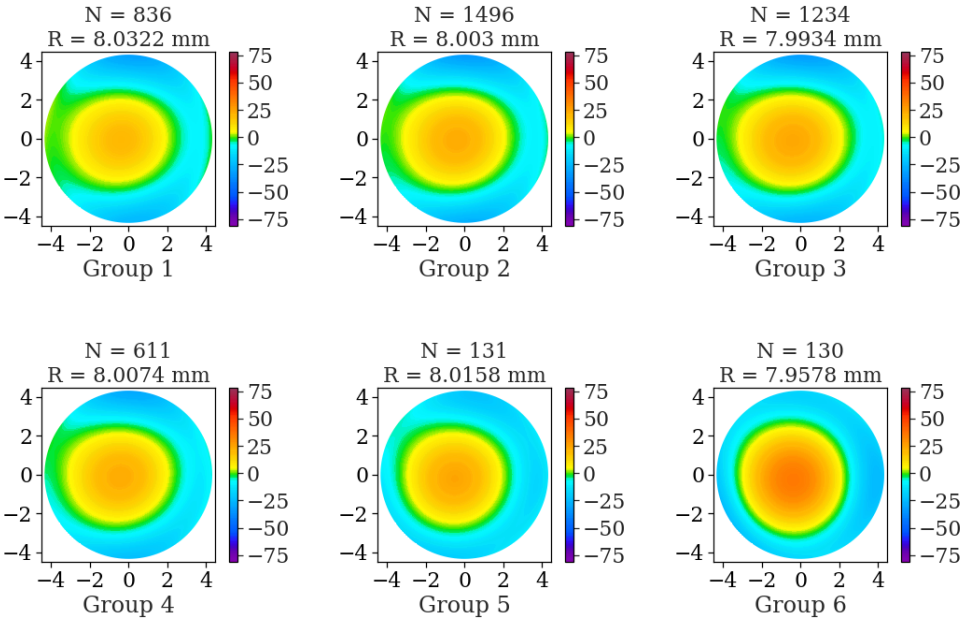

(h) Gender (group 1: M, group 2: F)

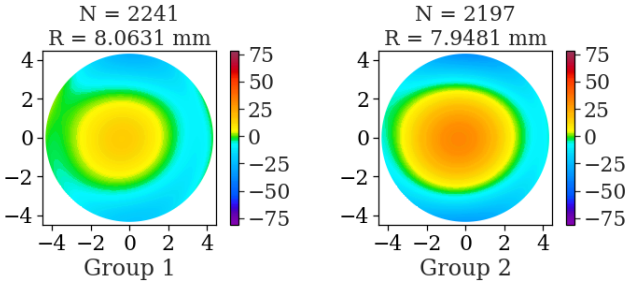


FIGURE 3.2: Atlas of average elevation maps of natural OD anterior corneal surfaces for (a) BFS R, (b) WTW, (c) ACD, (d) Side, (e) Ametropia, (f) Astigmatism, (g) Age and (h) Gender. The common BFS is used as a reference. The X and Y axes are in mm, and the Z axis (color scale) is in µm.

(a) BFS R (group 1: from 7.06 to 7.63 mm, group 2: from 7.63 to 8.19 mm, group 3: from 8.19 to 8.99 mm)

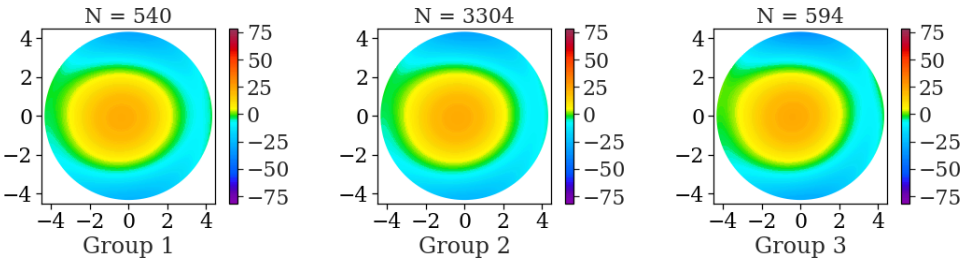


(b) WTW (group 1: from 10.40 to 11.36 mm, group 2: from 11.36 to 12.32 mm, group 3: from 12.32 to 14.10 mm)

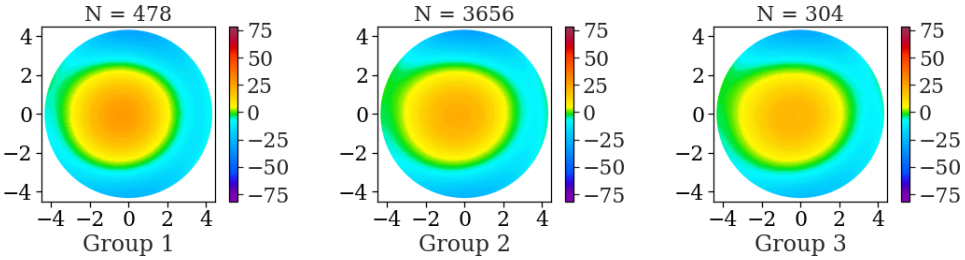


(e) Ametriopia (group 1: moderate or high myopia, SE < -3 D, group 2: emmetropia or low ametropia: -3 D ≥ SE ≤ 3 D, group 3: moderate or high hyperopia: SE > 3 D)

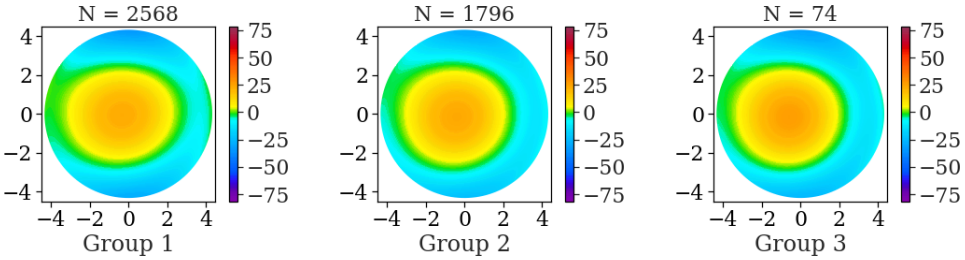

(h) Gender (group 1: M, group 2: F)

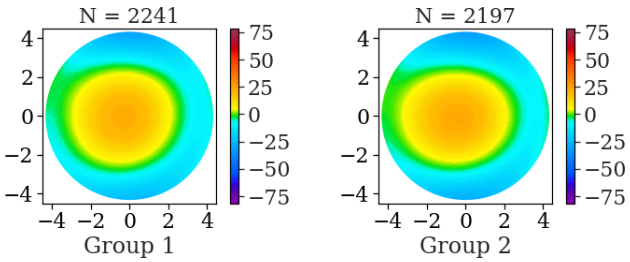


FIGURE 3.3: Average elevation maps of normalized OD corneal surfaces for each group of BFS R in reference to the normalized BFS when they differ qualitatively from corresponding maps with natural surfaces. Axes *X* and *Y* are in mm and axis *Z* (color scale) is in µm.

*Refraction parameters*

(e) *Ametropia (AMT).* From myopic to hyperopic corneas, the natural maps display a slight reduction in size of warm colors centrally as the SE increases (Figure 3.2 (e)). This is consistent with the fact that the SE is known to be directly related with the WTW [11] and negatively with the corneal curvature [11,12]. Besides, the reduction of the central warm pattern in natural maps is the opposite of the natural ACD maps (this is even clearer with the normalized surfaces in Figure 3.3 (e)). This is indicative of an inverse relation of SE with ACD [9,13].

(f) *Astigmatism (AST).* The astigmatism maps (Figure 3.2 (f)), in which the axis gets progressively more vertical, display a progressive vertical stretching of the warm central pattern, and thus a decrease of the curvature of the vertical meridian and increase of the curvature of the horizontal meridian [15,16].

*Demographic parameters*

(g) *Age.* Age maps display a progressive vertical stretching of their yellow-orange pattern that increases more rapidly in old age (Figure 3.2 (g)). This progression is consistent with the expected transition from WTR to ATR astigmatism in normal corneas [15]–[18,24]. The reddening and narrowing of the warm central pattern is also indicative of a reduction of the ACD with age (see the natural ACD maps in reverse order) [8,13,20,21].

(h) *Gender.* When compared to the male map, the female map presents a larger and warmer central pattern of warm colors along with a smaller BFS R (Figure 3.2 (h)). Indeed, being smaller, female corneas are known to have a steeper curvature [11,14,19], a smaller WTW [7,11,19]. If Gender maps are normalized to eliminate the effect of size on the corneal curvature (Figure 3.3 (h)), this effect is reduced, but the female map remain slightly redder than the male map, which is indicative of a smaller ACD (see the natural ACD maps) [8,20,24].

In sum, the average elevation maps of the reference atlas are globally consistent with the literature on the shape of the normal anterior corneal surface. They also agree with or are complementary to the statistical results presented earlier.

## 3.4. Discussion

In this study on clinical classification, we presented an atlas of average elevation maps to visualize the effects of different clinical variables on the shape of the anterior surface of the normal cornea geometrically modeled with Zernike coefficients.

These clinical variables covered different features of the cornea dealing with its geometric shape (WTW, ACD, Side), refractive power (Ametropia, Astigmatism) and demography (Age, Gender), instead of covering only two or three clinical features to make a proof of concept, as is usually the

case. The dataset was statistically evaluated, and the atlas based on this dataset was visually evaluated.

From a statistical standpoint, the dataset proved to be overall consistent with the literature on each of the examined clinical variables. Thus, concerning geometric variables, WTW was positively associated with the BFS R [3,14], while the ACD was negatively related to the SE [9]. The Side displayed an interocular symmetry between OD and OS surfaces [51]. Concerning refraction variables, the increase in SE (Ametropia) was associated with a lower ACD [9,13]. As for the increase of axis (Astigmatism), it is associated with a decrease of curvature of the vertical meridian and increase of curvature of the horizontal meridian. Regarding demographic parameters, Age was positively related to Axis [15]–[18,24] and to SE [22], and negatively with WTW [11] and ACD [8,20,21,52]. As for Gender, it was associated with a smaller BFS R [3,14] and with a larger corneal curvature [11,14,19], WTW [7,11,19], ACD [8,20,24] and SE [25] for women than for men.

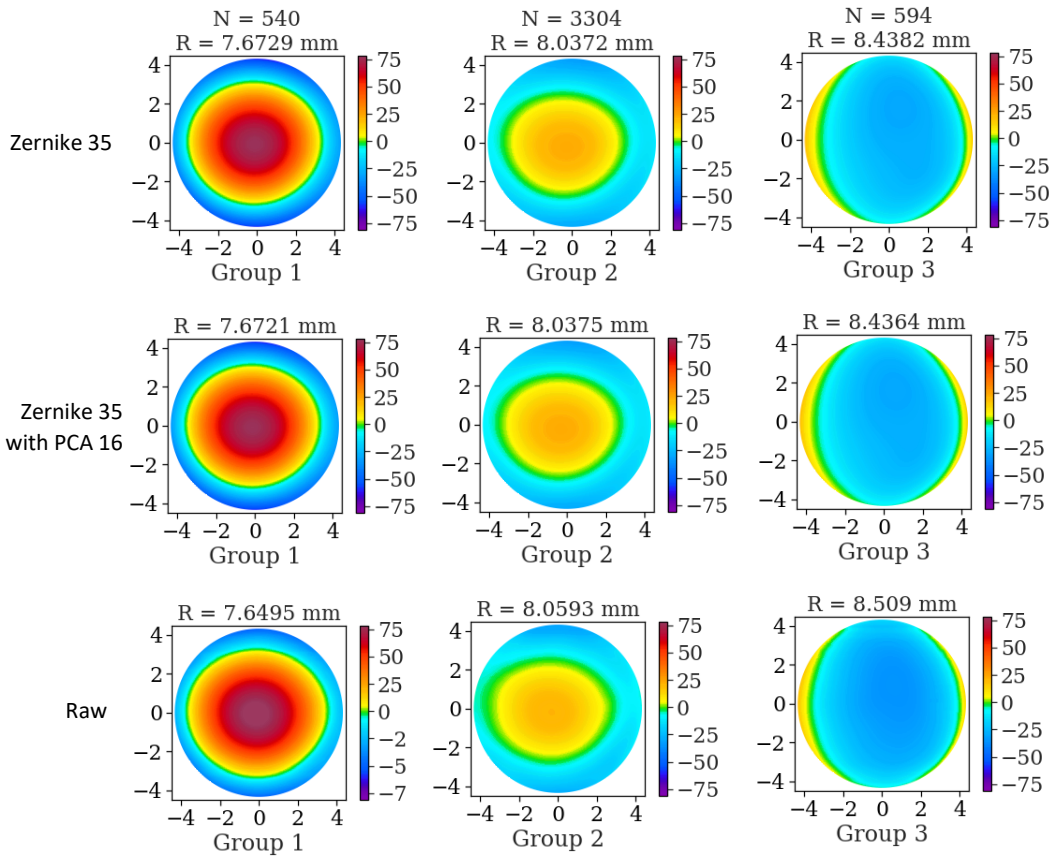


FIGURE 3.4: Average elevation maps of OD corneal surfaces for Age groups: (a) average surfaces modeled with 35 Zernike coefficients (first row), (b) average surfaces modeled with 35 Zernike coefficients and reduced to 16 principal components (second row), and (c) original average raw surfaces (third row). The maps are in reference with the common BFS of Age groups. Axes X and Y are in mm and axis Z (color scale) is in µm.

Having shown that the dataset was consistent with the literature, it could be expected that the atlas would display corneal shape transformations that are also in line with the literature. The visual examination of the corneal shape transformations displayed in the atlas showed that this was the case. As expected, the BFS R maps were consistent with an evolution toward a flatter cornea as the BFS R increased that was not related to the shape of the cornea but to its size ([3]. The WTW maps

showed a similar effect, but less pronounced, in agreement with the fact that the WTW are known to correlate positively with the radius of curvature [7], and thus with the BFS R (Gatinel et al., 2011), but negatively with corneal curvature [3,7]. The ACD maps signaled a reduction of the corneal curvature that was not related to the corneal size [8]. The Side maps displayed a quasi-perfect inter-ocular corneal horizontal symmetry [10,51] along with an intraocular asymmetry of asphericity [10]. The ametropia maps were consistent with the SE being directly related with the WTW [11] and negatively with the corneal curvature [11,12] and indirectly with the ACD [9,13]. The astigmatism maps displayed a transition from "with the rule" to "against the rule" astigmatism [15,16]. The Age maps also presented a transition from "with the rule" to "against the rule" astigmatism [15]–[18,24] along with a reduction of the ACD [8,13,20,21]. Finally, the Gender maps showed that female corneas had a steeper curvature [11,14,53], a smaller WTW [7,11,19] and a smaller ACD [8,20,24].

Once verified, a corneal shape atlas can serve as a validation and interpretation tool to assess the datasets used and produced in a number of applications (clustering, regression, etc.). It is similar to an atlas that would be directly constructed by averaging raw topographic surfaces [38], as shown in the third row of Figure 3.4, where the average maps for WTW groups are based on raw topographic surfaces. It is also possible to increase the number of Zernike coefficients to gain accuracy, as shown in the first row of Figure 3.4, where 35 Zernike coefficients are used, or else to reduce the dimensionality of the dataset by applying a feature extraction algorithm on top of geometric modeling without losing any apparent accuracy, as shown in the second row of Figure 3.4.

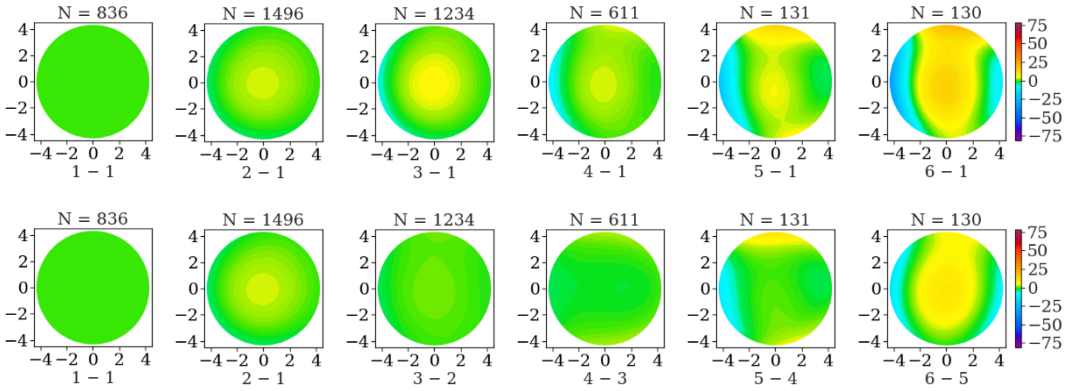


FIGURE 3.5: First row: difference maps of OD corneal surfaces reference with Age group 1. Second row: difference maps of OD corneal surfaces reference with the preceding Age group. Axes *X* and *Y* are in mm and axis *Z* (color scale) is in µm.

Allowing us to visualize the mean effects of clinical variables on the corneal shape, average elevation maps are indeed pivotal in the toolkit of group maps. However, other useful types of group maps can also be produced to highlight other aspects of the effects of clinical variables on the corneal shape, such as difference average maps, standard deviation maps or p value maps [38]. For instance, difference maps can be obtained by subtracting the elevations of two maps being compared to highlight their difference in elevations. Figure 3.5 (g) presents a series of difference maps in which Age groups 1 to 6 are presented in reference to group 1 (from 20 to 29 yo) in the first row and in reference to the preceding age group in the second row (pure green represents a total absence of change, as shown in the 1 – 1 maps). These difference maps highlight in another manner how and when the bulk of the transition takes place in aging from with-the-rule to against-the-rule astigmatism. In particular, while little change takes place in middle age (see maps with

groups 3 and 4, between 40 and 60 yo), the bulk of the most of the change takes place in older groups (see maps with groups 5 and 6), as discussed above.

## 3.5. Conclusion

This study presented a clinical classification of the anterior surface of normal adult corneas based on a number of clinical variables known to be associated with the shape of the cornea. To visualize the effects of these variables on the corneal shape, an atlas of average elevation maps representing the average surface of each group for each parameter was constructed and verified. Such a visualization tool can serve not only for clinical and instructional purposes but also for interpretation and validation purposes as a ground truth in different biometric or machine learning applications (clustering, prediction, etc.). Further developments include extending the coverage of the clinical parameters associated with the corneal shape, constructing an atlas for other aspects of the cornea (posterior surface, intersurface volume) and for other types of corneas (keratoconus, Fuch, etc.), constructing other types of group maps (standard deviation maps, count maps, p value, etc.), and using the atlas as a reference to assess comparable input datasets (surfaces modeled with spherical harmonics and or preprocessed with feature extraction, etc.) and output datasets (predictions, clusters, supervised classes, etc.).

## Acknowledgements

This work was supported by the QVRN (Quebec Vision Research Network), the FRQNT (Fonds de recherche du Québec Nature et Technologie) and the MUTAN (University Mission of Tunisia in North America).

# CHAPTER 4: UNSUPERVISED CATEGORIES OF NORMAL CORNEAL SHAPES

Hala Bouazizi[1], Isabelle Brunette[2,3], Jean Meunier [1,2]

1 Department of Computer Science and Operations Research, University of Montreal, Montreal, Quebec, Canada
2 Department of Ophthalmology, University of Montreal, Montreal, Quebec, Canada
3 Maisonneuve-Rosemont Hospital Research Center, Montreal, Quebec, Canada

## Abstract

The unsupervised classification of corneal surfaces is recent in ophthalmology. Most studies have tried to apply clustering algorithms to datasets of corneas of different clinical types (normal, keratoconus, etc.) in an attempt to verify whether their classification could be automated. A few have also tried to classify keratoconus corneas into clinical subtypes and assess their consistency with standard methods of diagnosis. This automated classification task remains to be done for normal corneas. The present study investigated a large number of normal adult corneas in an exploratory attempt to identify their natural groupings. The focus was on the anterior surface, which is more prone to changes in a normal population. The raw corneal data were either in their natural (non-normalized) state or normalized. To facilitate groupings, both the natural and normalized corneal data had their dimensionality reduced by Zernike polynomial modeling. The resulting clusters were evaluated using different clustering scores ($SPR^2$, $R^2$), representations (coefficient polar charts, coefficient scatter plots, average elevation maps, average profile cuts) and statistical comparisons (on different clinical measures). A number of hard and soft linear and nonlinear clustering methods were tested in this way, but k-means proved to be the most effective for this task. The best number of clusters for natural and normalized corneal surface data was four, but while natural corneas were clustered in accordance with their curvature (Zernike coefficient of defocus), normalized corneal data were clustered in accordance with their axis (Zernike coefficient of vertical astigmatism).

**Keywords:** cornea, Zernike polynomials, clustering, corneal topography, average elevation map, k-means

## 4.1. Introduction

The classification of corneas is essential in ophthalmological research for accurate diagnosis or data preprocessing. It is traditionally done manually through the expert examination of clinical data (topographies, etc.). Relatively new to the domain of corneal classification, machine learning (ML) can contribute to the automation of this tedious process and to its accuracy through a systematic examination of the distribution of data that does not require any a priori knowledge of this distribution. Most of the time, ML classification still necessitates the manual labeling of the training set through expert supervision. In unsupervised categorization, however, such manual labeling is no longer needed (except for validation purposes), and the focus is solely on the distribution of data. Only a few studies have applied unsupervised classification to corneal data, most of which to automate the process of establishing their clinical status (diagnosis).

In Yousefi et al. (2018) [54] and Hallet et al. (2020) [55], clustering was applied to a large number of clinical parameters of the corneal surface. These parameters were first reduced by feature extraction to only a few latent variables. A clustering method was then applied to group the corneas into a prespecified number of clusters in the hope of automating their diagnosis. The effectiveness of this clustering process was assessed in reference to a ground truth based on an established keratoconus typology. More precisely, in [54], feature extraction took place linearly by principal component analysis (PCA) and nonlinearly by manifold learning using t-distributed stochastic neighbor embedding (t-SNE) and allowed for the reduction of the initial 420 clinical parameters to two eigenvalues only. A density-based clustering approach was then applied to distinguish different types of keratoconus eyes and separate them from normal eyes. The accuracy of the clusters was assessed based on the Ectasia Status Index (ESI) to establish the ground truth using t-SNE maps to visualize the clusters. A true negative rate of 94.1% was obtained for distinguishing normal corneas from keratoconus corneas (specificity) and a true positive rate of 97.7% for distinguishing keratoconus corneas from normal corneas (sensitivity). In [55], feature extraction was achieved by variational autoencoder (VAE), a deep learning algorithm that reduced the initial set of 30 clinical variables to two latent variables only. Gaussian random sampling was then used to produce four clusters and classify so many types of keratoconus corneas in accordance with the Amsler-Krumeich (A-K) classification system of keratoconus corneas. The accuracy of clusters was established with performance under the curve (AUC) scores using a *receiver operating characteristic* (ROC) curve. The scores were 0.91, 0.87, 0.79 and 0.99 for each keratoconus type.

In Zéboulon et al. (2020) [56] and Bouazizi et al. (2018) [14], clustering was directly based on the shape of corneal surfaces (as defined by a grid of elevations), instead of a set of clinical parameters as in the other studies, and also involved a prior step of dimensionality reduction. Like the former studies, Zeboulon et al. were interested in the clustering of a dataset of unlabeled normal and irregular corneas (corneas with keratoconus, Fuchs or refractive surgery) in an attempt to automate their diagnosis and identify natural subtypes of keratoconus corneas [56]. The data involved the elevations of the anterior surface of the cornea and of the posterior surface as well as the intersurface volume (pachymetry). Feature extraction was based on t-SNE and allowed for the reduction of the initial set of 10000 x 3 corneal surface or intersurface elevations to 3 eigenvalues only. Clustering was achieved using the HDBSCAN algorithm. The accuracy of the clusters was established in reference to the ESI score, and their success rate was 96.5% (with better results for normal corneas than irregular corneas). Finally, the study of Bouazizi et al. focused on normal corneas to identify their natural groupings based on data distribution [14]. Dimensionality reduction was achieved by geometric modeling (Zernike polynomials) instead of feature extraction, and the unsupervised classification of corneas was based on agglomerative clustering. Contrary to the other studies, the best number of clusters (four) was not prespecified but was discovered based on their degree of compactness and separation thanks to a dendrogram and clustering scores ($SPR^2$ and $R^2$). The four best clusters identified were assessed using average elevation maps and profile cuts that represent their average shape. The clinical variable that best reproduced the transformations of

average corneal shapes from cluster to cluster, as visualized with average maps and profile cuts, was the corneal curvature.

The present study explores the data distribution of normal adult corneas in an attempt to identify their most significant groupings by achieving the non-supervised classification (clustering) of the corneal dataset. The focus is on the anterior corneal surface, which is the main responsible for the refractive power of the cornea. The first goal, pursued in pretests, is to identify an effective clustering method among the different types of methods available (hard and soft clustering, linear and nonlinear clustering, with or without feature extraction). To this end, the relevance, delimitation (compactness and separation), specificity and clinical conformity of the clusters produced by the examined methods are examined using a number of evaluation tools, including clustering scores, modeling coefficient representations, corneal surface representations, and clinical feature comparisons. To make clustering possible, the large dimensionality of the corneal dataset is first reduced by geometrical modeling before the clustering methods applies, with or without feature extraction, and with or without normalization of the corneal surfaces. Once the most effective clustering method is identified in pretests, it remains, as the main goal of this study, to characterize the clusters produced to identify the clinical features that distinguish them. It is assumed that these most discriminant features should play a prominent role in the distribution of anterior corneal shape data. First-order aberrations like defocus and astigmatism, often found in normal corneas, are good candidates.

## 4.2. Method

### *4.2.1. Data*

*Collection and description*

The investigated dataset comprises a total of 8609 topographies of the anterior corneal surface of normal corneas obtained from 4941 consenting adult subjects (4245 topographies of female corneas and 4364 topographies of male corneas, distributed into 4438 topographies of OD corneas and 4171 topographies of OS corneas). These topographies, generated by the Orbscan II topographer (Bausch & Lomb, Rochester, NY), are part of the cornea bank (database for the anatomopathological, functional and surgical characterization of the cornea) [5], which compiles more than 36000 corneal topographies. This database was screened to ensure that subjects had no history of ocular disease, ocular surgery, or recent contact lens wear. Each topography, recorded as a 101×101 grid of elevations (heights) evenly spaced (every 0.1 mm) along the $X$ (left-right) and $Y$ (up-down) axes, is accompanied by demographic information about the participant (gender, age) and geometric information on the shape of the cornea (white-to-white diameter, anterior chamber depth, eye side) and refraction information on the visual acuity of the cornea (cylinder, sphere, axis, spherical equivalent). No topography was recorded more than once for the same eye. The experimental procedures involving human subjects described in this paper were approved by the Institutional Review Board. More details are presented in the results section.

*Preprocessing*

The topographies of the database include some artifacts among the elevation points (e.g., missing data, noise) in the periphery. To address these issues, the matrices of elevation points were reduced into 91×91 matrices to eliminate 0.5 mm of radius and clean up the noisiest part of the surface (the image fringe). The resulting dimensionality of the data (8281 elevations), still substantial, had to be further reduced, which was achieved by geometric modeling using 16 Zernike polynomials (Zernike modeling), a number that provides a sufficient accuracy for producing mean surfaces while avoiding overfitting issues.

Zernike polynomials (ZP) are known to be effective for the description of optical aberrations of normal corneas [57]. They display properties of linearity, completeness, orthonormality, and

radiality, with coefficients that are clinically interpretable, an asset for the interpretation of clusters. As shown in Equation 4.1, a Zernike model of corneal surface can be conceived as a matrix of elevations modeled as a sum of least-square fitted Zernike polynomials over the unit disk [57]:

$$S(\rho_w, \theta_w) = z_w = \sum_{g=1}^{G} C_g P_g(\rho_w, \theta_w) + \epsilon_w \quad \text{for w = 1, 2, …, W} \tag{4.1}$$

In Zernike modeling, the corneal surface $S$ consists of a set of $W$ elevations $S(\rho_w, \theta_w)$ located at polar coordinates $\rho_w$ and $\theta_w$ for $w = 1$ to $W$. Each elevation $S(\rho_w, \theta_w)$ (equivalently $z_w$) is modeled by summing the product of the $g^{th}$ Zernike polynomial $P_g(\rho_w, \theta_w)$ and the $g^{th}$ coefficient $C_g$ for $g = 1$ to $G$, assuming error $\epsilon_w$. The $G$ Zernike polynomial terms were ordered in accordance with Noll sequential indices: 1: piston, 2: horizontal tilt, 3: vertical tilt, 4: defocus, 5: oblique astigmatism, 6: vertical astigmatism, 7: vertical coma, 8: horizontal coma, etc. The first term (the piston), which represents the mean height of the surface (as opposed to its shape), was not used nor counted (having a much larger magnitude than the shape coefficients, its use in clustering pretests yielded irrelevant results based mainly on the mean height of corneal surfaces). Therefore, a model of the corneal shape will be said in this study to have $J$ (= $G$ – 1) coefficients. $J$ = 16 was chosen as being accurate enough for the present purpose without causing overfitting issues (modeling error lower than the repeatability error of the topographer, RMSE = 6.18 µm for a 91×91 matrix). More details on Zernike polynomials can be found in [57].

### *4.2.2. Clustering method*

A number of clustering methods were examined in pretests, including two hard linear methods (agglomerative clustering and k-means), one hard nonlinear method (spectral clustering), and one soft clustering method (in which more than one cluster can be assigned with a probability of cluster belonging). These methods were tested with or without feature extraction (PCA for linear feature extraction or t-SNE for nonlinear feature extraction). They applied to anterior corneal surfaces reduced by geometrical modeling (with Zernike polynomials) in their natural (non-normalized) or normalized state. As will be exposed in the discussion, once evaluated in pretests in the way described in the next section, the most effective method for both natural and normalized corneal surfaces was found to be k-means, applied without feature extraction. This article will accordingly focus on the results produced by this hard linear top-down clustering method. In *k-means clustering*, data are clustered around $k$ groups to minimize the within-cluster sum of squares (WCSS) of each group. Each sample is assigned to its nearest centroid, which is then recomputed, and recursively until the WCSS falls below a minimum.

### *4.2.3. Clustering evaluation*

In this study, the success of the corneal clustering task was evaluated using different evaluation tools, including clustering scores, coefficient representations, surface representations and feature comparisons.

*Clustering scores*

The clear delimitation of clusters (compactness and separation) is largely dependent on $k$, the number of clusters produced. Following Halkidi et al. (2001) [39], the $SPR^2$ and $R^2$ scores were used to determine the best $k$ (curves shown in Figure 4.1).

1) *$SPR^2$* (semi-partial $R^2$). Measuring directly the gain of compactness produced when a new cluster is added, the $SPR^2$ score can be computed as the difference between two successive (WCSS) scores as $k$ increases. The WCSS estimates the average distance of a cluster's samples to its centroid. The $SPR^2$ curve is easier to interpret than the WCSS curve: the best $k$ is located at the end of the elbow, where the curve becomes (roughly) flat.

2) $R^2$. The $R^2$ is a direct measure of cluster separation. It is estimated as the ratio between the between cluster sum of square (BCSS), which measures the average distance between the cluster centroids, and the total cluster sum of square (TCSS), which measures the total distance between all samples. The best *k* is located at the knee of the curve.

*Coefficient representations*

1) *Coefficient polar charts*. These charts were used to represent the mean coefficients of the surfaces of a cluster. In Figure 4.2, each line relates the means of the J coefficients of a cluster (to help visualize the distance between them). The more the cluster lines are distinct and equally separated for a given coefficient (from $C_1$ to $C_{16}$), the more this coefficient is discriminant and effective as a clustering criterion in the clustering process.

2) *Coefficient scatter plots*. Complementary to coefficient polar charts, coefficient scatter plots represent the distribution of the coefficients for each *J* across the surfaces of each cluster. Figure 4.3 consists of two rectangle triangles separated by the diagonal that consist of a series of scatter plots. The lower one holds for clusters based on natural corneal surfaces and the upper one for those based on normalized corneal surfaces. In each of these triangles, the scatter plots represent the distribution of the Zernike coefficients used to model each surface of a cluster for each possible pair of coefficients ($C_1$ vs. $C_2$, $C_1$ vs. $C_3$, etc.). In the scatter plots, each cluster is assigned a particular color. The more the colors are clearly delimitated across the scatter plots for a given Zernike coefficient, the more this coefficient is discriminant and effective as a clustering criterion.

*Surface representations*

1) *Average elevation maps*. These maps were used to represent the average surface of the surfaces of each cluster (see Figure 4.4). An elevation map is a topographic representation of the elevations of a corneal surface. Assuming that the shape of the cornea is close to a sphere, the elevations are represented in reference to the sphere that best fits the surface, the best-fit sphere (BFS). The elevations that are above the BFS are pictured with warm colors, and those that are below the BFS with cold colors. In an average elevation map, the surface represented is an average surface (the average of a group of surfaces). The average surface was computed for each cluster by averaging the Zernike coefficients of the surfaces of the cluster and by reconstructing an average corneal surface on this basis (this is equivalent to computing the means of their elevations). A *cluster BFS* is the BFS of the average surface of a cluster. A *common BFS* is the average BFS of all clusters of natural surfaces, obtained by averaging their cluster BFSs. Note that for normalized surfaces, this distinction is irrelevant as the cluster BFSs are (about) the same.

2) *Average profile cuts*. These representations are horizontal or vertical profile cuts of the average cluster surfaces (see Figure 4.5). They are computed as the horizontal or vertical median elevations of the average corneal surface of each cluster. For a better visualization, the differences of the cluster surface cuts with the common BFS cut and the standard deviations (in grey) are amplified 10 times.

Feature comparisons

Clusters were compared based on the clinical features known to be associated with the clustering criterion found to distinguish them the best. For example, if the clusters of natural corneas were found to be mainly distinguished by $Z_2^0$, the Zernike coefficient of defocus, they were compared based on clinical features associated with defocus, such as the corneal curvature and white-to-white. Feature comparisons of clusters were based on analyses of variance.

## 4.3. Results

### *4.3.1. Clustering scores*

Figure 4.1 presents the $SPR^2$ and $R^2$ curves for the k-means clustering of natural (left) and normalized (right) anterior OD corneal surfaces modeled with 16 shape Zernike coefficients. Using the elbow and knee techniques, it can be seen that the best $k$ value for a clear delimitation should be $k = 4$.

### *4.3.2. Coefficient representations*

*Coefficient polar charts.* The first row of Figure 4.2 presents the full coefficient polar charts for the k-means clustering of anterior OD surfaces modeled with $J = 16$ and $k = 4$. In the left chart, the surfaces are natural, while they are normalized in the right chart. The second row presents a zoom-in view of each of these charts that focuses on the most discriminant Zernike coefficient, that is, $C_3$ for natural surfaces and $C_5$ for normalized surfaces. Indeed, for natural surfaces, the only coefficient where the $k$ cluster lines are clearly distinct is $C_3$, whereas for normalized surfaces, the only one is $C_5$. Note that $C_3$ (the coefficient of the third shape polynomial in Noll indices) is also known as $Z_2^0$ in double-index notation, which is the coefficient of defocus. As for $C_5$ (the coefficient of the fifth shape polynomial), also known as $Z_2^2$, it is the coefficient of vertical astigmatism.

*Coefficient scatter plots.* In Figure 4.3, a series of coefficient scatter plots successively present the distribution of pairs of coefficients ($C_1$ vs. $C_2$, $C_1$ vs. $C_3$, etc.) on the $X$ and $Y$ plot axes in clusters produced by k-means clustering for $k = 4$ using natural surfaces (lower rectangle triangle) and normalized surfaces (upper rectangle triangle) modeled with $J = 16$. As can be seen, with its clearly delimitated cluster colors, $C_3$ is by far the most discriminating Zernike coefficient for natural surfaces, whereas $C_5$ is the most discriminating one for normalized surfaces.

### *4.3.3. Surface representations*

*Average elevation maps.* Figure 4.4 shows a series of average elevation maps of the clusters produced by k-means clustering with $k = 4$ for natural (first and second rows) and normalized (third row) OD surfaces.

In the first row, the natural maps are in reference to the common BFS. As can be seen, they display a stark shift toward cooler colors at the center of the cornea along with a slight shift toward warmer colors at the nasal and temporal periphery as the BFS R gets larger from one cluster to another, meaning that the surfaces get on average flatter from one cluster to another. In the second row, the natural maps are in reference to their respective cluster BFS to cancel out the effect of the corneal size between clusters. As can be seen, the coldening effect is largely reduced when all clusters have the same average size, but it does not disappear completely: while the warm central pattern keeps its shape, it gets on average slightly more yellow and less red. This means that the reduction of corneal curvature is not entirely due to the corneal size but is in part due to a reduction of eccentricity. Besides, as concerns normalized surfaces (third row), the elevation maps display a progressive narrowing of the central warm color pattern by which the pattern passes from a horizontal state to a vertical state, signaling a transition from "with the rule" (WTR) to "against the rule" (ATR) astigmatism in which the horizontal meridian progressively steepens.

*Average profile cuts.* The horizontal and vertical average profile cuts presented in Figure 4.5 in reference to the common BFS allow us to visualize directly the reduction of curvature from one cluster to another as the BFS R gets larger.

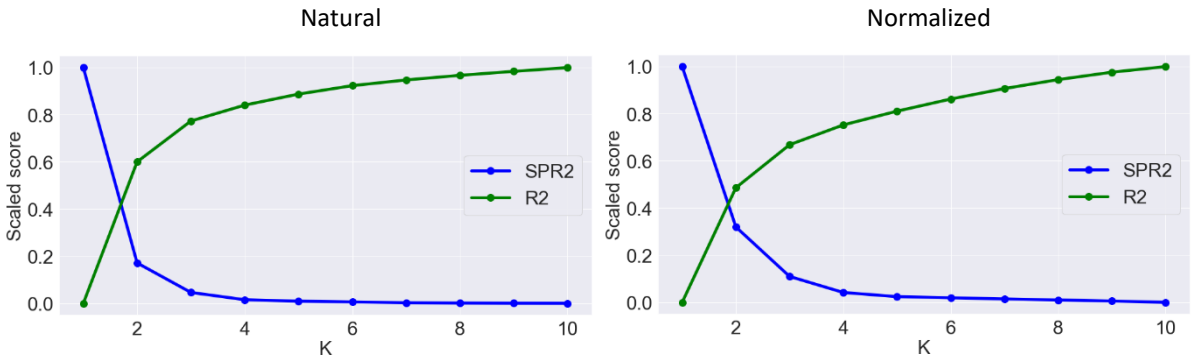


FIGURE 4.1: Clustering score curves for natural (left) and normalized (right) anterior OD corneal surfaces modeled with 16 shape Zernike coefficients.

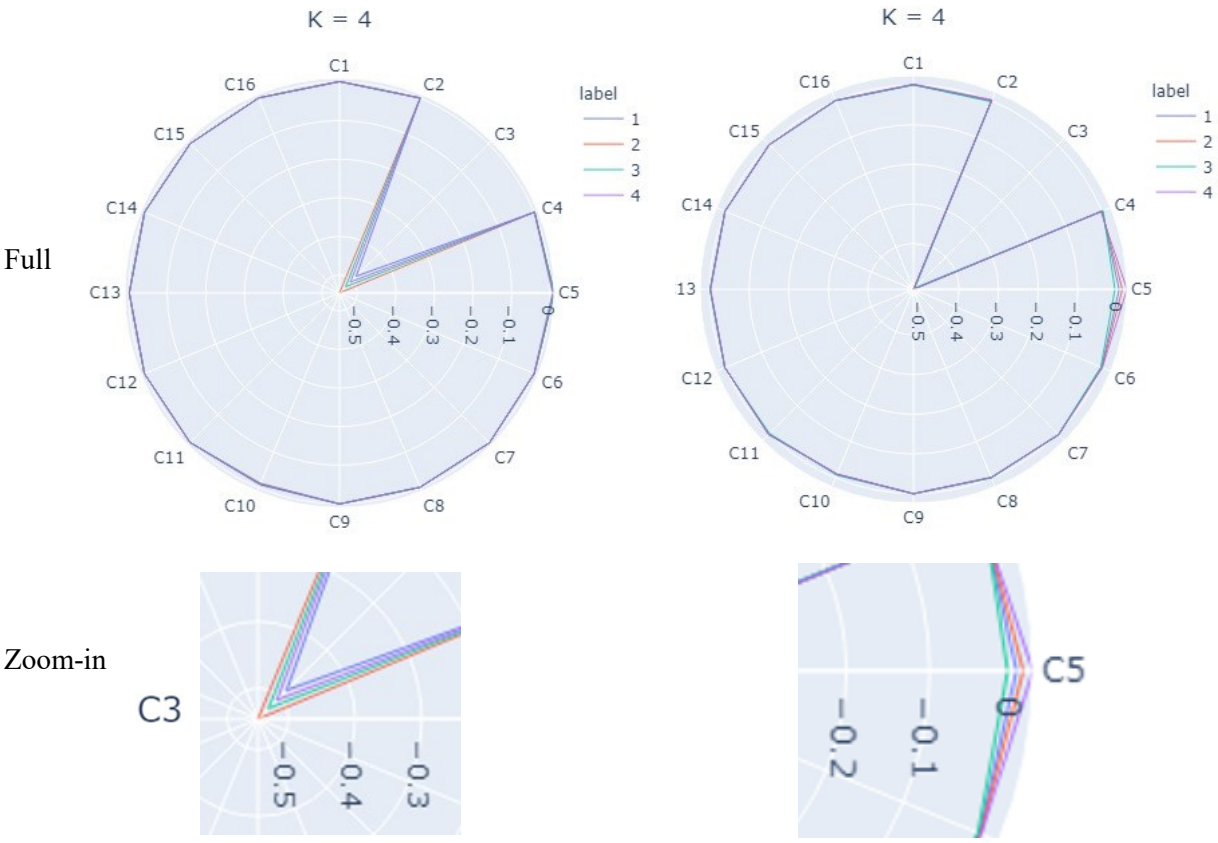


FIGURE 4.2: (a) Coefficient polar chart based on 16 Zernike shape coefficients using k-means clustering with $k = 4$ for natural surfaces (left) and normalized surfaces (right). The first row presents a full view of the polar chart. The second row presents a zoom-in view of the chart that focuses on the most discriminant Zernike coefficient.

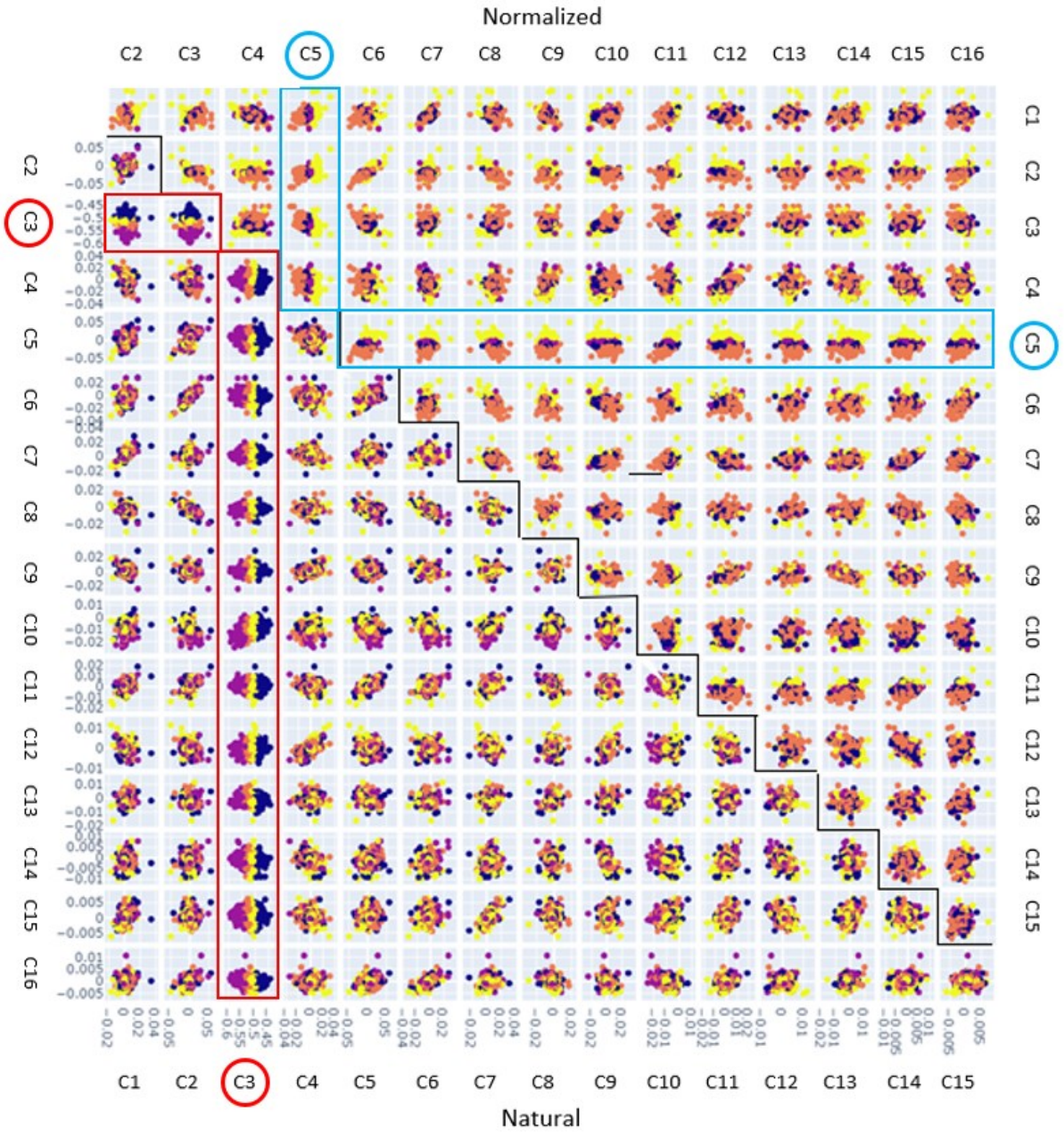


FIGURE 4.3: Series of pairwise coefficient scatter plots of the distribution of the 16 Zernike coefficients based on anterior OD corneal surfaces with $k = 4$ for (a) k-means clustering (complete plot series), (b) agglomerative clustering (excerpt) and (c) spectral clustering (excerpt).

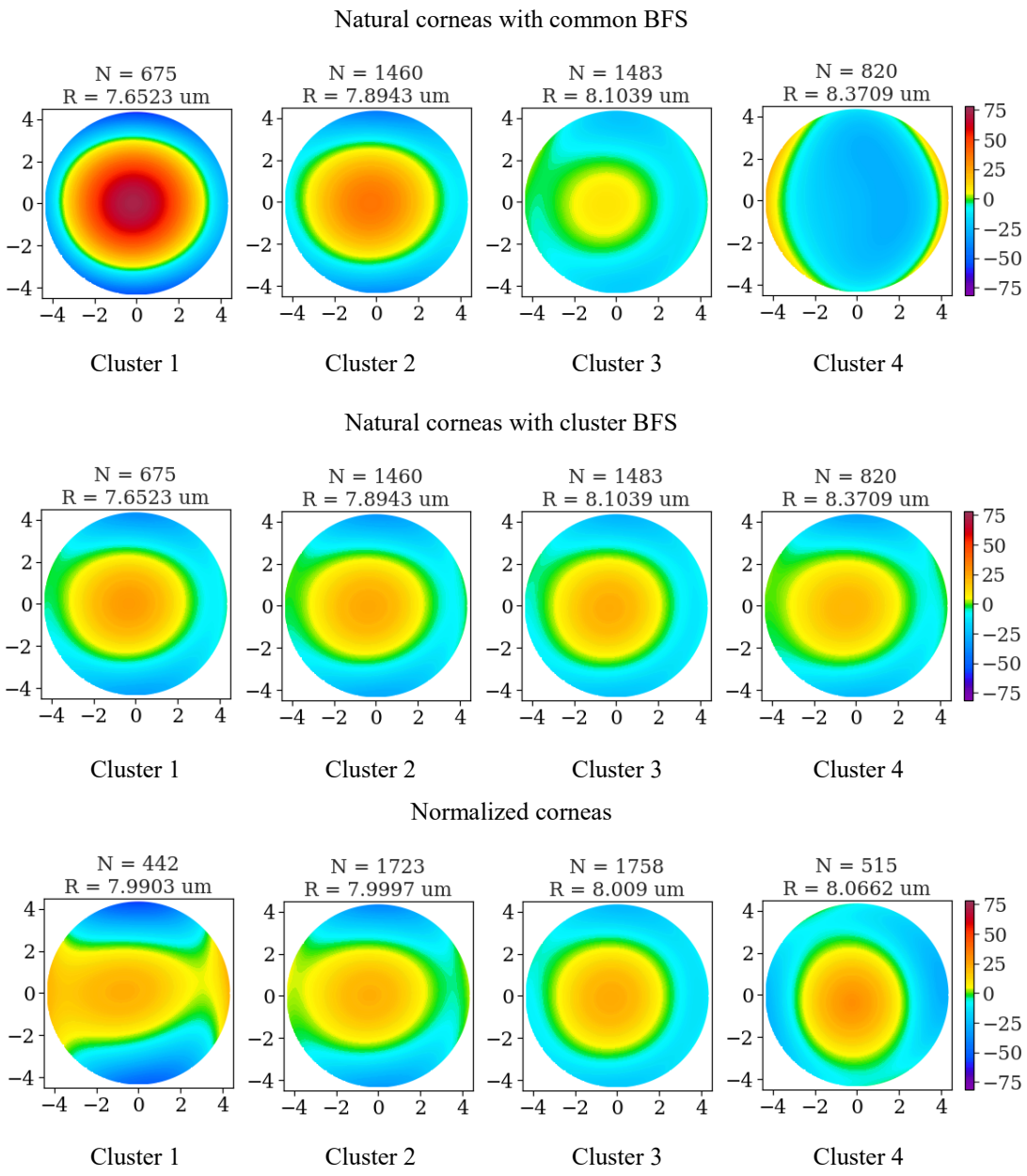


FIGURE 4.4: Average cluster elevation maps for k-means clustering applying to OD surfaces modeled with 16 Zernike terms with k = 4. In the first row, the clusters are based on natural surfaces and the maps are in reference to the common BFS. In the second row, the clusters are based on natural surfaces and the maps are in reference to their respective cluster BFS. In the third row, the clusters are based on normalized surfaces and the maps are in reference to the normalized BFS. The *X* and *Y* axes are in mm, and the *Z* axis (color scale) is in µm.

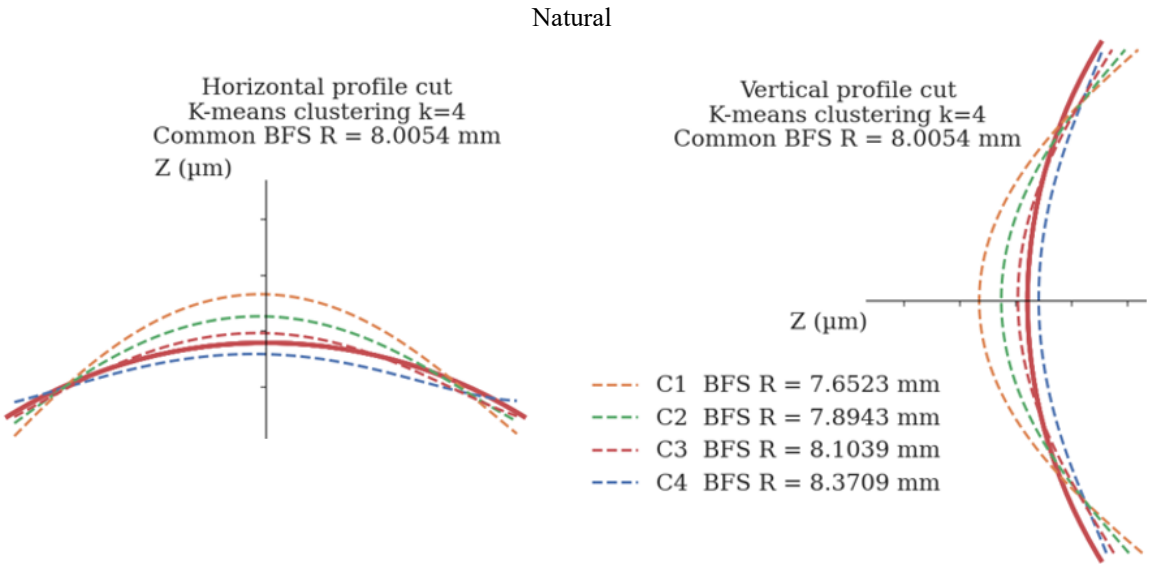


FIGURE 4.5: Average profile cuts along the vertical and horizontal meridians of natural OD mean corneal surfaces modeled with $J = 16$ shape Zernike coefficients using k-means clustering for $k = 4$. The solid curve is the common BFS. The differences of elevation between the mean cluster surfaces and the common BFS and the standard deviations (in grey) are amplified 10 times for a better visualization.

### *4.3.4. Cluster comparisons on corneal features*

As seen above, the unsupervised classification of corneal surfaces produced by k-means clustering is related to the Zernike coefficient of defocus ($Z_2^0$) for natural surfaces, and to the Zernike coefficient of vertical astigmatism ($Z_2^2$) for normalized surfaces. The coefficient of defocus relates the corneal curvature, known to be associated with some of the clinical features available in our database, namely the radius of the mean cluster BFS (R) [3], the white-to-white diameter (WTW) [7], the gender [3,11,14,19], and to a lesser extent the spherical equivalent (SE) [12, 13]. As for the coefficient of vertical astigmatism, it is known to be associated with the corneal Axis [15], and secondarily with age in older groups [15]–[18,24]. Therefore, we would expect that the clusters of natural surfaces be associated with R, WTW, gender and SE, and the clusters of normalized surfaces to Axis. As shown in Table 4.1, this is the case: the mean values of clusters on these variables increase or decreases progressively from one to another in agreement with expectations.[7] Each of these effects achieve significance at $p < 0.0001$.

[7] For Gender, the score is the average of the 1 values assigned to females and the 0 values assigned to males, so the higher the mean gender score for a cluster, the higher the proportion of females in the cluster.

Table 4.1 : Effects of clustering methods on clinical variables

| Surface state | Clinical Feature | C1 | C2 | C3 | C4 |
|---|---|---|---|---|---|
| Natural | R* | 7.54 ± 0.11 | 7.80 ± 0.08 | 8.00 ± 0.09 | 8.28 ± 0.13 |
| | WTW* | 11.59 ± 0.37 | 11.75 ± 0.35 | 11.85 ± 0.35 | 11.96 ± 0.37 |
| | Gender* | 0.69 ± 0.46 | 0.55 ± 0.50 | 0.44 ± 0.50 | 0.33 ± 0.47 |
| | SE* | -3.98 ± 2.54 | -3.59 ± 2.36 | -3.08 ± 2.47 | -2.99 ± 2.47 |
| Normalized | Axis* | 12.84 ± 18.32 | 17.44 ± 22.92 | 35.67 ± 33.82 | 56.51 ± 33.45 |
| | Age* | 39.48 ± 9.98 | 38.45 ± 10.04 | 41.05 ± 12.17 | 48.01 ± 15.82 |

* $p < 0.0001$

## 4.4. Discussion

In previous studies, the unsupervised classification of corneal surfaces has mostly been performed to distinguish keratoconus corneas (or other types of irregular corneas) and normal corneas and/or to identify theory-based subtypes of keratoconus corneas [54]–[56]. In this study, we examined the data distribution of normal adult anterior corneal surfaces in an attempt to identify their natural groupings using the most effective clustering method identified for the task in pretests based on a number of complementary evaluation tools, including clustering scores, modeling coefficient representations, corneal surface representations and clinical feature comparisons. Zernike polynomials were used to reduce the dimensionality of natural or normalized corneal surfaces to only a few coefficients, and the tested clustering methods applied directly to these coefficients instead of the surface itself.

In pretests, a number of clustering methods were examined, including hard clustering methods to assign only one cluster per surface, which could be linear (k-means and agglomerative clustering) or nonlinear (spectral clustering) and soft clustering methods (Gaussian Mixture Models, or GMM). The surfaces clustered had their dimensionality reduced with geometrical modeling alone or in combination with feature extraction, which could be either linear (with PCA) or nonlinear (with t-distributed stochastic neighbor embedding, or t-SNE). It was found that the best clusters (those that are evaluated as the most clearly delimitated and interpretable) were produced when a hard linear clustering method (k-means or agglomerative clustering) was used, with or without linear feature extraction, regardless of whether corneal surfaces on which clustering applied were natural or normalized.[8] The effectiveness of linear clustering methods with or without linear feature extraction might be related to the fact that it applied on corneal surfaces that were linearly modeled, making the use of these linear clustering methods suitable and their results easily interpretable. Pretests showed that k-means and agglomerative clustering produced good clusters from $k = 2$ to $k = 4$, so we opted for $k = 4$ to gain definition. Geometrical modeling with Zernike polynomials supported the production of good clusters from $J = 12$ to $J = 22$ or so,[9] with or without linear feature extraction.

[8] More precisely, if the clustering method was nonlinear (spectral clustering) or used in combination with a nonlinear feature extraction method (t-SNE) to reduce further the dimensionality of the data, the clusters produced were not as neat and were harder to interpret (they were based on more than one clustering criterion and their separation was more irregular). The use of a linear feature extraction method (like PCA) did not perturb clustering, but it did not help either. Results were neater with geometrical modeling than without (using only a feature extraction method to reduce the dimensionality of the data). The soft clustering method tested (GMM) produced similar results to those produced with linear models, but again, not as neat. Among linear clustering methods, agglomerative clustering performed almost as well as k-means clustering.

[9] Below $J = 12$, clusters lacked accuracy. Beyond $J = 22$, overfitting issues started to emerge that could not be fixed by applying a feature extraction method. Clearly, the main clustering criteria are not among higher-order Zernike coefficients, so their introduction is not helpful to clustering as their may introduce noise.

Given this state of affairs, we opted for k-means applying to corneal surfaces modeled with $J$ = 16 without feature extraction (for the sake of procedural simplicity). As a compromise between the clear delimitation of clusters and their precision, we selected $k$ = 4 both for natural corneas and for normalized corneas.

As shown in the Results, we found that natural (non-normalized) corneas are clustered in accordance with $C_3$ (aka $Z_2^0$), the Zernike coefficient of defocus. Defocus, the extent to which the cornea is off-focus, is related to the corneal curvature, which is itself related to the corneal radius (larger corneas are flatter) and to the degree of departure of the cornea from the perfect sphere (eccentricity). If the effect of the BFS radius is canceled out by presenting the maps in reference to the cluster BFS (the BFS of each cluster) instead of the common BFS, the flattening effect is reduced, but it still exists, and it can only be attributed to a departure of the cornea from the perfect sphere that fits it best, the cluster BFS. A possible explanation to these observations is the following. When clustering applies to centered natural corneas, the most important varying feature is arguably the BFS radius. The latter is associated to the WTW [3], which is itself associated to the spherical equivalent [9], a form of defocus linked to a departure from the corneal curvature in focus. This departure from the focal curvature becomes visible when the powerful effect of the BFS radius on the curvature is cancelled out by presenting the maps in reference to the BFS of each cluster.

On the other hand, when clusters are produced on the basis of normalized corneal surfaces, in which the BFS radius is always about the same, the grouping can obviously not be based on the BFS radius. We found that the corneas are then grouped accordance with $C_5$ (aka $Z_2^2$), the Zernike coefficient of vertical astigmatism, which is associated with the corneal axis, itself related to age. Indeed, the curvature of the horizontal meridian increases progressively from one cluster to the other (and the opposite for the curvature of the vertical meridian), indicating a transition from "with the rule" to "against the rule" astigmatism. Axis is another fundamental feature of normal corneas, and astigmatism another basic aberration found in these corneas.

## 4.5. Conclusion

This study tried to identify the most discriminative clinical features for differentiating normal corneal surfaces and their data distribution. We found that the clusters based on natural corneal surfaces were grouped in accordance with $Z_2^0$ while those based on normalized surfaces (in which the corneal size is neutralized) were grouped according to $Z_2^2$. $Z_2^0$ and $Z_2^2$ are low-order Zernike coefficients that relate to two fundamental features of the normal cornea: its curvature and its axis. And they represent the two most important types of aberrations that can be found in normal corneas: defocus and astigmatism.

In the future, we intend to apply the methodology developed here to other dimensions of the cornea (the posterior surface and the inter-surface volume) and to irregular types of corneas (keratonus, Fuch, etc.). Other types of geometric models and feature extraction methods will also be tested.

## Acknowledgements

This work was supported by the QVRN (Quebec Vision Research Network), the FRQNT (Fonds de recherche du Québec Nature et Technologie) and the MUTAN (University Mission of Tunisia in North America).

# CHAPTER 5: PREDICTING THE SHAPE OF CORNEAS FROM CLINICAL DATA WITH MACHINE LEARNING MODELS

Hala Bouazizi[1], Isabelle Brunette[2,3], Jean Meunier [1,2]

1 Department of Computer Science and Operations Research, University of Montreal, Montreal, Quebec, Canada
2 Department of Ophthalmology, University of Montreal, Montreal, Quebec, Canada
3 Maisonneuve-Rosemont Hospital Research Center, Montreal, Quebec, Canada

## Abstract

In ophthalmology, there is a need to explore the relationships between clinical parameters and the corneal shape. The present study explores the paradigm of machine learning (ML) and nonlinear regression methods to identify the conditions in which predictions of corneal shapes from clinical data can effectively be made for a population of corneas to visualize their central tendencies. To this end, the dimensionality of a database of topographic matrices of elevations representing the anterior corneal surfaces of normal adult corneas was first reduced by Zernike modeling into short vectors of coefficients. The nonlinear regression methods examined from the scikit-learn library were gradient boosting, Gaussian process, kernel ridge, random forest, k-nearest neighbors, AdaBoost, bagging, and multilayer perceptron. Different sets of clinical variables were used as predictors, including geometric variables (best-fit sphere radius, eye side, white-to-white distance, anterior chamber depth), refraction variables (sphere, cylinder, axis) and demographic variables (age, gender). The targets were vectors of Zernike coefficients of different lengths (from 12 to 20, initial mean shape coefficient excluded). Based on RMSE scores measuring the distance between raw (non-modeled) topographic true surfaces and predicted surfaces, the best model (method + predictors + targets) was gradient boosting using all available clinical variables to predict 16 Zernike coefficients. The most explicative predictor was the BFS radius, followed by the eye side and by refractive parameters. The aptitude of this model to accurately predict the central tendencies of the clinical variables used as predictors was further visually assessed thanks to an atlas of true and predicted average elevation maps. The great similarity of color patterns between the true and predicted average surfaces represented in these maps for different clinical variables showed that it is possible to effectively predict the shape of the cornea from a set of clinical variables and visualize their central tendencies.

**Keywords:** cornea, regression, machine learning, gradient boosting, Gaussian process, Zernike, corneal topography, average elevation map

## 5.1. Introduction

The cornea is the clear front surface of the eye, and it contributes to approximately 65 to 75 percent of the refractive power of the eye. Several factors are known to influence the corneal shape, including geometric features such as the axial length, the best-fit sphere, the anterior chamber depth and the white-to-white distance; refraction features such as the spherical equivalence, the axis, and the cylinder; and demographic features such as the age, the sex, the race and the ethnicity [3,15]. Given these known relations, is it possible to predict the shape of the cornea based on clinical data? To address this issue, we need to take advantage of the complex relationship that holds between clinical data and the corneal shape.

In the clinical literature, the traditional approach adopted to investigate this relationship is essentially statistical and requires prior knowledge of the form of this relationship (linear or not), which is not that well known and depends on prior knowledge of the features being related. In the machine learning (ML) paradigm, it is not necessary to have such prior knowledge, as the form of the relationship can be discovered by training models. The ultimate goal sought under that paradigm is not solely to establish whether a relationship exists but also to determine the closest one by systematically exploring all applicable conditions in which model optimization can take place, and to make maximally accurate predictions on this basis. While this necessitates a large amount of data, big databases become increasingly available, and an increasing number of ML studies dealing with corneal shape have been conducted in recent years. The vast majority of them are aimed at providing support for clinical diagnosis, and to this end, classification tasks are usually performed (as opposed to regression tasks). In corneal classification, the corneal data come in the form of clinical parameters (demographic, structural, refractive features of the cornea) or in the form of images (corneal surface elevations or inter-surface pachymetry visualized as color-coded maps, or topographies) [58]. Most often, these corneal data need to undergo a preprocessing step of dimensionality reduction that can take place by feature extraction, geometric modeling or data weighing. This is the case in Espinosa et al. [59], where the Gaussian process algorithm applies to the anterior corneal surface (modeled with Zernike coefficients) and to keratometry measures (weighted with neighborhood component analysis) in an attempt to predict the subjective refraction of the cornea. Likewise, in Lavric et al. [60], bagged trees classifiers are applied to corneal structural parameters along with corneal images (obtained by topography, pachymetry and optical coherence tomography) to predict visual field damage (as measured by the extent to which visual field departs from normal visual field parameters). The dimensionality of predictors is reduced by feature subset selection (greedy hill climbing step). In Kamiya et al. [61], a deep learning algorithm (CNN) takes color-coded maps of the anterior and posterior elevations to distinguish normal corneas from keratoconus corneas of different types. While the above studies proceed in a supervised manner to achieve corneal classification, it is also possible to proceed without supervision by applying a clustering algorithm. The input data are then quite similar to those used as predictors in supervised classification (clinical parameters of the cornea, as in Yousefi *et al.*, [54] and in Hallett et al. [55], or topographic maps of the cornea, as in Zéboulon et al. [56] and Bouazizi [14]). Again, the data undergo a process of dimensionality reduction by feature extraction [54,55,56] or by geometric modeling [14] before the ML process can take place.

In the present study, the perspective is different. Instead of resorting to ML algorithms to establish a diagnosis of the cornea from clinical parameters or from images of the cornea, it starts from clinical parameters in an attempt to predict the corneal shape itself, with a focus on the anterior corneal surface, which is the main responsible for the refractive power of the cornea. To facilitate corneal surface prediction, the dimensionality of the dataset of elevations is reduced by geometric modeling (Zernike polynomials). The main issue investigated in this study is to verify to what extent the whole shape of anterior corneal surfaces can be accurately predicted based on a set of clinical parameters for a normal adult population using an ML regression approach, If so, an atlas

of average elevation maps used to visualize the effects of corneal parameters on the shape of the predicted corneal surfaces should be similar to an atlas used to visualize the effects on the shape of corresponding true surfaces.

For this exploratory study, we needed a regression method that can be applied robustly in a limited optimization space to a medium-size database. To this end, we focused on standard ML algorithms and tested each of the applicable methods of the scikit-learn library with the database of anterior corneal surfaces under study. The database includes different clinical variables (the predictors) associated with corneal surfaces represented as topographic data in the form of large matrices of elevations (the targets). To preprocess the data, the clinical variables acting as predictors were normalized. As for the associated topographic corneal surfaces acting as targets, they had their large dimensionality reduced by geometric modeling based on Zernike polynomials with different numbers of coefficients to identify the best number. Defining a regression model as a triplet that includes a set of clinical variables acting as predictors, a regression method, and a vector of Zernike coefficients of a given size acting as targets, the goal was to identify the best model and to verify whether and to what extent the predicted surfaces produced by this model agreed with the true surfaces, as verified both quantitatively with RMSE scores and qualitatively with average elevation maps.

## 5.2. Method

### *5.2.1. Data processing*

*Data acquisition*

The database was collected using the Orbscan II corneal topographer (Bausch and Lomb, Rochester, NY). It consists of 8594 topographies of anterior surfaces of normal corneas (4356 male corneas and 4238 female corneas, 4430 OD (right) corneas and 4164 OS (left) corneas), coming from 4941 consenting adult subjects with no history of ocular diseases, ocular surgery, or recent contact lens wear and no repetition (only one acquisition per eye).[10] Each topography was recorded as a 101×101 grid of elevations (heights) evenly spaced (every 0.1 mm) along the x (left-right) and y (up-down) axes and saved as a vector of 10201 elevations. It was associated with a number of clinical parameters produced by the topographer, including geometric parameters (side (OD and OS), white-to-white distance, and anterior chamber depth), refraction parameters (refractive sphere, cylinder, axis), and demographic parameters (age, gender). The experimental procedures involving human subjects described in this paper were approved by the Institutional Review Board.

*Data preprocessing*

*Predictors*. Predictors with real values were normalized in the [0, 1] range. Axis needed a special treatment because it is a circular variable expressed on a semi-circle (from $0^{o}$ to $180^{o}$). This involved multiplying Axis degrees by 2 (to extend their range to the full circle) and computing their sines and cosines.

*Targets.* Most of the missing/noisy data are found in the periphery of corneal surface topographies due to acquisition artefacts (eyelid, lash or nose occlusion during scanning). A fringe of 5 mm was accordingly removed from the original 101×101 matrix of elevations of each surface to get a reduced 91×91 matrix. The dimensionality of this smaller matrix was then reduced to a much shorter vector of Zernike coefficients. To this end, the corneal surface was modeled as a sum of least-squared fitted Zernike polynomials over the unit disk, as described in Equation 5.1:

[10] We had access to more good quality data for anterior corneal surfaces with the Orbscan II than with the more recent Pentacam, an important consideration for a corneal regression study.

$$S(\rho_w, \theta_w) = z_w = \sum_{g=1}^{G} C_g P_g(\rho_w, \theta_w) + \epsilon_w \quad \textit{for } w = 1, 2, \ldots, W \tag{5.1}$$

The corneal surface $S$ consists of a set of $W$ elevations $S(\rho_w, \theta_w)$ located at polar coordinates $\rho_w$ and $\theta_w$ for $w = 1$ to $W$. Each elevation $S(\rho_w, \theta_w)$ (or equivalently $z_w$) is modeled by summing the product of the $g^{th}$ Zernike polynomial $P_g(\rho_w, \theta_w)$ and the $g^{th}$ coefficient $C_g$ for $g = 1$ to $G$, assuming error $\epsilon_w$. In this study, the $G$ Zernike polynomials were ordered in accordance with Noll sequential indices. The coefficient of the first polynomial ($C_1$) represents the mean height of the cornea, contrary to the following coefficients, which account for different aspects of the corneal shape. Being irrelevant and adding unnecessary noise to corneal shape predictions [28], it was removed from the dataset, leaving for the modeling of the corneal surface only the $J$ (= $G$ – 1) remaining shape coefficients. More on the Zernike modeling of corneal surfaces can be found in [57].

### *5.2.2. Regression analysis*

A regression analysis was conducted for each *regression model*, defined as a selection of a regression method, a set of predictors and a vector of shape Zernike coefficients of size $J$.

*Regression methods*

Taken from the scikit-learn library, the regression *methods* investigated included different nonparametric methods, namely bagging (BG), k-nearest neighbors (KNN), random forest (RF), kernel ridge (KR), gradient boosting (GB), Gaussian process (GP) and multilayer perceptron (MLP) [40]. These methods, presented in Table 5.1, were compared to two reference methods used to establish a minimum standard of performance (lower bound). The first one is the baseline (BL); this simply corresponds to the average shape of all corneas. It is used to assess the amount of specific learning achieved by the nonparametric methods, that is, the ability of the model to perform better than a common prediction that applies indistinctively to all surfaces. The second reference method is linear regression (LR), which is the simplest regression model able to achieve specific learning. It is used to assess the nonlinear contribution of the nonparametric methods being tested.

Nonparametric methods rest on no assumption about data distribution. Table 5.1 classifies those that were tested in accordance with their *architecture* and *algorithm*. The *architecture* could be (1) a *single estimator*, (2) an *ensemble* (unstructured collection of "weak" methods, such as decision trees, whose outputs are processed by an integration function), or (3) a *neural network* (with input, output and hidden ordered layers). Different *algorithms* could be used: (a) *ridge regression* (a linear function is learned in the space induced by kernel-transformed data); (b) a *probabilistic function* (a stochastic algorithm is applied with respect to probability theory); (c) *nearest neighbor selection* (the observations of the training set that are the closest to the tested observation are selected for testing); (d) *bagging* (weak methods are applied independently to different subsets of the data and are assigned equal weights when integrated); (e) *boosting* (weak methods are applied sequentially in the same dataset and are assigned unequal fitted weights when integrated); and (f) multilayer propagation (the data flow forward across layers and are nonlinearly modulated before being retroactively adjusted by gradient descent). For more details, see [40].

TABLE 5.1: Tested scikit-learn nonparametric methods for multiple multivariate regression tasks.

| Method | Architecture | Algorithm Type | Specificity |
|---|---|---|---|
| Kernel ridge (KR) | Single estimator | Ridge regression | Kernel trick |
| Gaussian process (GP) | Single estimator | Probabilistic function | Gaussian equations |
| K-nearest neighbors (KNN) | Single estimator | Nearest neighbor selection | Selection of *k* nearest neighbors |
| Random forest (RF) | Ensemble of decision trees | Bagging | Random selection of feature subsets |
| Bagging (BG) | Ensemble of decision trees | Bagging | Grid search selection of feature subsets |
| AdaBoost (AB) | Sequence of decision trees | Boosting | Iterative majority vote |
| Gradient boosting (GB) | Sequence of decision trees | Boosting | Gradient descent |
| Multi-layer perceptron (MLP) | Neural network structure | Multilayer propagation | Hidden layers, back-propagation, gradient descent, |

*Predictors*

Each regression method was initially tested in the exploratory step of the study with all possible combinations of the examined clinical variables used as predictors, including (with their two-letter acronyms): (1) BFS (Bf), to specify the radius of the best-adjusted sphere (BFS) of the cornea, (2) White-to-white distance (Ww, aka horizontal corneal diameter), to specify the limbus to limbus distance, (3) Anterior chamber depth (Ad), to specify the depth of the corneal chamber, (4) Side (Si), to specify left or right eye, (5) Sphere (Sp), to specify the lens power needed to correct vision from nearsightedness or farsightedness, (6) Cylinder (Cy), to specify the lens power to correct astigmatism, (7) Sinus (2 x Axis) (Sn) and Cosinus (2 x Axis) (Co), to specify the angle of the axis of astigmatism. The 512 possible sets of predictors were tested in the exploratory step, and the 10 best of them were selected for the validation step (see below), (8) Age (Ag), and (9) Gender (Ge).

*Targets*

Each regression method was applied to vectors of Zernike shape coefficients of different lengths (*J*). Preliminary tests indicated that to be optimal, *J* should range somewhere between 12 and 20 coefficients, so the analyses were conducted for $J = 12, 14, 16, 18, 20$.

*Regression models*

Figure 5.2 summarizes the conditions in which the regression analyses were conducted. Each possible set of conditions defines a *regression model* to be tested. This involved running a test for each of the 25600 models that can be formed (10 regression methods × 512 sets of predictors × 5 vector lengths of shape coefficients for each corneal surface). In running systematically all possible models, considering that this is the first study on this issue, we wanted to set a reference for further studies in which more effective predictor reduction methods are likely to be used. Computer clusters from the Digital Research Alliance of Canada made possible to go through this important load of processing in a reasonable time.

TABLE 5.2: Tested regression models.

| Condition | Description | Possible values |
|---|---|---|
| Regression method | Reference or nonparametric method | Reference method: BL, LR<br>Nonparametric method: AB, BG, KNN, RF, KR, GB, GP, MLP |
| Predictors | Set of clinical variables | Set from the power set of {Ag, Ge, Si, Ww, Sn, Co, Cy, Sp, Ad} |
| Targets | Set of *J* shape coefficients | $J = 12, 14, 16, 18, 20$ |

*Optimization of regression models*

To optimize the *parameters* of each tested regression model (selected method, set of predictors and array of target coefficients), a pipeline involving a random search (to get a rough approximation of the optimal model parameters) followed by a grid search (fine tuning to obtain more accurate estimations of optimal parameters) was applied [40]. In each case, the fitting measure $R^2$ on the training set was adopted to determine the best set of parameters for each model. The random search was based on the scikit-learn RandomizedSearchCV algorithm and the grid search on the GridSearchCV algorithm. Both the RandomSearchCV and GridSearchCV algorithms applied k-fold cross-validation with $k = 5$ (by default). The score obtained by combining these two search modalities was better and faster than with random search or grid search alone.

*Identification of the best regression model*

The determination of the best regression model involved a step of exploration and a step of validation.

In the *exploratory step*, all the 25600 possible regression models were tested. To make these tests possible, a fast analysis procedure was used aimed to narrow down the modeling space to only the most promising models, to be tested more completely in the next validating step. This fast preliminary procedure was based on an incomplete 10-fold cross-validation procedure in which only 2 folds were actually processed, each of which being split in a 9 to 10 proportion to get the training and testing sets, as for standard 10-fold cross-validation. Based on the RMSE scores obtained, the exploratory step allowed us to identify for each number of coefficient $J$ the regression methods that performed better than LR (the linear standard of reference), and for each of them, the 10 best sets of predictors identified. The RMSE scores measured the distance between the predicted modeled surfaces and the raw topographic true surfaces. Only the available elevation data points were considered to compute the scores, to the exclusion of the few missing data points of the 91×91 matrix of elevations (holes of the raw surface topography). The predicted and raw surfaces were previously vertically aligned to reduce the residual volume between them [29]. The most promising models to be kept for the full validation involved the methods that performed better than linear regression (the best methods), for each of them the 10 best sets of clinical variables (the best sets of predictors), and for each of these possibilities, the vectors of coefficients of length 12 to 20 (the best sets of targets).

In the *validation step*, the selected models were validated using a standard 10-fold cross validation procedure (again in a 9/10 proportion) to gain accuracy and generalizability (in combination with the k-fold cross-validation applied to fit coefficients at each dataset split, an effect of nested cross-validation was therefore achieved). The best regression model was the one with the best mean RMSE scores (estimated as in the exploratory step) across the 10 cross-validation folds.

*Evaluation of the best regression model*

Once identified, the best model was evaluated as to its predictions and its predictors.

*Evaluation of predictions.* In addition to be evaluated quantitatively with an *RMSE score* as described above, the best modeled was evaluated qualitatively based on *average elevation map analysis*, by which the effects produced by different clinical variables on the predicted surfaces (essentially, those used as predictors) can be visualized. By verifying whether the average elevation maps of predicted surfaces are similar to those of the corresponding true surfaces for different clinical variables, and by checking whether the effects displayed in these maps are consistent with the clinical literature on the anterior cornea, one can assess the extent to which the predictions are clinically valid.

In ophthalmology, the corneal surface is usually represented in reference to a sphere since the corneal surface is nearly spherical (see Figure 5.1 (a)). The differences between the corneal surface and the sphere of reference (the sphere that best fits the surface, or BFS, for Best-Fit Sphere) are

often tiny, so ophthalmologists often use elevation maps in which these differences are magnified with a color map. The positive differences, corresponding to areas of the corneal surface above the BFS, are represented with warm colors; the negative differences, corresponding to areas below the BFS, are represented with cold colors; those directly on the BFS are in green. In Figure 5.1 (b), a *simple elevation map* is presented in which the OD anterior surface of a single cornea is represented in reference to its BFS. In Figure 5.1 (b), the same surface is represented after it has been modeled with Zernike coefficients to reduce its dimensionality. Finally, in Figure 5.1 (d), an *average elevation map* of a particular group of surfaces (surfaces whose anterior chamber depth is between 1.96 to 3.11 mm) is represented as an average surface in reference to an average BFS (Figure 5.1 (c)). The *average surface* of a group of surfaces can be obtained by averaging their Zernike coefficients and by reconstructing that surface based on the mean coefficients [14]. The *BFS* used here is the *common BFS*, obtained by averaging the mean BFS of each group of surfaces being compared. The common BFS is useful to highlight the differences in shape between groups of surfaces.

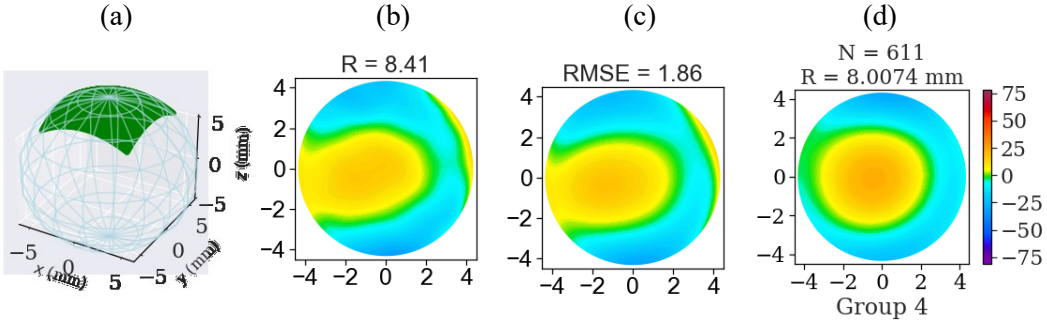


FIGURE 5.1: (a) 3D map of a single OD anterior corneal surface in reference to its BFS (surface in green, BFS as a grid; (b) Raw elevation map of the same surface in reference to its BFS, (c) Modeled elevation map of the same surface with 24 Zernike coefficients, (d) Average elevation map of a group of corneal surfaces (age group from 50 to 60 yo) modeled with 16 Zernike coefficients. Warm colors are for surface areas above the BFS, cold colors for those below the BFS, and green colors for those on the BFS. The *X* and *Y* axes are in mm, and the *Z* axis (color scale) is in µm.

An atlas of average elevation maps was constructed for a number of clinical variables to assess the similarity of true and predicted corneal surfaces (see Figure 5.4). These clinical variables were categorical versions of those used as predictors in regression analyses (they were segmented in groups when needed). They include geometric variables: best-fit sphere (Bf), white-to-white (Ww), anterior chamber depth (Ad) and side (Si), as well as refraction variables: astigmatism (As) and ametropia (Am), and demographic variables: age (Ag) and gender (Ge). These variables were grouped as follows:

(1) Bf (group 1: from 7.06 to 7.63 mm, group 2: from 7.63 to 8.19 mm, group 3: from 8.19 to 8.99 mm),

(2) Ww (group 1: from 10.40 to 11.36 mm, group 2: from 11.36 to 12.32 mm, group 3: from 12.32 to 14.10 mm),

(3) Ad (group 1: from 1.96 to 3.11 mm, group 2: from 3.11 to 4.26 mm, group 3: from 4.26 to 6.92 mm),

(4) Si (group 1: OD, group 2: OS),

(5) Am (group 1: moderate or high myopia, SE < -3 D, group 2: emmetropia or low ametropia: -3 D ≥ SE ≤ 3 D, group 3: moderate or high hyperopia: SE > 3 D),

(6) As (1: group 1: “with the rule”: the axis is between 0° and 30° or between 150° and 180°, 2: group 2: oblique: the axis is between 30° and 60° or between 120° and 150°, group 3: “against the rule”: the axis is between 60° and 90° or between 90° and 120°),

(7) Ag (group 1: from 20 to 29 yo, group 2: from 30 to 39 yo, group 3: from 40 to 49 yo, group 4: from 50 to 59 yo, group 5: from 60 to 70 yo, group 6: 70 yo and more),

(8) Ge (group 1: M, group 2: F).

*Evaluation of predictors.* Once the best model is identified, it remains to see to what extent the clinical variables used as predictors in this model contributes to the predictions. This issue was addressed in two complementary ways: by considering their occurrences and their non-occurrences in the sets of predictors. With regard to their *occurrences*, it was assumed that the more a clinical variable occurs frequently in the 10 best sets of predictors for the best method and the best *J*, the more it is important as a predictor for the accuracy of predictions. With regard to their *non-occurrences*, it was instead assumed that the more the accuracy loss of a clinical variable is important when it fails to occur for the first time in the list of set of predictors (ranked by RMSE score), the more this variable is important as a predictor to make accurate predictions. The accuracy loss of a clinical variable was computed as the difference between the RMSE score of the best model (the model with the best method, *J* value and set of predictors) and the RMSE score of the best similar model (the model with the same regression method and *J* value but not the same set of predictors) where this clinical variable is absent from the set of predictors. To make possible the evaluation of predictors in a reasonable time, only two folds of the shuffled dataset were used (instead of the 10 folds that would be required for full 10-fold cross-validation).

## 5.3. Results

### *5.3.1. Identification of the best regression model*

*Exploratory step.* In the exploratory step, all regression methods were tested with all 512 possible sets of clinical variables acting as predictors on each vector of *J* Zernike coefficients acting as targets in an attempt to reduce the modeling space for further validation. Among the tested regression methods, four did better than linear regression (LR) and were accordingly selected for further testing in the validation step of the study, namely GB, GP, KR and RF along with the reference methods (BL and LR).

*Validation step.* Figure 5.2 (left) plots the mean RMSE of each of the validated regression methods with their best set of predictors for each *J*.

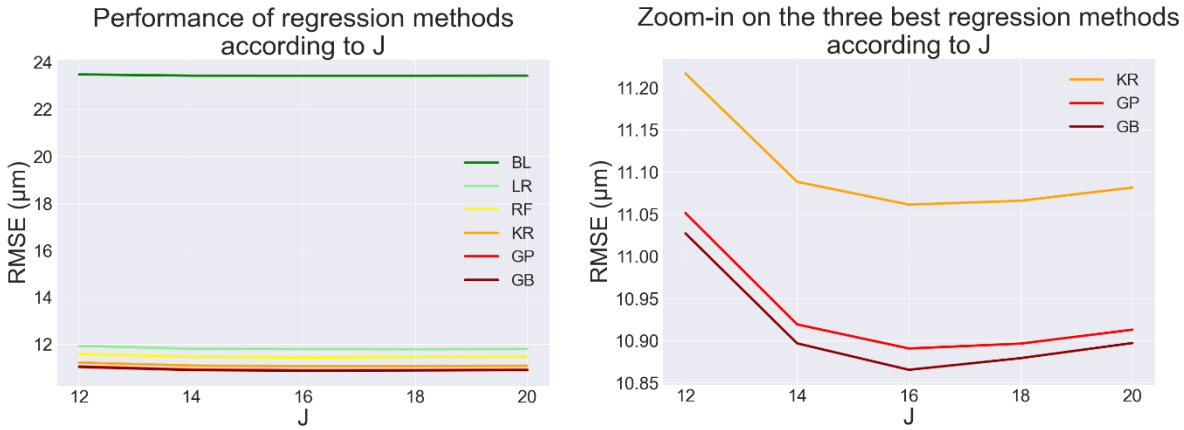


FIGURE 5.2: RMSE curves of the validated regression methods with their best set of predictors of each *J* (left) and zoom-in view on the curves of the three best methods (right).

As can be seen in Figure 5.2 (left), the three best methods are, in order, GB, GP and KR. These three methods perform significantly better than LR on every *J* and much better than BL. With a score of RMSE = 10.87 µm, the best selection of method, predictors and targets (the best model) was GB using 16 coefficients and all available clinical variables as predictors (GB 16 all), closely

followed by GP using 16 coefficients and all available clinical variables but Ge (GB 16 all\Ge, RMSE = 10.88 µm) (see Figure 5.2, right).

### *5.3.2. Contribution of the best model's predictors to the predictions*

To evaluate the contribution of the clinical variables used as predictors in the best model (GB 16 all) in predicting corneal surfaces, their occurrences and non-occurrences in the best model and models of the same family (in which the regression method and number of coefficients are the same but the sets of predictors are different) were considered.

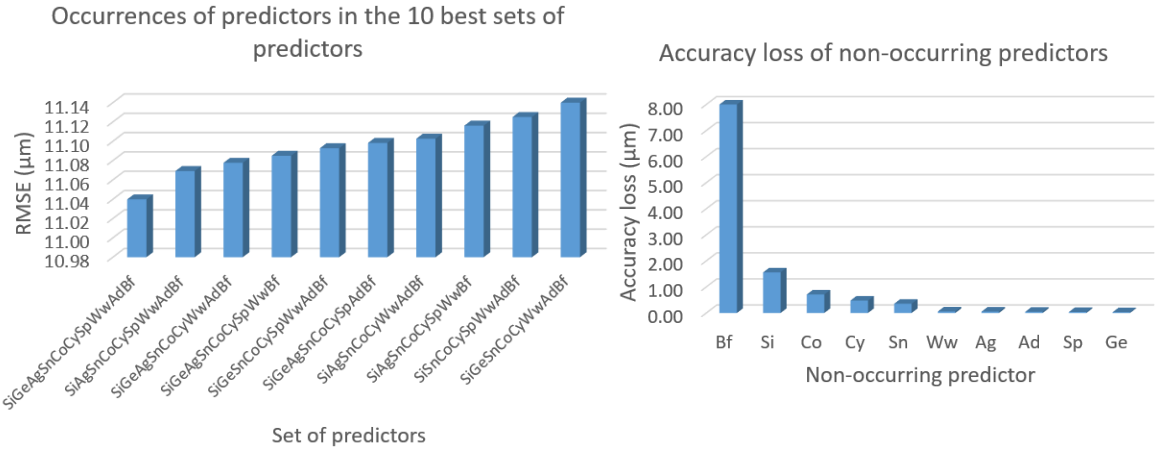


FIGURE 5.3: Occurrences of the predictors in the 10 best sets of predictors according to the RMSE (left) and accuracy loss of predictors when they fail to occur for the first time in a set of predictors (ranked by increasing RMSE scores).

*Occurrences of clinical variables as predictors.*

Figure 5.3 (left) shows the occurrences of the clinical variables in the 10 best sets of predictors ranked according to their RMSE. In Table 5.3, the predictors are ranked by frequency of occurrence. As can be seen, a group of variables appears in each the 10 best sets, namely Bf, Si, Co, Cy and Sn. Then, in decreasing order, we have Ww (9 times), Ad (8 times), Ag and Sp (7 times), and Ge (6 times).

TABLE 5.3: Frequencies of occurrences of clinical variables in the 10 best sets of predictors.

| Variable | Frequency | Type |
|---|---|---|
| Bf | 10 | Corneal shape |
| Si | 10 | Corneal shape |
| Co | 10 | Refraction |
| Cy | 10 | Refraction |
| Sn | 10 | Refraction |
| Ww | 9 | Corneal shape |
| Ad | 8 | Corneal shape |
| Ag | 7 | Demographic |
| Sp | 7 | Refraction |
| Ge | 6 | Demographic |

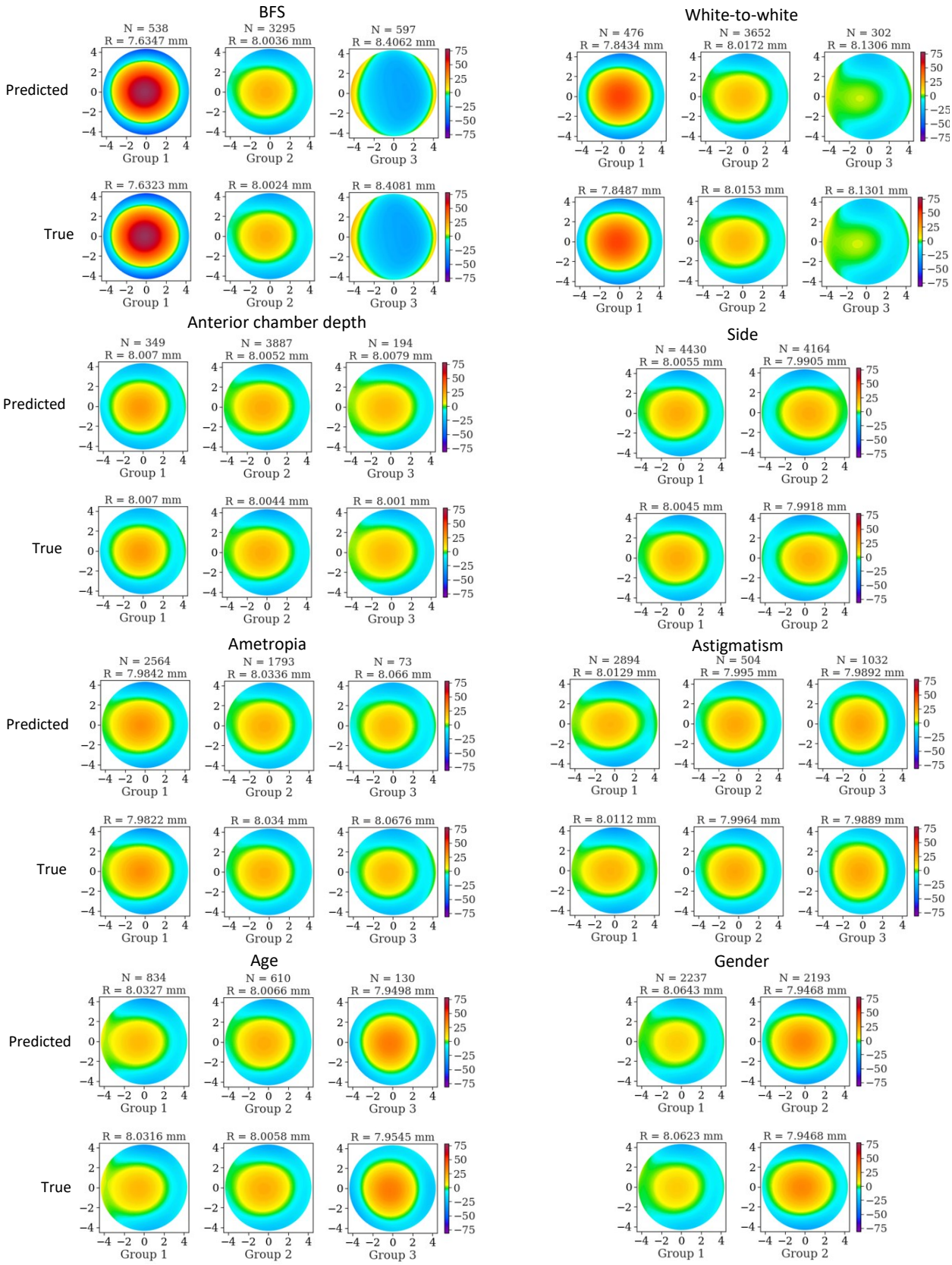


FIGURE 5.4: Atlas of average elevation maps of predicted (first row) and true (second row) OD anterior surfaces for different clinical variables modeled with 16 Zernike coefficients. The X and Y axes are in mm, and the Z axis (color scale) is in µm. N is the number of surface of a group. R is the radius of the mean BFS of the group.

*Non-occurrences of clinical variables as predictors.* In Figure 5.3 (right), clinical variables are ranked in accordance with the importance of their accuracy loss when they fail to occur for the first time in a set of predictors of a model of the GB 16 family (ranked by increasing RMSE scores). As can be seen, four predictors are associated with a noticeable accuracy loss: Bf, Si, Co and Sn (the same that appeared in each of the 10 best sets of predictors). Among them, Bf stands out for the considerable importance of its accuracy loss when it is absent for the first time in a set of predictors: a drop of 8.00 µm (from 19.04 µm to 11.04 µm). The loss incurred by Si, Co and Sn is less important (0.78 µm on average) but still significant. The loss incurred by Ww, Ag, Ad, Sp, Ge is marginal (0.044 µm on average).

### *5.3.3. Visualization of the predictions of the best regression model*

Figure 5.4 presents the true and predicted average elevation maps of Zernike modeled surfaces for different clinical variables, including geometric variables (Bf, Si, Ww, Ad), refraction variables (Am, As), and demographic variables (Ag, Ge), along with a description of their groups. The maps are in reference to the common BFS. For each variable, the average predicted surfaces (one for each group of the variable), produced with GB and modeled with 16 Zernike terms, are presented on the first row, and the corresponding true surfaces, also modeled with 16 Zernike terms, in the second row. As can be seen, the similarity of the predicted and true maps is excellent for every clinical variable. Difference maps representing the difference of elevations between predicted and true surfaces (not shown) would all be green using the same colorbar. Similar results were obtained with OS surfaces (maps not shown).

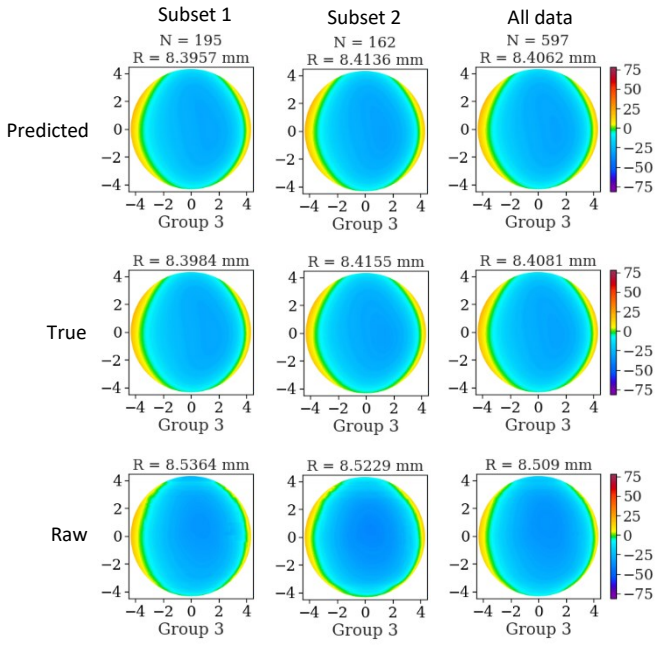


FIGURE 5.5: Average elevation maps of the predicted (first row), true (second row) and raw (third row) OD anterior corneal surfaces of the third BFS group based on two subsets of the whole dataset (the two first column) and on the whole dataset (third column). The maps are in reference to the common BFS. The X and Y axes are in mm, and the Z axis (color scale) is in µm. N is the number of surface of a group. R is the radius of the mean BFS of the group.

To assess the generalizability and robustness of predictions, predictions were also made with different sets of data. As an illustration, Figure 5.5 presents the average elevation maps of the third BFS group for raw surfaces, as scanned by the topographer (first row, missing data are not interpolated), for true surfaces modeled with 16 Zernike coefficients (second row) and for predicted

surfaces also modeled with 16 Zernike coefficients (third row). The first column is based on the training data of the first three folds, the second column on the training data of the next three folds, and the third column on all data. As can be seen, even with data that are different and more limited in number, the average elevation maps of raw, modeled and predicted corneal surfaces are much similar to one another.

## 5.4. Discussion

This study aimed to explore whether it is possible to predict the shape of the corneal surface based on different clinical variables and visualize their central tendencies. To this end, we had to select the best regression model among those examined, which involved the selection of a method (AB, BG, KNN, RF, KR, GB, GP, MLP), a set of predictors (Bf, Ww, Ad, Si, Sp, Cy, Co, Sn, Ag, Ge) and a set of targets formed of a vector of Zernike coefficients of a certain size ($J$ = 12 to 20). Four regression methods performed better than LR (RF, KR, GB, GP) and were kept for full k-fold cross-validation. It was found that the best regression model was GB using all examined clinical variables as predictors and $J$ = 16 Zernike coefficients (GB 16 all, for short).

GB 16 all performed much better than the random model (RMSE = 10.87 μm vs. 33.00 μm), in which a surface is selected at random and compared to the others, so this model effectively learns. It was also better than the baseline (the mean surface) (RMSE = 23.43 μm), so it can discriminate the specificities of different surfaces. And it performed better than linear regression (11.79 μm), meaning that it can take advantage of its nonparametric architecture. As shown in the methods' description presented in Table 2.1, GB (gradient boosting) does not particularly distinguish itself from the other nonlinear regression methods examined: it is an ensemble of decision trees, and as such, it is not different from RF (random forest) and BF (bagging). However, like GP (Gaussian Process), which performed almost as well, it proceeds by gradient adjustments (gradient descent, while GP proceeds by gradient ascent).

Concerning the targets of GB 16 all, the best number of Zernike coefficients ($J$ = 16) can be viewed as the best compromise between a modeling constraint, for which the modeled surface is more accurate with more terms, and a prediction constraint, for which predicting fewer terms is less demanding. While this number of coefficients is rather small, the predicted surfaces reconstructed with $J$ = 16 are on average remarkably similar to the modeled true surfaces modeled with $J$ = 16 presented in Figure 5.4, which are themselves quite similar to the raw true surfaces presented in Figure 5.5, which uses different datasets of different sizes. This means that the predictions are on average quite accurate and robust. And notice that the learning margin was reduced by the repeatability error of the topographer of is 6.18 μm (estimated as the average of the RMSE differences between two topography acquisitions for the *same* individual for a 91×91 matrix of elevations; recall that the RMSE of GB 16 all is 10.87 μm).

It remains to verify whether the average elevation maps presented in Figure 5.4 are themselves consistent with the literature. Starting with geometric variables, the best-fit sphere (Bf) maps display a stark transition toward colder central colors along with a slight warming of peripheral colors as the radius of the BFS gets larger, meaning that the cornea becomes flatter, in accordance with [3]. The *white-to-white* (Ww) maps also display a transition toward colder central colors along with a slight warming of peripheral colors as the white-to-white distance increases, though not as strong as for the BFS radius. This is consistent with the fact that the white-to-white parameter is known to be inversely associated with the corneal curvature [7], pushing the cornea to become flatter and thus the radius of corneal curvature to increase [3]. The maps for the *anterior chamber depth* (Ad) show a slight increase and coldening of the central area of the cornea, signaling a slight flattening of the corneal area [8]. The *side* (Si) maps display a quasi-perfect interocular symmetry of color patterns (enantiomorphism) [10,51] as well as an intraocular asymmetry in which the nasal area displays less color change than the temporal area [10]. Concerning refraction variables, the *ametropia* (Am) maps (in which the SE increases) display a reduction in warm colors centrally and

reduction of the size of the warm color pattern that signals a slight apical flattening of the cornea [11,12] along with a shallowing of the anterior chamber depth (see the anterior chamber depth maps in reverse order) [9,13]. The *astigmatism* (As) maps present, as the axis gets progressively more vertical, a transition from an egg-shaped warm-color pattern that is horizontally laid down (first map) to another that is vertically stretched (third map) in passing an intermediate state (second map). This is indicative of a progressive decrease of the curvature of the vertical meridian and increase of the curvature of the horizontal meridian that reflects a transition from "with the rule" to "against the rule" astigmatism [15,16,17]. Finally, regarding demographic variables, the age (Ag) maps also display a transition from with-the-rule to against-the-rule astigmatism in old age [15,16,17,18]. A warming of the central yellow pattern is also observed in old age, in agreement with the finding that, with age, the anterior chamber depth becomes shallower (see Ad maps in reverse order) [8,13,20,21]. As for the *gender* (Ge) maps, the second (female) map presents a warmer central color pattern than the first (male) map, along with a smaller BFS R, in agreement with the fact that females have a steeper curvature [11,14,19] and a smaller white-to-white distance (Ww) than men [7,11,19].

Finally, as concern the predictors of the best model, the most determining predictor was the BFS radius (Bf), followed by the side of the corneal shape (Si) and by three refraction variables, including two variables that establish the angle of the corneal axis, defined in terms of cosinus (Co) and sinus (Sn) and one variable that specifies the cylinder (Cy) of the corneal shape. The other predictors, while contributing to decrease the error, had nonetheless only a marginal effect on it. A straightforward explanation of this state of affair would be that in order to predict effectively the corneal shape, one has to establish first the radius of its BFS. Since the shape of the cornea is close to a sphere, doing so provides most of the information needed to specify the shape of the cornea. Indeed, even taken alone as a predictor, the BFS radius does much better (RMSE = 14.01 μm) than all of the other predictors taken together (RMSE = 19.04 μm). Once the contribution of this important predictor is achieved, all that remains to be done is to specify the tiny departures of the corneal shape from the perfect sphere: this is fine adjustment. Given that the left and right eyes are known to be symmetrical in their departures from the perfect sphere, a first source of departure from the perfect sphere is indeed the side of the eye (Si) [10,51]. Other sources are those that lead to optical aberrations in normal eyes, including ametropia and astigmatism, which can be characterized by the axis of the cornea (Co and Sn) and by the cylinder (Cy). Once this information is specified, the other variables become to some extent redundant. White-to-white (Ww), anterior chamber depth (Ad) and genre (Ge) are known to correlate closely with the BFS, and age (Ag) with axis, as discussed above (their relative contribution is much more important when the BFS is removed from the set of predictors). However, the little importance of sphericity (Sp), also needed to define the degree of ametropia, is somewhat of a surprise. But considering the total information provided by the other variables, sphericity might also be somewhat redundant for the sake of predicting the corneal shape.

## 5.5. Conclusion

This study shows that it is possible to make an accurate prediction of the anterior surface of normal adult corneas shape using a machine learning methodology based on an average size (vs. big) dataset. We demonstrated that even a regression algorithm that does not exploit a big optimization space (in contrast with some deep learning algorithms) trained with a dataset of less than 8000 data was able to learn effectively the connection between 10 clinical parameters (9 if Axis-cosinus and Axis-sinus are counted as one parameter) and the corneal shape modeled with a limited set of 16 Zernike shape coefficients (mean height coefficient excluded). The atlas of elevation maps showed a close similarity between true and predicted average corneal surfaces. This similarity was robust, being well maintained in smaller datasets, and generalizable from one data subset to another. And the maps produced were consistent with the clinical literature on the anterior

corneal surface. The fact that the predictions formed valid corneal categories means that they implicitly achieved a form of supervised clinical classification.

Further improvements can be made to better predict the corneal shape from clinical variables and visualize the predictions and their central tendencies: by adding other relevant clinical predictors, by flipping horizontally OS corneas to get only OD corneas to predict, by testing other regression methods involving deep learning, by preprocessing data with other more effective geometric models (such as spherical harmonics or rational functions), by using a geometric model in combination with a linear or nonlinear feature extraction method. In so doing, it should be possible to extend the scope of the methodology and apply it to irregular surfaces and to other facets of the cornea (posterior surface, pachymetry).

## Acknowledgements

This work was supported by the QVRN (Quebec Vision Research Network), the FRQNT (Fonds de recherche du Québec Nature et Technologie) and the MUTAN (University Mission of Tunisia in North America).

# GENERAL CONCLUSION

This thesis aimed to investigate the best conditions in which corneas can be preprocessed, classified and predicted using geometric modeling and machine learning (ML) techniques. It proposed a procedure in which data are preprocessed by geometric modeling and validated by atlas visualization to support ML tasks of clustering or prediction (among other possibilities) involving corneal surfaces. This procedure was examined in a series of studies about the geometric modeling (Chapter 2), clinical classification (Chapter 3), unsupervised classification (Chapter 4), and prediction (Chapter 5) of normal adult anterior corneal surfaces.

Chapter 2 was concerned with the dimensionality reduction of normal adult corneal surface datasets by geometric modeling. Four types of geometric models were tested for their accuracy and processing time in a (relatively) low dimensional space ($J < 30$), including two polynomial (P) models (ZP and SHP) and two corresponding rational function (R) models (ZR and SHR). While SHP and ZR are known to be more accurate than ZP for the same number of coefficients, it was not clear as to whether the SH advantage was more important than the R advantage for effective dimensionality reduction. As expected, SHP and ZR were both more accurate than ZP in a low dimensional space. More generally, the two SH models performed better than the two Z models, and the two R models better than the two corresponding P models. On the other hand, concerning processing times, while the P models ran in quasi-linear time with a very low slope (especially ZP), the R models ran in polynomial time (with a quite steep increase in slope for SHR). Considering these results, if speed is privileged, the best model is ZP. Given its reasonable accuracy and transparent interpretability, it can advantageously be used in the development phases of ML projects, especially with normal corneas and when interpretability is important. If accuracy is critical and the prime consideration, then SHR is the best model. However, the gain of accuracy it provides is fairly small compared to its cost of processing time. Its processing time can be substantially reduced, though, by running a prior step of optimization with a small dataset to identify the best combinations of numerator and denominator coefficients (a major cause of processing time explosion) and focusing only on these combinations when modeling the whole dataset. But in the end, the best compromise between accuracy and speed remains SHP.

Chapter 3 dealt with the classification of normal adult anterior corneal surfaces based different clinical variables and with the visualization of the effects of these variables with an atlas of average elevation maps. Clinical classification is a requirement to explore the variability of the corneal shape, which is known to be affected by a number of clinical parameters, including geometric variables (BFS radius, white-to-white diameter, anterior chamber depth, corneal side, etc.), refraction variables (astigmatism, ametropia, etc.) and demographic variables (age, gender, etc.). While the quantitative assessment of this variability with statistical techniques of regression and mean comparison is a necessity, there is a need for the visual assessment of central tendencies, and group maps, a relatively recent development in visualization techniques, can be instrumental to this end. This issue was explored in this study, and an atlas of average elevation maps was constructed for different clinical variables (listed above) and was validated in light of the literature. Such a validated tool can be useful not only for clinical or pedagogical uses but also for validation and interpretation purposes in ML projects. We showed that this tool can be used to validate and interpret output datasets of clusters (Chapter 4) and predictions (Chapter 5).

With these preprocessing tools (geometric modeling) and this validation tool (atlas of group maps) in hand, the proposed procedure continued to be implemented in Chapter 4 and 5 with studies on ML tasks of clustering and prediction. Chapter 4 was concerned with the unsupervised classification of normal adult corneas based on their anterior surface. While the few existing studies used corneal clustering for the sake of automatic diagnosis and proceeded with a prior step of feature extraction to reduce the dimensionality of the dataset, we focused on normal corneas (whose unsupervised classification remained to be done) using geometric modeling to achieve

dimensionality reduction. In this study, geometric modeling was based on Zernike polynomials, selected for its transparent interpretability (each coefficient concerns a particular clinical feature of the cornea), considering its sufficient accuracy with normal corneas and convenient processing speed. Two linear clustering methods (agglomerative and k-means clustering) and one nonlinear method (spectral clustering) were tested. It was found, based on different qualitative and quantitative evaluation tools, that the linear methods grouped corneas essentially in terms of their curvature, whereas the nonlinear method did so mostly in terms of their axis. In addition to being effective in characterizing the natural groupings of normal adult corneas based on their anterior surface, the proposed clustering procedure can eventually be instrumental for the automatic classification of normal corneas.

Finally, the fourth study (Chapter 5) was about the prediction of the corneal shape based on clinical information. Resorting to nonparametric regression methods, it could take advantage of the complex relationship that holds between clinical corneal features and the corneal shape itself without having to make any assumption as to the form of this relationship. The clinical variables available in the database were used as predictors, and the vector of Zernike coefficients was employed to reduce the dimensionality of the dataset of normal adult anterior corneal surfaces used as targets. The issue was to identify the regression model that best predicted the shape of the cornea based on the available clinical information. A regression model was defined as a selection of a set of clinical variables used as predictors, of a nonparametric algorithm used as regression method (along with parametric methods serving as reference methods), and of a vector of Zernike coefficients of a given size ($J$) as used as targets. Based on RMSE scores (to measure the distance between the surfaces predicted by a model and the corresponding true raw topographic surfaces), it was found that the best model was gradient boosting with all available clinical variables and 16 Zernike coefficients. Using the atlas of average elevation maps as a visual validation tool, these predictions were found to be clinically sound, being on average surfaces that were very similar to the true modeled surfaces. This means that the complex relationship that holds between the examined clinical variables and the corneal shape is strong enough to allow sound predictions. The most contributive predictor was by far the BFS radius, which defines the cornea as a sphere. Then, other predictors contributed to specify the tiny departures of the cornea from its ideal quasi-spherical form, including the side of the cornea, and refractive features (axis and cylinder). This study was exploratory and aimed at making a proof of concept to establish that it is possible to predict the central tendencies of corneal shape across a number of clinical conditions. However, it is possible to make even better or more demanding predictions by testing new regression models on normal and irregular corneas. For instance, known to be more accurate, spherical harmonics could be used instead of Zernike polynomials for dimensionality reduction, or else deep learning algorithms could be used in place of gradient boosting as a regression method. Given the prime importance of side as a predictor, it should be beneficial to dispense the algorithm with the necessity to distinguish between right and left corneas by taking advantage of their symmetry and by horizontally flip left corneas and turn them into right corneas. Finally, the dimensionality of the dataset can be further reduced by applying feature extraction in combination with geometric modeling to alleviate the prediction load. In this improvement process, the best regression model identified in this study (gradient boosting 16 with all clinical variables) can be regarded as the new, more demanding standard of reference for this research.

# References


[1] Rhcastilhos. And Jmarchn., CC BY-SA 3.0 <https://creativecommons.org/licenses/by-sa/3.0>, via Wikimedia Commons, *File:Schematic diagram of the human eye en.svg*. 2007. [Online]. Available: https://commons.wikimedia.org/wiki/File:Schematic_diagram_of_the_human_eye_en.svg

[2] *Topographie cornéenne – Orbscan*. [Online]. Available: https://commons.wikimedia.org/wiki/File:Topographie_corn%C3%A9enne_%E2%80%93_Orbscan.jpg#/media/Fichier:Topographie_corn%C3%A9enne_%E2%80%93_Orbscan.jpg

[3] D. Gatinel, J. Malet, T. Hoang-Xuan, and D. T. Azar, "Corneal Elevation Topography: Best Fit Sphere, Elevation Distance, Asphericity, Toricity, and Clinical Implications:," *Cornea*, vol. 30, no. 5, pp. 508–515, May 2011, doi: 10.1097/ICO.0b013e3181fb4fa7.

[4] Nagorsky, CC BY 3.0, *Компьютерная кератотопография*. 2011. [Online]. Available: https://upload.wikimedia.org/wikipedia/commons/b/bb/%D0%9A%D0%B5%D1%80%D0%B0%D1%82%D0%BE%D1%82%D0%BE%D0%BF%D0%BE%D0%B3%D1%80%D0%B0%D1%84.JPG

[5] Isabelle Brunette, Jean Meunier, and Marie-Claude Robert, "Database for the anatomopathological, functional and surgical characterization of the cornea," *Database for the anatomopathological, functional and surgical characterization of the cornea*, Jun. 17, 2022. https://visionnetwork.ca/actuelles/robert/ (accessed Jun. 17, 2022).

[6] D. Meister and J. E. Sheedy, *Introduction to Ophthalmic Optics*, Carl Zeiss Vision. San Diego, CA.

[7] H. Hashemi, M. Khabazkhoob, M. H. Emamian, M. Shariati, A. Yekta, and A. Fotouhi, "White-to-white corneal diameter distribution in an adult population," *Journal of Current Ophthalmology*, vol. 27, no. 1–2, pp. 21–24, Mar. 2015, doi: 10.1016/j.joco.2015.09.001.

[8] H. Chen, H. Lin, Z. Lin, J. Chen, and W. Chen, "Distribution of axial length, anterior chamber depth, and corneal curvature in an aged population in South China," *BMC Ophthalmol*, vol. 16, no. 1, p. 47, Dec. 2016, doi: 10.1186/s12886-016-0221-5.

[9] M. Hosny, J. L. Alió, P. Claramonte, W. H. Attia, and J. J. Pérez-Santonja, "Relationship Between Anterior Chamber Depth, Refractive State, Corneal Diameter, and Axial Length," *J Refract Surg*, vol. 16, no. 3, pp. 336–340, May 2000, doi: 10.3928/1081-597X-20000501-07.

[10] S. A. Dingeldein and S. D. Klyce, "The topography of normal corneas," *Arch. Ophthalmol.*, vol. 107, no. 4, pp. 512–518, Apr. 1989.

[11] K. P. Mashige, "A review of corneal diameter, curvature and thickness values and influencing factors*," *African Vision and Eye Health*, vol. 72, no. 4, Dec. 2013, doi: 10.4102/aveh.v72i4.58.

[12] K. Kato, M. Kondo, M. Takeuchi, and K. Hirano, "Refractive error and biometrics of anterior segment of eyes of healthy young university students in Japan," *Sci Rep*, vol. 9, no. 1, p. 15337, Dec. 2019, doi: 10.1038/s41598-019-51920-4.

[13] V. Bhardwaj and G. P. Rajeshbhai, "Axial length, anterior chamber depth-a study in different age groups and refractive errors," *J Clin Diagn Res*, vol. 7, no. 10, pp. 2211–2212, Oct. 2013, doi: 10.7860/JCDR/2013/7015.3473.

[14] H. Bouazizi, I. Brunette, and J. Meunier, "Are There Categories of Corneal Shapes?," in *2018 40th Annual International Conference of the IEEE Engineering in Medicine and Biology Society (EMBC)*, Honolulu, HI: IEEE, Jul. 2018, pp. 2719–2723. doi: 10.1109/EMBC.2018.8512882.

[15] E. Gudmundsdottir *et al.*, "'With the rule' astigmatism is not the rule in the elderly: Reykjavik Eye Study: A population based study of refraction and visual acuity in citizens of

Reykjavik 50 years and older," *Acta Ophthalmologica Scandinavica*, vol. 78, no. 6, pp. 642–646, Dec. 2000, doi: 10.1034/j.1600-0420.2000.078006642.x.
[16] W. R. Baldwin and D. Mills, "A longitudinal study of corneal astigmatism and total astigmatism," *American journal of optometry and physiological optics*, vol. 58, no. 3, 1981.
[17] G. Nemeth, E. Szalai, A. Berta, and L. Modis, "Astigmatism Prevalence and Biometric Analysis in Normal Population," *European Journal of Ophthalmology*, vol. 23, no. 6, pp. 779–783, Nov. 2013, doi: 10.5301/ejo.5000294.
[18] X. Shao *et al.*, "Age-Related Changes in Corneal Astigmatism," *J Refract Surg*, vol. 33, no. 10, pp. 696–703, Oct. 2017, doi: 10.3928/1081597X-20170718-04.
[19] E. Iyamu and E. Osuobeni, "Age, gender, corneal diameter, corneal curvature and central corneal thickness in Nigerians with normal intra ocular pressure," *Journal of Optometry*, vol. 5, no. 2, pp. 87–97, Apr. 2012, doi: 10.1016/j.optom.2012.02.001.
[20] H. Hashemi *et al.*, "The distribution of axial length, anterior chamber depth, lens thickness, and vitreous chamber depth in an adult population of Shahroud, Iran," *BMC Ophthalmol*, vol. 12, no. 1, p. 50, Dec. 2012, doi: 10.1186/1471-2415-12-50.
[21] H.-D. Miguel Angel, G. Sara Gonzalez, and V.-G. Jorge, "Clinical features of the Anterior Chamber Depth," *Int J Ophthalmol Clin Res*, vol. 8, no. 2, Apr. 2021, doi: 10.23937/2378-346X/1410125.
[22] P. J. Foster and Y. Jiang, "Epidemiology of myopia," *Eye*, vol. 28, no. 2, pp. 202–208, Feb. 2014, doi: 10.1038/eye.2013.280.
[23] K. E. Lee, B. E. K. Klein, R. Klein, and T. Y. Wong, "Changes in refraction over 10 years in an adult population: the Beaver Dam Eye study," *Invest Ophthalmol Vis Sci*, vol. 43, no. 8, pp. 2566–2571, Aug. 2002.
[24] F. Orucoglu, M. Akman, and S. Onal, "Analysis of age, refractive error and gender related changes of the cornea and the anterior segment of the eye with Scheimpflug imaging," *Contact Lens and Anterior Eye*, vol. 38, no. 5, pp. 345–350, Oct. 2015, doi: 10.1016/j.clae.2015.03.009.
[25] H. Hashemi, A. Fotouhi, and K. Mohammad, "The age- and gender-specific prevalences of refractive errors in Tehran: the Tehran Eye Study," *Ophthalmic Epidemiology*, vol. 11, no. 3, pp. 213–225, Jan. 2004, doi: 10.1080/09286580490514513.
[26] D. Gatinel, M. Haouat, and T. Hoang-Xuan, "[A review of mathematical descriptors of corneal asphericity]," *J Fr Ophtalmol*, vol. 25, no. 1, pp. 81–90, Jan. 2002.
[27] J. A. Corbin, S. A. Klein, and C. van de Pol, "Measuring effects of refractive surgery on corneas using Taylor series polynomials," presented at the BiOS '99 International Biomedical Optics Symposium, San Jose, CA, P. O. Rol, K. M. Joos, F. Manns, B. E. Stuck, and M. Belkin, Eds., San Jose, CA, Jun. 1999, p. 46. doi: 10.1117/12.350598.
[28] Lewis, N D., "Corneal topography measurements for biometric applications," The University of Arizona., 2011.
[29] A. Polette, J.-L. Mari, I. Brunette, and J. Meunier, "Comparison of quasi-spherical surfaces – application to corneal biometry," *IET Biometrics*, vol. 5, no. 3, pp. 212–219, Sep. 2016, doi: 10.1049/iet-bmt.2015.0048.
[30] H. Bouazizi, I. Brunette, and J. Meunier, "Comparison of parametric methods for modeling corneal surfaces," presented at the SPIE Medical Imaging, Orlando, Florida, United States, M. A. Styner and E. D. Angelini, Eds., Orlando, Florida, United States, Feb. 2017, p. 101332E. doi: 10.1117/12.2254426.
[31] J. Schwiegerling, J. E. Greivenkamp, and J. M. Miller, "Representation of videokeratoscopic height data with Zernike polynomials," *J. Opt. Soc. Am. A*, vol. 12, no. 10, p. 2105, Oct. 1995, doi: 10.1364/JOSAA.12.002105.

[32] D. R. Iskander, M. R. Morelande, M. J. Collins, and B. Davis, “Modeling of corneal surfaces with radial polynomials,” *IEEE Trans. Biomed. Eng.*, vol. 49, no. 4, pp. 320–328, Apr. 2002, doi: 10.1109/10.991159.
[33] R. Iskander, M. Collins, and B. Davis, “Modeling corneal surfaces with three-dimensional basis functions,” Jan. 2009.
[34] D. R. Iskander, “Modeling videokeratoscopic height data with spherical harmonics,” *Optom Vis Sci*, vol. 86, no. 5, pp. 542–547, May 2009, doi: 10.1097/OPX.0b013e31819fa8ec.
[35] M. Schneider, D. R. Iskander, and M. J. Collins, “Modeling Corneal Surfaces With Rational Functions for High-Speed Videokeratoscopy Data Compression,” *IEEE Trans. Biomed. Eng.*, vol. 56, no. 2, pp. 493–499, Feb. 2009, doi: 10.1109/TBME.2008.2006019.
[36] The SciPy Community, “ScyPy.org.” The SciPy Community, 2019. [Online]. Available: https://docs.scipy.org/doc/scipy/reference/index.html
[37] D. Marquardt, “An Algorithm for Least-Squares Estimation of Nonlinear Parameters,” *SIAM J. Appl. Math*, vol. 11, pp. 431–441, 1963.
[38] J.-F. Laliberte´, J. Meunier, M. Chagnon, J.-C. Kieffer, and I. Brunette, “Construction of a 3-D Atlas of Corneal Shape,” *Investigative Opthalmology & Visual Science*, vol. 48, no. 3, p. 1072, Mar. 2007, doi: 10.1167/iovs.06-0681.
[39] M. Halkidi, Y. Batistakis, and M. Vazirgiannis, “On Clustering Validation Techniques,” *Journal of Intelligent Information Systems*, vol. 17, no. 2/3, pp. 107–145, 2001, doi: 10.1023/A:1012801612483.
[40] Pedregosa et al., “Scikit-learn: Machine Learning in Python,” *JMLR*, vol. 12, pp. 2825–2830, 2011.
[41] T. Y. Baker, “Raytracing through non-spherical surfaces,” *Proceeds of the Royal Society*, vol. 55, pp. 361–4, 1944.
[42] M. F. Greenwald, B. A. Scruggs, J. M. Vislisel, and M. A. Greiner, “Corneal Imaging: An Introduction.” Eyes Round.org, 2016. [Online]. Available: https://webeye.ophth.uiowa.edu/eyeforum/tutorials/Corneal-Imaging/Index.htm
[43] A. Polette, E. Auvinet, J.-L. Mari, I. Brunette, and J. Meunier, “Constructing average models of quasi-spherical objects: application to corneal topographies,” *Computer Methods in Biomechanics and Biomedical Engineering: Imaging & Visualization*, vol. 5, no. 4, pp. 241–250, Jul. 2017, doi: 10.1080/21681163.2015.1077164.
[44] D. R. Iskander, M. J. Collins, and B. Davis, “Modeling Corneal Surfaces With Three-Dimensional Basis Functions,” *Investigative Ophthalmology & Visual Science*, vol. 50, no. 13, pp. 5086–5086, Apr. 2009.
[45] wiki, “Narval,” *Narval*, Aug. 06, 2022. https://docs.alliancecan.ca/wiki/Narval (accessed Jun. 17, 2022).
[46] K. Hayashi, F. Nakao, and F. Hayashi, “Corneal topographic analysis of superolateral incision cataract surgery,” *Journal of Cataract and Refractive Surgery*, vol. 20, no. 4, pp. 392–399, Jul. 1994, doi: 10.1016/S0886-3350(13)80173-3.
[47] T. Buehren, M. J. Collins, D. R. Iskander, B. Davis, and B. Lingelbach, “The Stability of Corneal Topography in the Post-Blink Interval:,” *Cornea*, vol. 20, no. 8, pp. 826–833, Nov. 2001, doi: 10.1097/00003226-200111000-00010.
[48] H.-B. Fam, K.-L. Lim, and D. Z. Reinstein, “Orbscan Global Pachymetry: Analysis of Repeated Measures,” *Optometry and Vision Science*, vol. 82, no. 12, pp. 1047–1053, Dec. 2005, doi: 10.1097/01.opx.0000192348.37026.09.
[49] K. P. Mashige, “A review of corneal diameter, curvature and thickness values and influencing factors*,” *African Vision and Eye Health*, vol. 72, no. 4, pp. 185–194, Dec. 2013, doi: 10.4102/aveh.v72i4.58.

[50] S. Heydarian *et al.*, “The normal distribution of corneal eccentricity and its determinants in two rural areas of north and south of Iran,” *Journal of Current Ophthalmology*, vol. 30, no. 2, pp. 147–151, Jun. 2018, doi: 10.1016/j.joco.2017.11.006.
[51] G. M. Durr, E. Auvinet, J. Ong, J. Meunier, and I. Brunette, “Corneal Shape, Volume, and Interocular Symmetry: Parameters to Optimize the Design of Biosynthetic Corneal Substitutes,” *Investigative Opthalmology & Visual Science*, vol. 56, no. 8, p. 4275, Jul. 2015, doi: 10.1167/iovs.15-16710.
[52] M. H. Cheon *et al.*, “Effect of age on anterior chamber angle configuration in Asians determined by anterior segment optical coherence tomography; clinic-based study,” *Acta Ophthalmologica*, vol. 88, no. 6, pp. e205–e210, Sep. 2010, doi: 10.1111/j.1755-3768.2010.01960.x.
[53] E. Iyamu and E. Osuobeni, “Age, gender, corneal diameter, corneal curvature and central corneal thickness in Nigerians with normal intra ocular pressure,” *Journal of Optometry*, vol. 5, no. 2, pp. 87–97, Apr. 2012, doi: 10.1016/j.optom.2012.02.001.
[54] S. Yousefi *et al.*, “Keratoconus severity identification using unsupervised machine learning,” *PLoS ONE*, vol. 13, no. 11, p. e0205998, Nov. 2018, doi: 10.1371/journal.pone.0205998.
[55] N. Hallett *et al.*, “Deep Learning Based Unsupervised and Semi-supervised Classification for Keratoconus.” arXiv, Jan. 30, 2020. Accessed: Sep. 10, 2022. [Online]. Available: http://arxiv.org/abs/2001.11653
[56] P. Zéboulon, G. Debellemanière, and D. Gatinel, “Unsupervised learning for large-scale corneal topography clustering,” *Sci Rep*, vol. 10, no. 1, p. 16973, Dec. 2020, doi: 10.1038/s41598-020-73902-7.
[57] D. R. Iskander, M. J. Collins, and B. Davis, “Optimal modeling of corneal surfaces with Zernike polynomials,” *IEEE Transactions on Biomedical Engineering*, vol. 48, no. 1, pp. 87–95, Jan. 2001, doi: 10.1109/10.900255.
[58] S. K. Jameel, S. Aydin, and N. H. Ghaeb, “Machine Learning Techniques for Corneal Diseases Diagnosis: A Survey,” *Int. J. Image Grap.*, vol. 21, no. 02, p. 2150016, Apr. 2021, doi: 10.1142/S0219467821500169.
[59] J. Espinosa, J. Pérez, and A. Villanueva, “Prediction of Subjective Refraction From Anterior Corneal Surface, Eye Lengths, and Age Using Machine Learning Algorithms,” *Trans. Vis. Sci. Tech.*, vol. 11, no. 4, p. 8, Apr. 2022, doi: 10.1167/tvst.11.4.8.
[60] A. Lavric, V. Popa, H. Takahashi, R. M. Hazarbassanov, and S. Yousefi, “Association between visual field damage and corneal structural parameters,” *Sci Rep*, vol. 11, no. 1, p. 10732, May 2021, doi: 10.1038/s41598-021-90298-0.
[61] K. Kamiya, Y. Ayatsuka, Y. Kato, N. Shoji, Y. Mori, and K. Miyata, “Diagnosability of Keratoconus Using Deep Learning With Placido Disk-Based Corneal Topography,” *Front. Med.*, vol. 8, p. 724902, Oct. 2021, doi: 10.3389/fmed.2021.724902.